ABSTRACT

Title of Dissertation: QUANTUM APPLICATIONS, PARALLEL OPERATIONS, AND NOISE CHARACTERIZATION ON A TRAPPED ION QUANTUM COMPUTER

Yingyue Zhu
Doctor of Philosophy, 2024

Dissertation Directed by: Professor Norbert M. Linke
Department of Physics

Quantum computing holds vast potential for solving classically hard problems ranging from optimization to simulations critical in material science research and drug discovery. While large-scale fault-tolerant quantum computers capable of these tasks are yet to come, small and noisy prototypes have been demonstrated on several candidate platforms. Among these, trapped-ion qubits have been at the forefront of quantum computing hardware because of their long coherence times, high-fidelity quantum gates, and all-to-all connectivity. This dissertation investigates new methods for efficient quantum computing at the interface of quantum information theory and trapped-ion experiments, and advances both the control of physical trapped-ion hardware and the characterization of their decoherence processes.

We present a number of proof-of-principle experiments for early quantum applications on a trapped-ion quantum computer (TIQC). First, we experimentally show that the results of the Quantum Approximate Optimization Algorithm (QAOA)—a method to solve graph combinatorial optimization problems by applying multiple rounds of variational circuits—improve with deeper circuits for multiple graph-theoretic problems on several arbitrary graphs. We also demonstrate a modified version of QAOA that allows sampling of all optimal solutions with predetermined weights. Additionally, we implement the real-time evolution of

a one-dimensional scattering process and demonstrate a more efficient and accurate method to extract the phase shift, forming a tentative first step towards the goal of lattice quantum chromodynamics (QCD) simulation. Furthermore, we demonstrate two Bell-type nonlocal games that can be used to prove quantum computational advantage as well as offer a set of practical and scalable benchmarks for quantum computers in the pre-fault-tolerant regime. Our experimental results indicate that the performance of quantum strategies for the nonlocal games exceeds basic classical bounds, and is on the cusp of demonstrating quantum advantage against more complicated classical strategies.

We propose and demonstrate a high-fidelity and resource-efficient scheme for driving simultaneous entangling gates on different sets of orthogonal motional modes of a trapped-ion chain. We show the advantage of parallel operation with a simple digital quantum simulation where parallel implementation improves the overall fidelity significantly.

We test and improve the performance of an ancilla-assisted protocol for learning Pauli noise in Clifford gates on a TIQC. With N ancilla, Pauli noise in an $N-$qubit Clifford gate can be learned with a sample size linear to N. We also design and demonstrate a way to improve the protocol's performance by reducing ancilla noise in post-processing.

QUANTUM APPLICATIONS, PARALLEL OPERATIONS, AND NOISE CHARACTERIZATION ON A TRAPPED ION QUANTUM COMPUTER

by

Yingyue Zhu

Dissertation submitted to the Faculty of the Graduate School of the
University of Maryland, College Park in partial fulfillment
of the requirements for the degree of
Doctor of Philosophy
2024

Advisory Committee:
Professor Norbert M. Linke, Advisor
Professor Christopher Jarzynski, Dean's Representative
Professor Steven Rolston, Chair
Professor Yu Liu
Professor Avit Dutt

Acknowledgements

First and foremost, I would like to express my deepest gratitude to my advisor, Norbert Linke, for giving me the opportunity to join this incredible group, for trusting me with challenging research projects, and for providing guidance whenever I struggled. Your unwavering support and encouragement, even during moments of self-doubt, have been invaluable.

Words cannot adequately convey my gratitude to my colleague, mentor, and friend, Alaina Green. I have learned so much from you—not only about becoming a better researcher but also about being a true friend. Thank you for always being there for me. I hope that one day, I can be as exceptional a mentor to someone else as you have been to me.

In the past six years, I have had the great honor of collaborating with many brilliant researchers outside my research group, including Zewen Zhang, Bhuvanesh Sundar, Kaden R. A. Hazzard, Erik Gustafson, Patrick Dreher, Yannick Meurice, Austin K Daniel, Vikas Buchemmavari, Tyler G Thurtell, Andrew Zhao, Akimasa Miyake, Alireza Seif, Senrui Chen, Liang Jiang, Masoud Mohammadi-Arzanagh, Yunseong Nam, Daiwei Zhu, Ze-Pei Cian, and others. Thank you for everything I have learned from you.

Many thanks to Nhung H. Nguyen, Cinthia Huerta Adelete, Daiwei Zhu, Liam Jeanette, Mika Chmielewski, Denton Wu, Henry Luo, Michael Straus, Anton Than, Matthew Diaz, Xingxin Liu, and all the other member of Linke Lab. Thank you not only for your help as brilliant colleagues but also for your friendship. I will treasure the memories of our group lunches, board game nights, and lab trips. My gratitude also extends to the other residents of the Atlantic basement: Kate Collins, Connor Goham, Andrew Laugharn, Wance Wang,

and Joe Britton. Your presence brought joy and made this journey far more enjoyable. I would also like to thank Andrew Risinger, Bin Cao, Marie Lu, and William Morong for their help navigating the job market.

I could not have come this far without the friendship of Chenwei Tang, Tianyi Xie, Cynthia Giron, Kungang Li, Qingfeng Wang, Yukari Yamauchi, Dan Zhang, Julia McMurray, Matt Kovacs-Deak. A special thanks goes to my housemates for making our shared home a restful harbor where we could recharge from the daily grind of grad school.

I am incredibly fortunate to have had my partner, Andrew Guo, by my side for the past five years. I am also profoundly grateful to Andrew's family for welcoming me into their home and sharing with me their warmth, especially when I have been 7,000 miles away from my own family. Lastly, I would like to thank my parents, Baoxin Zhu and Yunzhi Ren, for giving me life, and more importantly, for their unconditional love and support, which has made all of this possible.

Thank you so much!

Table of contents

List of Tables

List of Figures

Chapter 1

Introduction

1.1 Introduction to Quantum Computing

The world we live in and interact with seems classical. The building blocks of all modern computer chips are transistors, and they behave like two-position switches that can take the values of either “on”(1) or “off”(0), forming the basis of classical computation. When we look past the macroscopic effects and dive deeper, to the subatomic level, the world follows the rules of quantum mechanics. A quantum bit, or a "qubit", can exist in superposition of both 0 and 1. Entanglement can be created between qubits such that they become correlated and no longer have independent states. Classical simulations of large and highly entangled quantum systems are extremely challenging as the size of the Hilbert space increases exponentially with the size of the system. The idea of using a quantum system constituted of qubits to efficiently simulate another quantum system was born to address this problem. Since then, research on information processing with quantum systems expanded beyond simulating physical systems to more generic computing tasks. Quantum algorithms for solving abstract computational problems utilizing superposition, entanglement, and interference have been developed and proven to be significantly more efficient than their classical counterparts. Today, quantum computing holds the potential to solve a wide class of classically expensive

computing problems, such as factorization [226], large search and optimization problems [3, 6, 48, 83, 85, 110], simulation of molecular structures, chemical reactions and material [10, 44, 140] and others.

Quantum computers can be built using a variety of technologies. Superconducting qubits are built using superconducting electronic circuits containing Josephson Junctions [130]. The system have fast quantum gates on the nanosecond order with nearest neighbour connectivity and highly scalable architecture. Spin qubits, realized in silicon or nitrogen-vacancy centers, are encoded in the spin states of electrons in semiconducting material, and can be mass-produced with conventional semiconductor manufacturing processes [45]. Although large number of qubits are easier to achieve for these two type of qubits, they usually suffer from strong coupling to the environment and artifacts in manufacturing. Technologies based on atoms and atomics ions benefits from naturally identical qubits. Neutral atoms trapped in optical lattice or tweezers can be coherently controlled by laser and entangled via Rydberg interactions [122]. Trapped atomic ions confined in Radio Frequency (RF) electric fields or static electric and magnetic fields are another promising platform for realizing quantum computers [42]. Other emerging technologies include photonic systems and topological qubits. Each platform has unique advantages and challenges in terms of scalability, error rates, and coherence times, and ongoing research explores all the possible avenues to reach the goal of building a useful quantum computer.

1.2 Introduction to the Trapped-Ion Quantum Computer (TIQC)

Trapped ions have long been at the forefront of experimental quantum computing. The qubits are usually encoded in the quantum states of the outmost electron. Atomic ions provide naturally identical and well-isolated qubits with long coherence time and high controllability. The qubit phase coherence time T_2, is typically on the order of seconds. When

compared to the single and two-qubit gate times which are on the order of tens and hundreds of microseconds, it is clear that it is possible to apply a large number of gate operations before decoherence sets in. The longest T_2 time observed in trapped-ion qubits was more than an hour in Ref [250], and the qubit was defined in the hyperfine split ground states of a single $^{171}Yb^{+}$ ion, the same qubit used in this thesis. Besides hyperfine encoding, qubits can also be defined over different electronic orbital states to form optical and metastable qubits. More recently, conversions between different qubit types within the same ion have also been demonstrated. The qubits state can be initialized by optical pumping and read out with laser driven florensce detection, and coherent manipulation of the qubits can be carried out with lasers or microwaves with high precision. Single-qubit and two-qubit gate fidelity higher than 99.99% and 99.9%, respectively, have been shown [15, 59, 93], exceeding the fidelity requirements for building fault tolerant machines with many promising Quantum error correction code. Finally, we note unique feature of TIQC which not shared by most of the other leading quantum computing platforms, since the entangling operations are mediated by collective motional modes, in which all ions confined in the same trapping potential participate, the qubits are all-to-all connected, providing advantage for applications with non-nearest neighbour interactions.

Over the past few decades, Ions of almost all of the alkaline-earth and alkaline-earth atoms have been trapped. Various types of ion traps, such as Linear Paul Traps and Microfabricated Surface Traps where ions are usually trapped in linear chain configurations, and Penning Traps where ions form rotating crystals, have been used to build TIQC. New cooling and coherent control schemes were proposed and successfully implemented. Advanced operations vital for device scale-up and error correction, such as splitting up long ion chains, combining short chains, and ion shuttling, have also been developed[268]. In the recent years, TIQC have grown to systems with 20-40 individually controlled qubits in multiple architectures, enabled by and integrating together many of the above-mentioned technological advances made on smaller-sized devices[134, 185]. To further scale up trapped ion systems,

one promising strategy is to connect multiple modules with photonic links[73, 183]. Trapped ion qubits that are coupled to telecom photon are particularly suitable for serving as the communication nodes in each module. The ability to co-trap and entangle more than one ion species or isotopes allows combining qubits with complimentary advantages into one module and maximize the capability of future trapped-ion quantum computers.

1.3 Current Devices and Challenges

In order to solve any problem of practical value, quantum computers need a large number of qubits and low enough error rates. Quantum computers are very sensitive to error. In long operation sequences, even a very small error per operation can eventually destroy the quantum information. Quantum error correction (QEC) allows active error detection and correction without collapsing the protected quantum state. It requires the encoding of each logical qubit across several physical qubits. QEC is a costly process, and the more errors there are to be corrected, the more resource overhead is needed. And the effectiveness of QEC is only guaranteed when the physical gate error is lower than the error threshold of the specific QEC code used. One of the main challenges trapped-ion technology faces is to scale up the system size while maintaining high-fidelity operations. Usually, gate fidelities decrease when the number of qubits in the system increases, due to increased sources of noise and higher susceptibility to noise. Continuous improvement in physical gate fidelity, especially two-qubit gate fidelity, remains a vital task. Additionally, cost and performance of QEC codes depend significantly on the noise environment. Accurate noise models for real hardware platforms can be leveraged to lower the cost of QEC and error mitigation.

While the development of large-scale fault-tolerant quantum computing devices is ongoing, many of the above-mentioned challenges can continue to be addressed by research on smaller systems that are already available, like the one I used for this thesis. Many techniques that enhance a quantum platform's capability can be developed and tested in lab

experiments of smaller scale and directly deployed to larger systems later. This includes the development of high-fidelity entangling gates, parallel gates, and multi-body gates in trapped ions. The goal is for physical entangling operations to be carried out with higher fidelity either by engineering noise-robust controls or by reducing experimental time and therefore experimental errors. Evidence strongly suggests that platforms with the same underlying technology share similar noise environments [267]. Studying device limitations and noise models on smaller systems can allow us to gain insight into and predict noise in larger systems. Detailed knowledge of noise will enable also the co-design of new generations of low-noise hardware and tailored QEC protocols that are low-cost high-performance.

Another challenge faced in the wider quantum computing field is that, although it is widely recognized that quantum computing has vast potential in solving classically unattainable problems, there are very few readily available algorithms and methods. Researchers across the scientific community, who wish to apply quantum computing to difficulty problems in their own fields, are still working on exploring and prototyping new methods and tools for unlocking the power of quantum computers. For this reason, different scientific communities have a strong interest and need in testing small-scale applications on currently available devices. This not only allows testing of proof of principle demonstrations but also continue to provide research and education opportunities for the next generation of users who will run large-scale experiments on the future fault-tolerant devices. In return, the users can provide valuable feedback to experimentalists working on building better quantum computers.

1.4 Outline of the Dissertation

In this dissertation, I present my contributions to many aspects of experimental trapped-ion quantum computing. These include successful demonstrations of early quantum applications, high-fidelity parallel entanglement operations, quantum state verification, and noise

characterization. Many projects reported here are completed in collaboration with others in the GATES lab at University of Maryland and at other institutions. The dissertation is organized as follows:

Chapter 2 describes the full-stack architecture of a trapped-ion quantum computer including the hardware platform, the control system, and basic coherent quantum operations. This chapter explains how to make qubits out of atomic ions and make them perform computing tasks for us.

Chapter 3 focuses on the realization of three early quantum applications representing several avenues of interest the field has been exploring: optimization problems, simulation of quantum systems, and quantum advantage demonstrations. In Chapter 3.1, we advance the Quantum Approximate Optimization Algorithm (QAOA), a quantum-classical hybrid variational algorithm, by showing the experimental optimization results improved with circuit depth. We test a variation of QAOA inspired by Grover's search in sampling problems. In Chapter 3.2, as a first step toward simulating lattice quantum chromodynamics (QCD) on quantum computers, we measure phase shifts in scattering events simulated on a trapped-ion quantum computer in real time using information about the early and intermediate stages of the collision. In Chapter 3.3, we perform two Bell-type nonlocal games that can be used to demonstrate quantum computational advantage and achieve win rates with quantum strategies exceeding the classical bounds in several settings. This chapter is based on the following publications:

- *Multi-round QAOA and advanced mixers on a trapped-ion quantum computer*, **Yingyue Zhu**, Zewen Zhang, Bhuvanesh Sundar, Alaina M Green, C Huerta Alderete, Nhung H Nguyen, Kaden R A Hazzard and Norbert M Linke, Quantum Sci. Technol. 8 015007 (2022)

- *Real-time quantum calculations of phase shifts using wave packet time delays*, Erik Gustafson, **Yingyue Zhu**, Patrick Dreher, Norbert M. Linke, and Yannick Meurice, Phys. Rev. D 104, 054507 (2021)

- *Quantum computational advantage attested by nonlocal games with the cyclic cluster state*, Austin K. Daniel, **Yingyue Zhu**, C. Huerta Alderete, Vikas Buchemmavari, Alaina M. Green, Nhung H. Nguyen, Tyler G. Thurtell, Andrew Zhao, Norbert M. Linke, and Akimasa Miyake, Phys. Rev. Research 4, 033068 (2022)

Chapter 4 is centered around the verification of the outcome of quantum computing results and the characterization of noise on quantum computers. The common tool used in these two tasks is tomography, and the common challenge is the exponential scaling of the required sample size with system size. In Chapter 4.1, we compare quantum states prepared on our own and other quantum computers with different underlying technologies, using randomized and correlated measurements, allowing us to study the intra-technology similarities and differences on an array of quantum computing hardware platforms. In Chapter 4.2 we experimentally test an efficient protocol for characterizing Pauli noise in a class of quantum gates and use it to benchmark noise in our native two-qubit entangling gate. We study how the method adapts to a noise environment native to trapped ions and methods to improve the its performance in the presence of this particular noise environment. Chapter 4.1 is based on the following publication and manuscript in preparation:

- *Cross-platform comparison of arbitrary quantum states*, D. Zhu, Z. P. Cian, C. Noel, A. Risinger, D. Biswas, L. Egan, **Y. Zhu**, A. M. Green, C. Huerta Alderete, N. H. Nguyen, Q. Wang, A. Maksymov, Y. Nam, M. Cetina, N. M. Linke, M. Hafezi, and C. Monroe, Nature Communications volume 13, Article number: 6620 (2022)

- *Efficent benchmarking of Pauli noise in entangling gates on a trapped-ion quantum computer*, **Y. Zhu**, S. Chen, A. Seif, A. M. Green, N. H. Nguyen, N. M. Linke, L. Jiang, in preparation (2024)

In Chapter 5, we propose and implement a high-fidelity parallel entangling gates scheme where entangling gates are driven simultaneously on different sets of orthogonal motional modes of the ion chain. This scheme does not require extra optical power or extra classical

overhead in most cases and can be used to parallelize most addressed entangling gate schemes in ion chains. We demonstrate the advantage of this scheme by implementing a trotterized evolution of the Transverse-Field Ising model and showing that substituting series gates for parallelized gates results in a more accurate simulation. This chapter is based on the following publication:

- *Pairwise-Parallel Entangling Gates on Orthogonal Modes in a Trapped-Ion Chain*, **Yingyue Zhu**, Alaina M. Green, Nhung H. Nguyen, C. Huerta Alderete, Elijah Mossman, Norbert M. Linke, Adv Quantum Technol, 6, 2300056 (2023)

Statement of Contribution

Most of my PhD work was done in collaboration with members of the UMD Gates lab and other external collaborators. This dissertation highlights the projects that I made significant contributions to.

For the three projects presented in Chapter 3, I was the lead experimental contributor. In the QAOA project described in Chapter 3.1, I co-designed and implemented the experiments, analyzed data, and wrote the manuscript. In the scattering simulation and the quantum non-local games project reported in Chapter 3.2 and Chapter 3.3, I implemented the experiments, analyzed data, and contributed to the manuscript.

The cross-platform benchmarking project, described in Chapter 4.1, is a large collaboration across multiple research groups and several hardware platforms. I represented one of the four trapped-ion platforms (the UMD_2 system) in the collaboration, participated in the design of the experiments, led data collection on UMD_2, the data analysis, and contributed to the manuscript.

I am the lead researcher in the project described in Chapter 4.2, where I designed and performance the first validation of a novel noise characterization protocol, proposed by collaborating theorists, on trapped-ion systems. I also developed and experimentally demonstrated a method to improve the performance of this protocol for trapped ions.

In Chapter 4.3, I developed a parallel entangling gate scheme on trapped ions using orthogonal modes. I designed and implemented the experiments, analyzed data, and wrote the manuscript.

Chapter 2

Experimental Apparatus

The fundamental component of a quantum computer is a qubit. To construct a quantum computer capable of universal computing tasks, a large number of qubits with long coherence time and the abilities to initialize and read out the qubit states as well as to implement a universal gate set are required. In this chapter, we briefly introduce the hardware architecture and the control system of a TIQC with up to 9 individually addressed qubits. We highlight the features of the device that enabled that work described in the next three chapters. More detailed discussion about this experimental setup can be found in Ref. [69, 88, 159, 188].

2.1 Qubit in an Ion

2.1.1 $^{171}Yb^{+}$ Hyperfine Qubits

The qubit is defined in the hyperfine ground states $|F = 1, m_F = 0\rangle \equiv |0\rangle$ and $|F = 1, m_F = 1\rangle \equiv |1\rangle$ of the $^2S_{1/2}$ manifold in the $^{171}Yb^{+}$ ion (See Fig. 2.1). The qubit states are first-order insensitive to and only have weak second-order dependence on the magnetic field. The qubit phase coherence time is measured to be about 1 second. State initialization and readout can be achieved via optical pumping and state-dependent fluorescence detection respectively using 369 nm light with appropriate sidebands through the couplings between the $^2S_{1/2}$ and

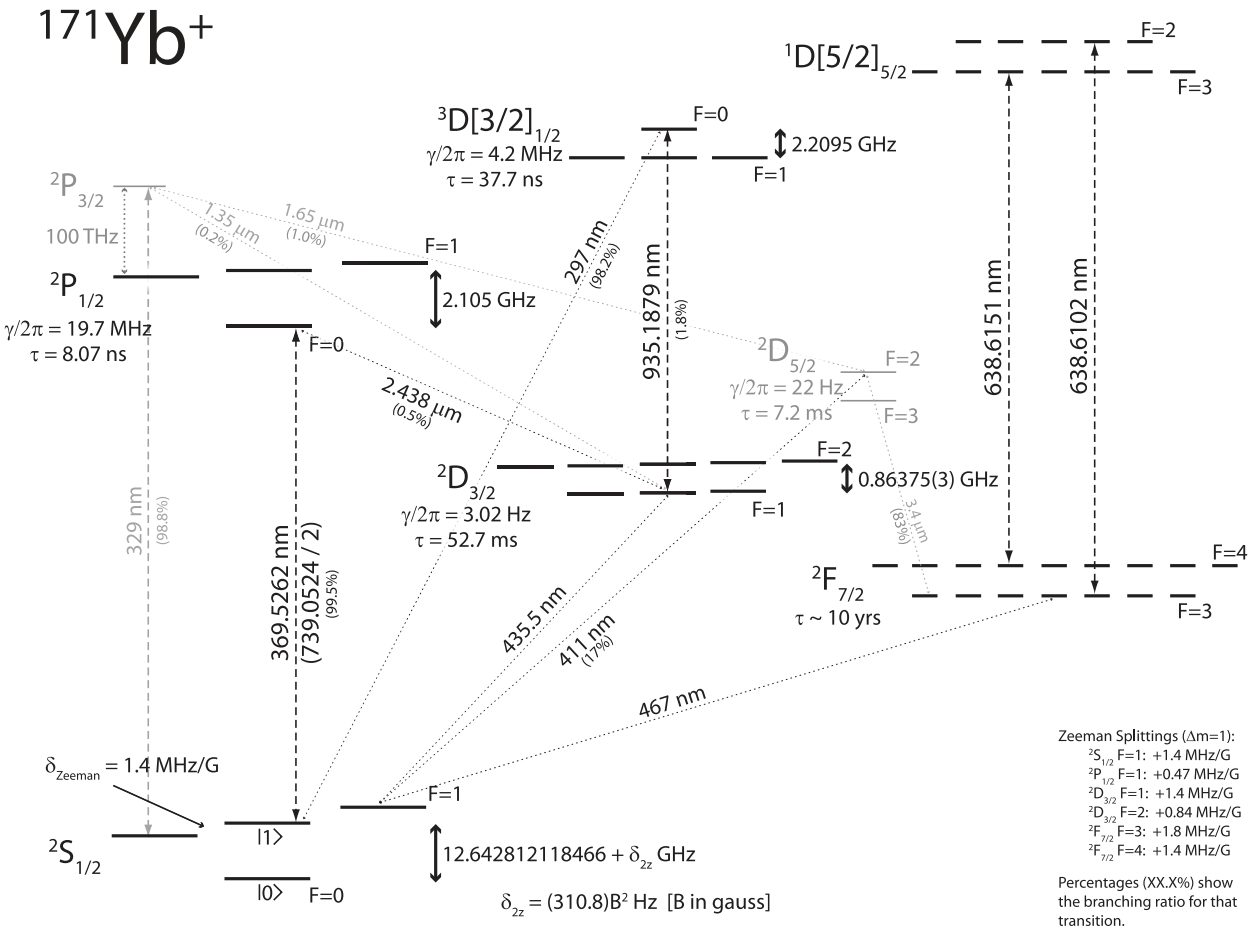

Figure 2.1: $^{171}Yb^{+}$ level diagram. The qubit is defined in the hyperfine ground states $|F = 1, m_F = 0\rangle \equiv |0\rangle$ and $|F = 1, m_F = 1\rangle \equiv |1\rangle$ of the $^2S_{1/2}$ manifold. Doppler cooling, optical pumping and state-dependent detection are implemented with the 369nm laser light with appropriate sidebands respectively. There is a small probability that the qubit may fall into a dark state in the $^2D_{3/2}$ manifold. A re-pump beam at 935 nm is used to bring the qubit back to $^2S_{1/2}$.

$^2P_{1/2}$ manifold [251].

2.1.2 Ion Trapping

Due to Earnshaw's theorem, charged particles cannot be trapped by static electric fields in three spatial directions. Most ion traps use either dynamic electric fields [196], usually at Radio Frequency (RF), or static magnetic and electric fields for confinement [40]. In this experiment, the ions are confined in a Linear Paul trap, a type of RF trap, generated by four segmented blade electrodes as shown in Fig. 2.2 [270], where two of them are connected to

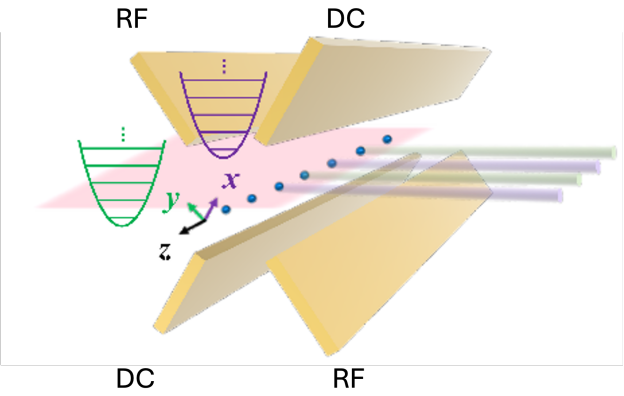

Figure 2.2: Linear Paul trap with blades.

an RF source and the other two are connected to a DC source. In the z direction along the blades, the ions experience weak harmonic confinement generated by DC voltages applied to the trap blades, and therefore form a chain along this direction. In the radial directions, i.e., the plane perpendicular to the chain spanned by axis x and y, the ions are trapped in a pseudo-potential that is approximately harmonic along the two radial principal axes, x and y.

The N ions in the chain act as a set of coupled harmonic oscillators along each principal axis x, y, z as the result of the confining potential and the Coulomb repulsion between the ions, generating N normal motional modes along each principle axis. Normal modes on different principal axes are independent [135, 174]. The eigenfrequencies of the motional modes in x and y directions do not overlap due to the anisotropicity of the pseudo-potential in the $x - y$ plane. Motional frequencies in the z direction are much lower than that in x and y. Normal modes give rise to motional sidebands on carrier transition, which couples the two qubit states on resonance. In this experiment, the typical frequency of the radial modes are around 3 MHz. Fig. 2.3 shows the carrier transition, the blue and red motional sidebands generated by x and y modes in the frequency domain.

During ion loading, the hot neutral Yb atoms are loaded from an oven below the trap, and ionized by the 399nm laser light and the 369 nm or 355nm laser light through a two-step ionization process. The hot Yb^+ ion cloud is first Doppler-cooled by a high-power 369nm

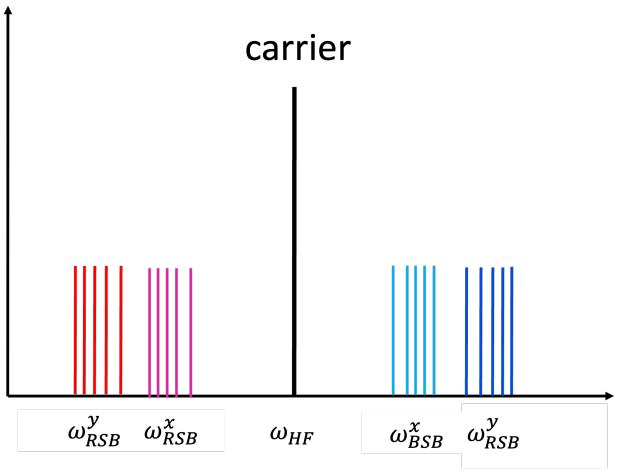

Figure 2.3: Red and blue motional sidebands for x and y modes. Carrier transition marked by a black solid line couples the qubit $|0\rangle$ and $|1\rangle$ state on resonance. the sidebands are about 3MHz away from the carrier transitions.

cooling beam that is 300 MHz red-detuned (far-detuned) from the $S_{1/2}$ to $P_{1/2}$ transition, and then further cooled by an unsaturated 369nm beam which is 10 MHz red-detuned (near-detuned) to Doppler limit.

2.2 Coherent Operations

Coherent operations, such as coherent population transfer between qubit states are entanglement generation between qubits, are driven by two counter-propagating Raman beams (Fig. 2.5). In this section we briefly discuss how to implement arbitrary single qubit rotations and two-qubit entangling gates in this architecture.

2.2.1 Single-Qubit Operation

Rabi flops between the two qubit states can be driven by directly microwave at $\omega_{HF} = 12.642$ GHz or via a Raman transition by two laser beams with a beatnote at ω_{HF}. Although the individual addressing of ions with microwave has been explored [11, 165, 253], it is more straightforward to use laser for individual addressibility.

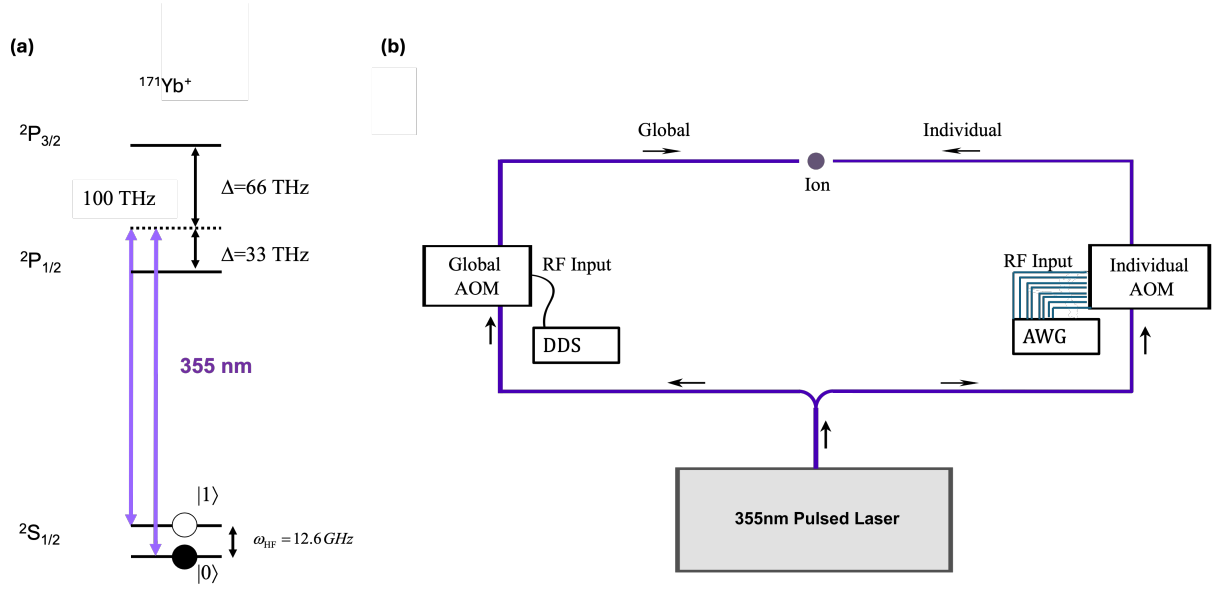

Figure 2.4: (a) Raman transition between the qubit levels driven by a pair of 355nm beams with a beatnote at ω_{HF}. (b)The pair of Raman beams is derived from 355 nm pulse laser. The beam in the global beam path is modulated by an RF signal generated from a DDS. Each beam in the beam array in the individual path can be independently controlled by an RF signal generated by the multi-channel AWG modules.

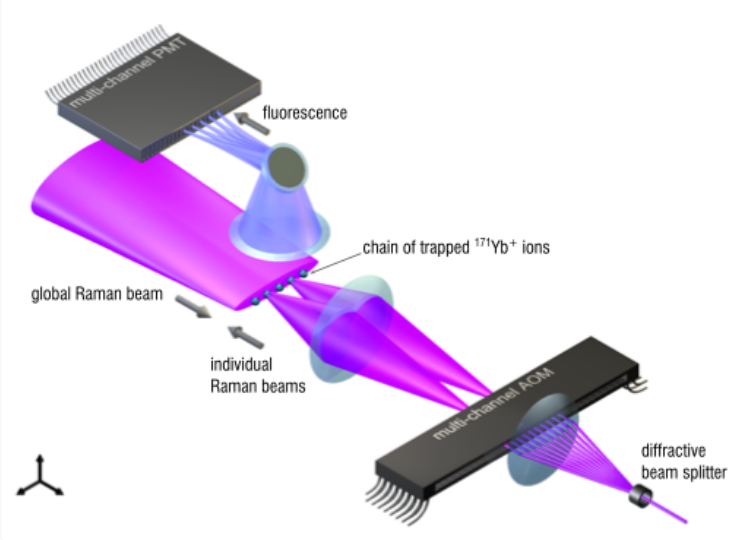

Figure 2.5: Sketch of the optical setup of the system.

Fig. 2.4 (a) shows the stimulated Raman transition between $|0\rangle$ and $|1\rangle$ can be driven by a pair of 355nm beams with a beatnote at ω_{HF}. This is a two-photon process where the two qubit states are weakly coupled to multiple excited states in the $^2P_{1/2}$ and the $^2P_{3/2}$ manifolds. The detuing of the laser from these two manifolds are chosen such that stark shift from the off-resonant driving of these transitions cancel out [182]. Although this can be experimentally implemented with continuous wave lasers, we use a mode-locked pulse laser at 355 nm for straightforward beatnote generation and higher optical power. In the frequency domain, the pulse laser generates a frequency comb consisting of many equally spaced comb lines. The repetition rate of our pulse laser is such that a single frequency comb can not drive a Raman transition between the qubit levels. Instead, we split the output light into two beams. They are modulated independently before recombining at the ions, as shown in Fig. 2.4 (b). The two frequency combs are offset from each other such that the beatnote between nth comb-line in one beam and the 108th comb-line in the other beam equals to ω_{HF}. There are many pairs of comb-lines between the two beams that satisfy this condition, and all pairs of comb-lines drive the Raman transition at the same time. The beam in the "Global" path illuminates the entire ion chain. The light in the "individual" path is further split into 10 smaller beams by a 10-way diffractive element, and each small beam is coupled into one channel in a 32-channel AOM and modulated by its own RF control signal. The frequency, amplitude and phase of each output beam can be individually controlled. The output beam array of the AOM is then tightly focused onto the ion chain, where each beam illuminates one ion qubit.

The rotation gate $R(\theta, \phi) = e^{-i\theta/2(\cos\phi\sigma_x + \sin\phi\sigma_y)}, \theta \in [0, \pi], \phi \in [0, 2\pi]$ can be implemented with the Raman transition. σ^x and σ^y are the Pauli X and Y operators. Arbitrary θ and ϕ can be achieved by varying the pulse duration and relative phase between the laser and the qubit. $R_z(\theta) = e^{-i\theta/2\sigma_z}$ rotations are implemented classically by adjusting the laser phase [69].

2.2.2 Two-Qubit Operation

There exists many schemes for implementing entangling gates in trapped ions, such as the Cirac-Zoller gate [57], the light shift gate [14, 163], and the Mølmer-Sørensen (MS) gate [230]. In MS gate scheme, entanglements between qubits are generated by entangling qubits with the collective motion of the ion crystal during the gate and disentangling the motion from the qubits at the end of the gate, leaving only the qubits entangled with each other. This operation can be realized by lasers, microwaves, or radio frequency waves. The advantage of using laser beams over the other options is the ability to entangle arbitrary pairs of ions of choice.

The entanglement between the qubit state of an ion and the motion of the ion chain can be created by biochromatic light driving both the red- and the blue motional sidebands with symmetric detuning from the carrier, generating a spin-dependent momentum kick on the ion. In an N-ion chain, $\omega_k, k \in \{1, 2, ..., N\}$ as the eigenfrequency of the motional modes in x direction. $\omega_{HF}+\mu$ and $\omega_{HF}-\mu$ are frequencies of the blue and red sidebands near detuned from the x motional modes. Since the typical Rabi frequencies of the sideband transitions during an entangling gate are much smaller than the frequency separation between motional modes in different spatial directions, we can ignore the off-resonant excitation of y and z modes here. In our experiment this is realized by the two counter-propogating raman beams with beatnote frequencies at $\omega_{HF} + \mu$ and $\omega_{HF} - \mu$. In order to induce the momentum kick in the x direction, the difference between the vectors of the two Raman beams $\Delta\vec{k} = \vec{k_1} - \vec{k_2}$ must have none-zero projection in x. The orientation of the Raman beams with respect to the trap axis in this experiment is shown in Fig. 2.6.

In the interaction picture, after the rotating wave approximation and ignoring the weak off-resonant excitation of the carrier transition, the Hamiltonian of the spin-dependent force on ion i can be written as

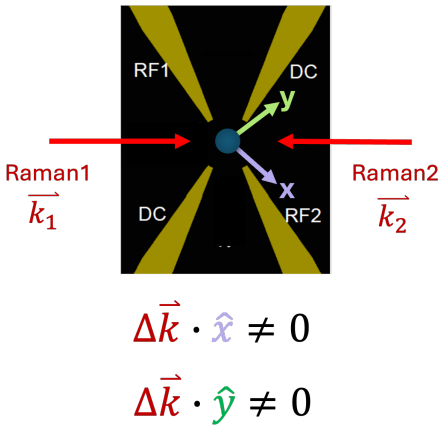

Figure 2.6: The orientation of the Raman beams with respect to the trap axis. $\Delta\vec{k}$ has non-zero projection in both x and y. The figure shows the cross-section of the trap looking into the z axis. The yellow diagonal structures are the trap blades.

$$H_{SDF}(\tau) = \sum_{k=1}^{N} \Omega_i(\tau)\eta_k^i \cos(\mu\tau - \phi_i^m)(a_k e^{-i\omega_k \tau} + h.c.)\hat{\sigma}_i^{\phi_i^s - \pi/2}, \tag{2.1}$$

where $\hat{\sigma}^{\phi} = \hat{\sigma}^x \cos\phi + \hat{\sigma}^y \sin\phi$. $a_k^\dagger$ and a_k are the creation and annihilation operator for mode k in x direction. Ω_i is the Rabi frequency of qubit i. η_k^i is the Lamb-Dicke parameter coupling qubit i to mode k. ϕ_i^m and ϕ_i^s are determined by the laser phases. Eq. (2.1) is similar to the Hamiltonian of a driven quantum harmonic oscillator, except that the direction of the driving force has an extra dependency on the spin state of the qubit through $\sigma_i^{\phi_i^s - \pi/2}$.

An XX gate of angle χ_{ij} ($R_{XX}(\chi_{ij}) = e^{i\chi_{ij}(\tau)\hat{\sigma}_i^x\hat{\sigma}_j^x}$) between qubit i and j can be generated by applying the spin-dependent kick described by Eq. (2.1) on two ions $\{i, j\}$ at the same time. The unitary for interaction can be derived via the Magnus expansion

$$U_{ij}(\tau) = \exp\left[\sum_{i'=i,j}\sum_{k=1}^{N}\left(\alpha_{i'k}(\tau)\hat{a}_k^\dagger - \alpha_{i'k}^*(\tau)\hat{a}_k\right)\hat{\sigma}_i^x + i\chi_{ij}(\tau)\hat{\sigma}_i^x\hat{\sigma}_j^x\right], \tag{2.2}$$

where $\phi_i^s = \pi/2$ and $\phi_i = -\phi_i^m$. τ is the gate time, which is usually $200 - 300$ μs in our

experiment, and

$$\alpha_{ik}(\tau) = -i\eta_{ik}\int_0^\tau \Omega_i(t)\cos(\mu t + \phi_i)\mathrm{e}^{i\omega_k t}dt, \tag{2.3}$$

and

$$\chi_{i,j}(\tau) = \eta_{ik}\eta_{jk}\sum_{k=1}^{N}\int_0^\tau dt\int_0^t dt'\Omega_i(t)\Omega_j(t')\sin(\omega_k(t-t'))\cos(\mu t+\phi)\cos(\mu t'+\phi). \tag{2.4}$$

Disentangling qubits and motion at the end of the entangling gate requires all $\alpha_{ik}(\tau)$ to be zero. This can be achieved by modulating the amplitude (Ω), phase (ϕ), and frequency (μ) of the laser pulse, respectively, or a combination of these [103, 166, 208, 223, 269]. Using the amplitude modulation scheme [56], we find pulse solution $\Omega_i(t) = \Omega_j(t) = \Omega(t)$ such that $\alpha_{ik}(\tau)$=0 for $i \in \{i, j\}$ and $k \in \{1, 2, ..., N\}$. We call such a pulse solution a gate solution. Aamplitude- and frequency-modulate gate pulses are used in our experiment as well.

A universal gate set is a collection of quantum gates that can be used to approximate any unitary to an arbitrary accuracy. The $R_{XX}(\chi)$,$R(\theta, \phi)$, and $R_z(\theta)$ form an universal gate set.

2.3 Control System Architecture

The control system of a TIQC should be able to control the trapping and cooling of ions, execute an experimental sequence, and acquire data. This is realized by the main control software developed in Igor Pro from WaveMetrics together with a hierarchy of electronics, such as FPGAs, frequency synthesizers, and electro-optical devices. The sketch of the control system is shown in Fig. 2.7.

A standard experimental sequence usually involves ion cooling, qubit initialization, coherent operation, and detection. During each step, different lasers and electronic devices need to be switched on for a specific amount of time. The timing of the experiment is coor-

dinated by the Igor program and the Sequencer FPGA. When receiving the instruction for an experiment, Igor translates the entire experiment into a sequence of device names and activation time, which is then sent to the Sequencer FPGA. The Sequencer FPGA constructs TTL pulses, which activate devices at high voltage and deactivate them at low voltage, and ensure that the TTL signals are delivered to the correct devices at the exact right times.

AWGs have the ability to generate arbitrary waveform and is an essential piece of equipment for implementing different types of quantum gates. In our experiment, each of the individual Raman beams is independently modulated by an RF signal in the 32-channel AOM. The control RF signals are generated by three Keysight AWG modules (M3202A) with four independent AWG channels on each module. When receiving a gate sequence, Igor complies the waveform for the control signals and upload them to the AWG channel controlling the relevant individual beams. The AWG outputs are amplified and combined with TTLs before entering the AOM. This set up allows us to switch on and off arbitrary beams, and control their amplitude, frequency and phase individually. Usually we use nine AOM and AWG channels maximally.

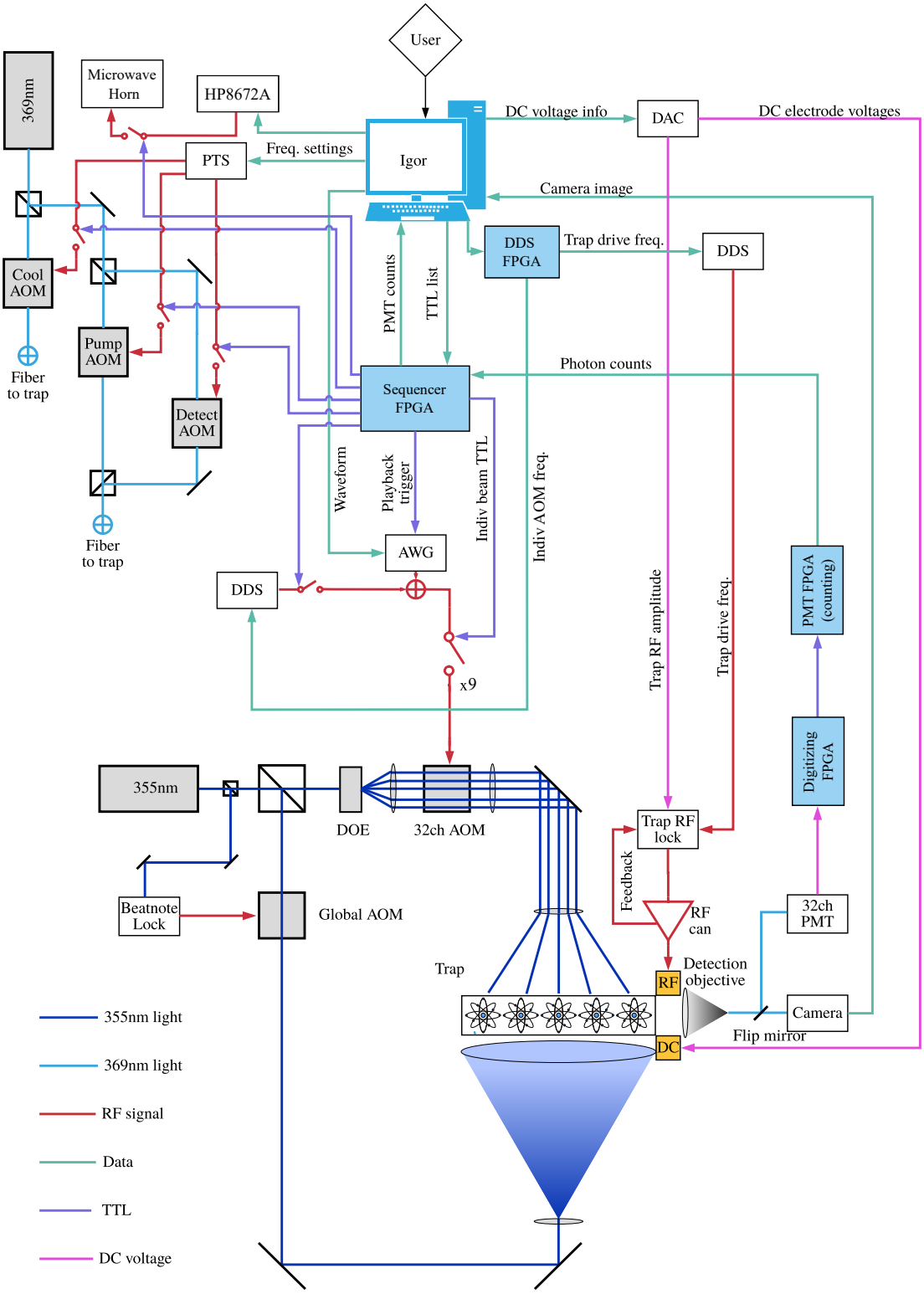

Figure 2.7: Experimental control system layout. Figure is from Ref. [188].

Chapter 3

Implementations of Early Quantum Applications on a TIQC

Although it is promising that quantum computers may provide speedups over classical computers on a wide variety of tasks, there are few readily available algorithms. Efficient quantum methods need to be tested and further developed to unlock the potential of quantum computers. In this chapter, we discussed three proof-of-principle demonstrations of early quantum applications with the potential to be applied to larger-scale problems with practical values.

3.1 Quantum Approximate Optimization Algorithm (QAOA) on Graph Problems

Combinatorial optimization problems on graphs have broad applications in science and engineering. The Quantum Approximate Optimization Algorithm (QAOA) is a method to solve these problems on a quantum computer by applying multiple rounds of variational circuits. However, there exist several challenges limiting the application of QAOA to real-world problems. We demonstrate on a trapped-ion quantum computer that QAOA results improve with the number of rounds for multiple problems on several arbitrary graphs. We also demonstrate an advanced mixing Hamiltonian that allows sampling of all optimal solutions with predetermined weights. Our results are a step towards applying quantum algorithms to real-world problems.

3.1.1 Graph Optimization and Standard QAOA

Combinatorial optimization problems on graphs are ubiquitous in fields of science and engineering, such as bioinformatics [74, 261], earth science [126], logistics [215], resource management [79], telecommunications [205], e-commerce [81, 262] and others. Efficient classical algorithms for solving many of these problems are not known, and quantum computers can potentially provide an advantage. The Quantum Approximate Optimization Algorithm (QAOA) has been used in several demonstrations to solve combinatorial as well as other types of optimization problems [2, 23, 117, 156, 161, 193, 194, 203, 257]. QAOA is a quantum-classical hybrid algorithm that produces high-quality approximate solutions [83]. Even though it does not always guarantee an advantage over classical algorithms, QAOA can achieve a provable quadratic speedup in oracle calls when it is equivalent to Grover's algorithm [192], and numerical evidence shows that it can provide a polynomial speedup in some problems [71]. It has also been argued that even the output distribution from a one-round QAOA circuit is hard to sample classically [84]. QAOA is also able to generate

approximate answers with low-depth circuits, which makes it valuable for implementations on near-term quantum devices.

In QAOA, two non-commuting Hamiltonians, the problem-dependent Hamiltonian H_A and the mixing Hamiltonian H_B, are applied repeatedly to a chosen initial state $|\psi_{\text{initial}}\rangle$ in a bang-bang protocol. The final output state is an approximate ground state of H_A as well as a solution to the optimization problem.

$$|\psi_{\text{final}}\rangle = \prod_{i=1}^{p} e^{-iH_B\beta_i} e^{-iH_A\alpha_i} |\psi_{\text{initial}}\rangle \tag{3.1}$$

α_i and β_i are real variational parameters, and p is the number of QAOA rounds. The variational parameters are optimized classically to minimize the expectation value $\langle\psi_{\text{final}}|H_A|\psi_{\text{final}}\rangle$. $|\psi_{\text{initial}}\rangle$ is the ground state of H_B. In standard QAOA, H_B is the n-qubit transverse-field Hamiltonian

$$H_B^{\text{transverse}} = \sum_{i=1}^{n} \sigma_i^x, \tag{3.2}$$

where σ_i^x is the Pauli X matrix acting on qubit i.

In theory, QAOA performance improves as p is increased. However, increasing p can degrade the results in practice when the experimental errors introduced by deeper circuits outcompete the theoretical QAOA gain. Additionally, if the connectivity of the graphs does not match the qubit connectivity of the quantum hardware, the overheads required to map these nonnative graphs to the qubits also greatly increase the circuit depth. Moreover, the standard QAOA often provides only a subset of the ground states, while many applications require knowledge about all of them.

The first result of our work is to show that the probability of finding a ground state with standard QAOA increases with p, up to $p = 3$, on a trapped-ion quantum computer for optimization problems defined on arbitrary graphs. Previous experimental works have demonstrated QAOA results improving with p on hardware-native graphs [23, 117, 156, 161], while real-world graph problems are often hardware-nonnative.

The second result of our work is to demonstrate that employing advanced mixing Hamiltonians in QAOA can allow one to access a broader range of classically hard optimization problems. The recently proposed Grover mixer QAOA (G-QAOA) [19, 231] is capable of generating a superposition of all ground states with probabilities determined by their weights, which are defined in the optimization problem and provided as inputs. This feature is referred to as fair sampling. G-QAOA can be applied to both unweighted and weighted graph problems. The n-qubit Grover mixer takes the form

$$H_B^{\text{Grover}} = \prod_{i=1}^{n} \frac{1 + (1-2q)\sigma_i^z + 2\sqrt{q(1-q)}\sigma_i^x}{2}, \tag{3.3}$$

where q is related to the numerical weight assigned to all qubits, with $q = 0.5$ corresponding to unweighted problems. Other important tasks relying on fair sampling include satisfiability (SAT)-based membership filters [12, 72, 255], proportional model sampling [99], machine learning [80, 124], and sampling the ground states of arbitrary classical spin Hamiltonians [98, 210]. Although in theory G-QAOA fairly samples ground states at any p, the total probability of finding ground states increases with p. While previous works have experimentally demonstrated one round of G-QAOA in Hamiltonian optimization problems on unweighted graphs [97, 197], we apply G-QAOA to both weighted and unweighted graph problems up to $p = 2$ on arbitrary graphs, and quantitatively evaluate the experimental fair sampling results.

We implemented the experiments on our trapped-ion device with up to five qubits.

3.1.2 Higher Round QAOA on graph problems

In this section, we focus on finding a *maximum cut* on the bridge graph and an *edge cover* on the triangle, paw and square graphs with standard QAOA. All graphs discussed in this section are unweighted. A graph G is defined by a set of vertices $v \in V$, $|V| = N_v$, and a set of edges $e \in E$, $|E| = N_e$. A *maximum cut* is a partition of all vertices into two

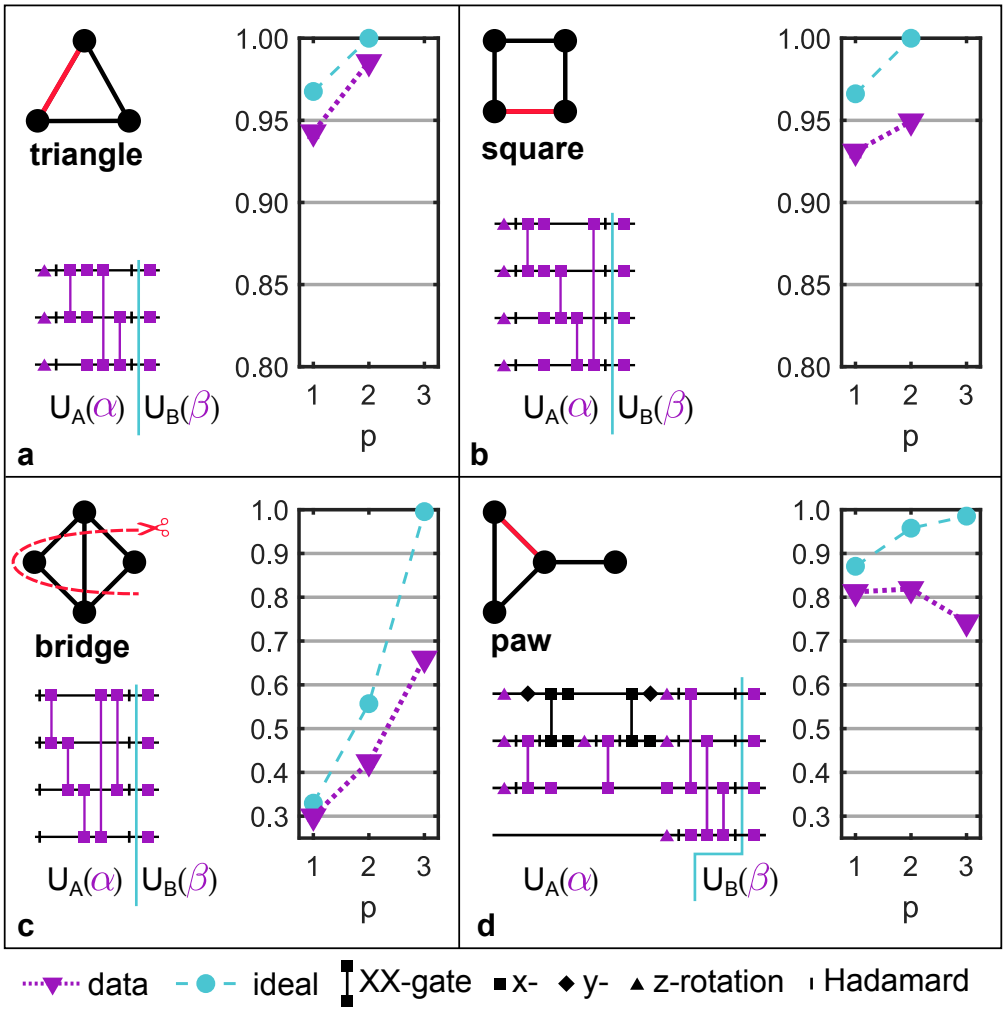

Figure 3.1: The plots give the probability to find a solution on the trapped-ion machine compared to the ideal result for different numbers of QAOA rounds p. The graphs are indicated in the top left corner, i.e. the triangle (a), square (b), bridge (c) and paw graph (d). For edge cover problems (a,b,d) the black links show example solutions, for the Max-Cut problem (c) the red line indicates the unique cut. Circuits show one round of the problem unitary $U_A = e^{-iH_A\alpha}$ and the mixer unitary $U_B = e^{-iH_B\beta}$, with purple gates parameterized by α or β. The values of parameters α_i and β_i are listed in Appendix A.1. All qubits are initialized in the x-basis and measured in the z-basis (not shown). Statistical error bars on the data are calculated from 4000 experimental shots per data point. The error bars are all smaller than 1% in value and smaller than the symbols in the figure. The dashed lines are a guide to the eye.

standard QAOA					G-QAOA			
graph		$p=1$	$p=2$	$p=3$	graph		$p=1$	$p=2$
triangle	sim	0.968	1		triangle	sim	0.781	0.999
	exp	0.943(2)	0.986(1)			exp	0.739(2)	0.751(2)
square	sim	0.966	1		square	sim	0.770	0.801
	exp	0.931(1)	0.949(1)			exp	0.668(1)	0.692(1)
paw	sim	0.871	0.958	0.985	paw	sim	0.645	0.867
	exp	0.812(2)	0.819(1)	0.743(2)		exp	0.548(2)	0.551(2)
bridge	sim	0.330	0.557	0.996	paw (weighted)	sim	0.105	0.835
	exp	0.300(3)	0.424(4)	0.660(4)		exp	0.235(1)	0.421(1)
					square (weighted)	sim	0.310	0.758
						exp	0.255(1)	0.497(1)

Table 3.1: Simulated and experimental probabilities of finding a ground state for different p by standard QAOA (left half) and G-QAOA (right half) for the edge cover (triangle, paw, and square graph) and Max-Cut problems (bridge graph). The errors are the statistical 68.3% confidence interval.

complementary sets where the number of edges between them is maximized. An *edge cover* is a subgraph $G' \subseteq G$ in which every $v \in V$ is connected to at least one edge E' included in G'. A graph can have multiple *maximum cuts* or *edge covers*. Although brute force solutions of the *maximum cut* problem on planar graphs and the *edge cover* problem can be carried out in polynomial time, the algorithms we employ do not exploit this structure.

Based on the graph problem to be solved, we construct the problem-dependent Hamiltonian H_A such that minimizing H_A gives the solutions of interest. When mapping the graphs onto a quantum computer, a qubit can represent either an edge or a vertex. In Max-Cut problems, the qubits encode the vertices. Each computational basis state represents a partition of V with all vertices corresponding to qubits in state $|0\rangle$ in one set and the rest in the other set. The probability of finding each ground state is the population of the corresponding quantum state in $|\psi_{\text{final}}\rangle$. The problem Hamiltonian H_A for Max-Cut problems is

$$H_A^{\text{maxcut}} = \sum_{(i,j)\in E} \sigma_i^z \sigma_j^z, \tag{3.4}$$

where σ^z is the Pauli Z operator. If (i,j) is an edge between sets, $\sigma_i^z \sigma_j^z = -1$.

In an edge cover problem, each qubit encodes a unique edge $e \in E$. Therefore, each computational basis state encodes a unique G' where the qubit state $|0\rangle$ ($|1\rangle$) means that the corresponding edge is included (not included) in G'. H_A encoding the edge cover problem is

$$H_A^{\text{ec}} = \sum_{v \in V} \prod_{e \in E(v)} \frac{1 - \sigma_e^z}{2}, \tag{3.5}$$

where $E(v)$ is the set of edges incident on vertex v in G. For a subgraph G', the product term for each v in H_A^{ec} is 0 if there is at least one edge incident on v, otherwise it is 1. Therefore the energy of H_A^{ec} is minimized to 0 if and only if G' is an edge cover.

In the experiment, the system is first prepared in the ground state of H_B in equation (3.2), $|\psi_{\text{initial}}\rangle = |+ + ... +\rangle$ with $|+\rangle = \frac{1}{\sqrt{2}}(|0\rangle + |1\rangle)$, by applying a Hadamard gate to each qubit. Then the system unitarily evolves under H_A and H_B alternately before being measured in the computational basis.

The results are shown in Fig. 3.1 and in Table 3.1 (left column). In the Max-Cut problem on the bridge graph, the probability of finding a *maximum cut* clearly improves with p [Fig. 3.1(c)], despite the p-fold increase in the number of gate operations. Similarly, the probabilities of finding one *edge cover* on the triangle and square graph also increase with p [Fig. 3.1(a,b)].

However, on the paw graph, the probability of finding an *edge cover* only improves marginally for $p = 2$ and drops for $p = 3$ [Fig. 3.1(d)]. In this problem, the implementation of H_A^{ec} requires seven two-qubit entangling gates, the most among all four problems, and the additional gate error outweighs the theoretical gain with increasing p. The question then arises whether there are alternatives to increasing p that will improve the solution probability. One such idea is to use more sophisticated mixers, an example of which is the Grover-mixer given in equation (3.3). While, as we will see, this does not increase the solution probability for a fixed gate depth, it does enable the solution of a new class of graph optimization problem—sampling problems.

		(N_g)	2	3	4	5	6	7
triangle	$p=1$	QAOA	2.58	5.00	10.16			
		G-QAOA	3.15	5.87	11.28			
	$p=2$	QAOA	10.43	26.48	60.50(1)			
		G-QAOA	3.11	5.82	11.30(2)			
paw	$p=1$	QAOA	3.13	6.15	11.65	33.34		
		G-QAOA	4.12	7.19	11.91	21.54		
	$p=2$	QAOA	6.44	14.93	29.20(6)	66.0(1)		
		G-QAOA	4.09	7.20(1)	11.93	21.61(3)		
square	$p=1$	QAOA	2.53	4.28	6.55	9.78	15.05	25.09
		G-QAOA	3.16	5.22	7.84	11.4(1)	16.82	28.12
	$p=2$	QAOA	6.64	15.33	28.41	53.7(1)	171.1(5)	493(1)
		G-QAOA	3.25	5.36	7.99	11.56	16.87	27.69

Table 3.2: Number of draws required to see N_g ground states on unweighted graphs. Average and error bars are calculated from 100,000 independent trials. All error bars less than 0.01 are not included in the table. In comparison, if this similar counting test is done on random guessing ($p = 0$), it will take 16.64(3), 36.58(6) and 41.40(4) of draws in these three graphs to get all ground states.

3.1.3 Sampling with G-QAOA on unweighted graphs

All four unweighted graph problems studied in Sec. 3.1.2 have more than one solution, but we observe that the standard QAOA favors only one. G-QAOA samples all ground states with equal probability at any p on unweighted graphs. In this section, the goal is to find all solutions for the three edge cover problems studied in Sec. 3.1.2 by using G-QAOA. H_A^{ec} is given in equation (3.5). But now H_B is the Grover mixer for unweighted graphs given in equation (3.3) with $q = 0.5$. The circuit in Fig. 3.2 shows the 3-qubit Grover mixer for unweighted problems used in the edge cover problem on the unweighted triangle graph. Fig. 3.3 shows the 4-qubit Grover mixer. Variational parameters α and β for each problem are listed in Table A.1 in Appendix A.1. These optimal parameter sets are derived from a noise-free theory using exact numerics.

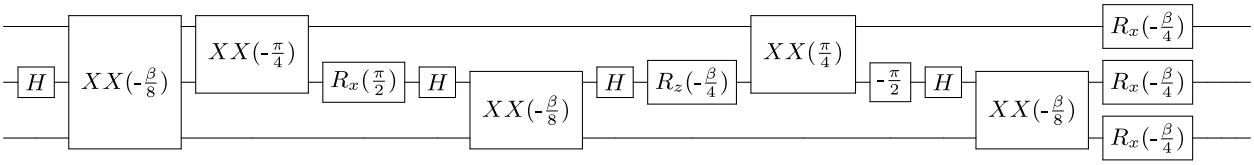

Figure 3.2: 3-qubit Grover mixer for unweighted problems in equation (3.3) with $n = 3$ and $q = 0.5$.

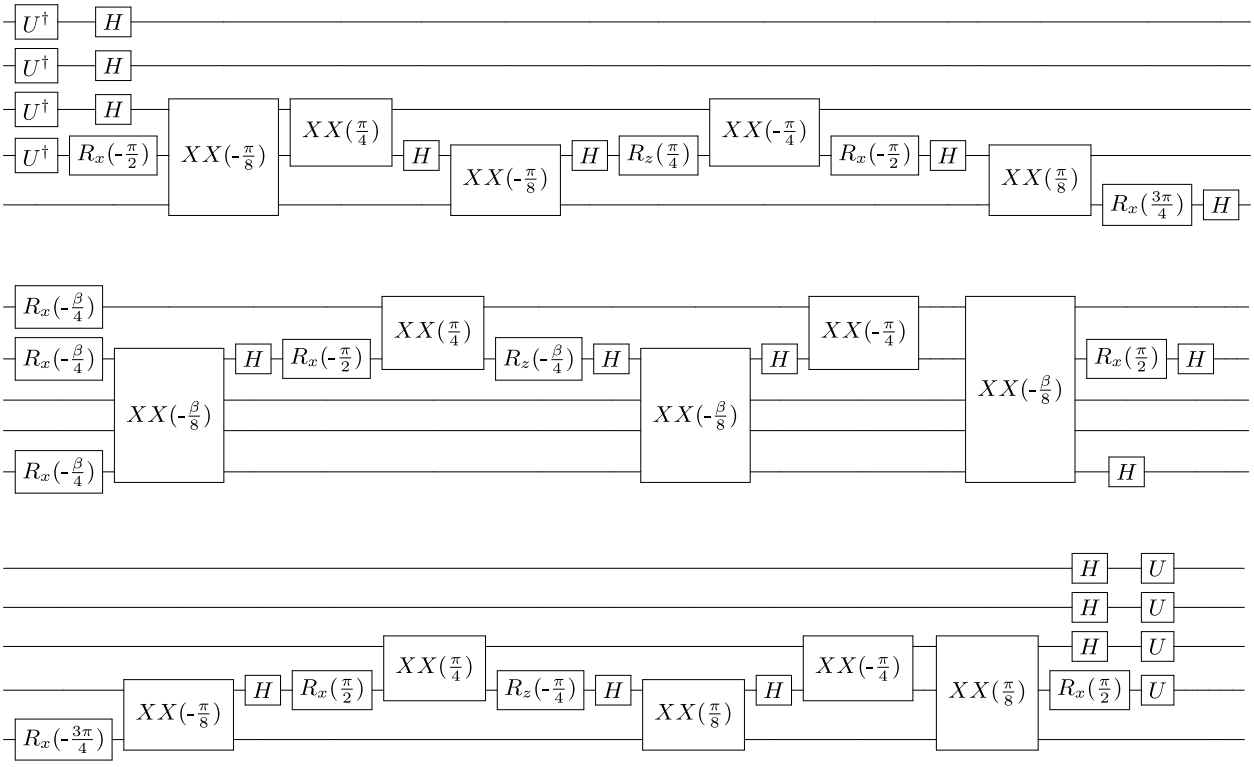

Figure 3.3: 4-qubit Grover mixer in equation (3.3) with $n = 4$ and arbitrary q. The last qubit acts as an ancilla qubit.

Fig. 3.4 shows the individual probabilities of finding each ground state for each problem, and Table 3.1 gives the total probability of finding all ground states. The blue bars in Fig. 3.4 demonstrate our claim that standard QAOA favors one solution more than others, while the purple bars show that G-QAOA does not. In the G-QAOA result for the edge cover problem on the triangle graph at $p = 1$, the experiment closely approximates the simulation. Furthermore, we see a small improvement in the total ground state probabilities at $p = 2$ compared with $p = 1$ for all three graphs despite the deeper circuits at higher p.

Fairness describes how well the experimentally sampled distribution represents the ideal distribution. The fair sampling of ground states with equal probabilities provides a convenient method to enumerate all ground states of a problem. One measure of the efficiency of the enumeration is the average number of experimental shots required to observe each ground

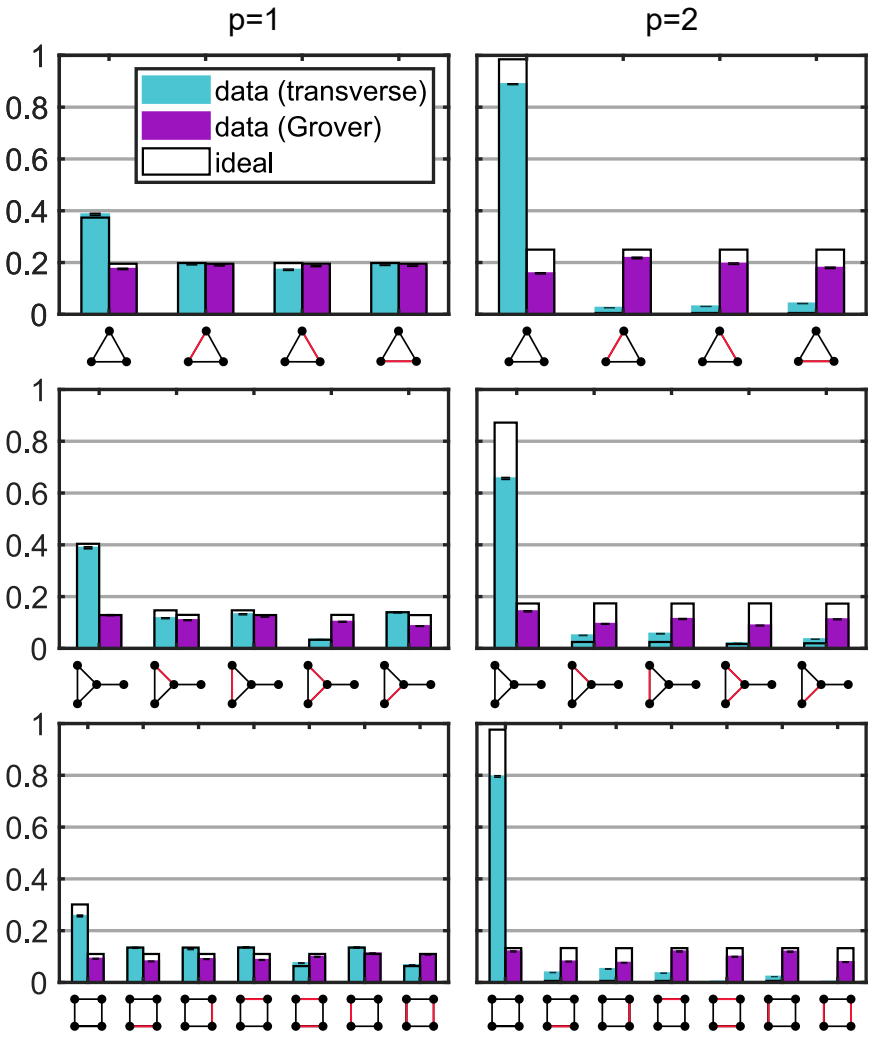

Figure 3.4: Simulated and experimental probabilities of finding each ground state by standard QAOA and G-QAOA for the edge cover problems on the triangle, paw, and square graph. Each plot compares the individual probabilities of finding each ground state at the same p for the same problem between standard QAOA and G-QAOA. Different *edge covers* are illustrated at the bottom of each plot on the horizontal axis, with edges included in each specific *edge cover* colored in black and edges not included colored in red. Simulated probabilities are delineated in contour with solid black lines, overlapping with corresponding experimental data plotted with colored bar without any outline. Error bars are calculated from 4000 experimental shots and are shown as short black dashes.

state at least once. To estimate this, we sample the states from the experimentally measured distributions on a classical computer. For each experimental distribution, we record the number of random draws required to observe any N_g different ground states at least once, varying N_g from 2 to the total number of ground states. For each N_g we repeat the procedure for 100,000 times to determine the average number of draws and the uncertainty.

Table 3.2 shows that, at $p = 1$, G-QAOA and QAOA perform similarly at enumerating ground states, with QAOA being marginally more efficient in most cases. The only exception is the paw graph problem for $N_g = 5$, where the ground state with the smallest probability found by QAOA (the fourth ground state from the left, see Fig. 3.4) has considerably lower probability in both simulation and experiment than the ground state with the smallest probability found by G-QAOA. Since the efficiency of enumerating by sampling is limited by the ground states with the lowest probability, G-QAOA shows an advantage in this case. QAOA at $p = 2$ suppresses some ground states more strongly than at $p = 1$, and therefore has the worst results. G-QAOA at $p = 2$ shows results similar to G-QAOA at $p = 1$, with slight improvement seen in a few cases. This differs from the ideal prediction that the number of draws required should decrease from $p = 1$ to $p = 2$ for G-QAOA since the total probability of ground states grows. However, in experiment the total probabilities do not increase significantly due to decoherence (see Table. 3.1). For the same reason, we see that most often QAOA at $p = 1$ requires the least number of draws to find N_g ground states, while theory predicts that G-QAOA at $p = 2$ should have an advantage in most cases, especially when N_g is close to the total number of ground states. Nevertheless, G-QAOA at $p = 1$ and $p = 2$ still require fewer samples than random guessing to obtain all ground states.

3.1.4 Fair-sampling with G-QAOA on weighted graphs

In this section, we solve the edge cover problem when a numerical weight $(1 - q) > 0$ with $q \neq 0.5$ is assigned to all edges on the paw and square graph. The weight of each subgraph G' is defined as $P_{G'} = (1 - q)^{n'} q^{n-n'}$, where n' is the number of edges included in G'. G-QAOA

		$p=1$	$p=2$
unweighted	triangle	5754(32)	406(8)
	paw	328(4)	208(4)
	square	602(13)	192(4)
weighted	paw	38(1)	90(1)
	square	35(1)	45(1)

(a) Experimental data

		$p=1$	$p=2$
unweighted	triangle	6526(3259)	4337(943)
	paw	1882(217)	4044(702)
	square	2544(414)	2318(247)
weighted	paw	297(74)	1958(675)
	square	674(82)	1370(270)

(b) Synthetic data

Table 3.3: Number of shots to reject the fair sampling hypothesis by re-sampling from the experimental data and the synthetic data. The synthetic data is randomly drawn from the ideal distributions. Averages and error bars are calculated by repeating the "shots to reject" test 10 times.

samples all ground states, with squared amplitudes proportional to these weights.

H_A^{ec} is given in equation (3.5) as in the previous two Sections. H_B is the Grover mixer given in equation (3.3). The initial state is prepared by applying

$$U = e^{-i\sigma^y \sin^{-1}\sqrt{q}} \tag{3.6}$$

to each qubit in $|0\rangle$. Fig. 3.5 shows the G-QAOA results on a paw graph with $q = 0.7$ and a square graph with $q = 0.75$, and compares them to the ideal population distributions.

To allow direct fairness comparisons between results for problems with different numbers of ground states and different sample sizes N on weighted graphs, we need a metric that is insensitive to these problem specifics. Fairness of the sampling result can be quantified as the discrepancy between the ideal ground state distribution Q_2 and the experimentally measured ground state distribution Q_1, which is obtained by post-selecting out all ground states from 4000 experimental shots. The first method we adopt is the "shots to reject" method, proposed in Ref. [97], which is constructed based on the chi-squared (χ^2) test. By re-sampling from Q_1, the goal is to compute the number of samples, N^*, needed to reject the null hypothesis H_0 at a selected significance level. Here, H_0 is that Q_1 is sampled from Q_2. The more the experimental data Q_1 deviates from the ideal distribution Q_2, the smaller N^* will be. To find N^*, we follow the protocol described in Appendix A.2.

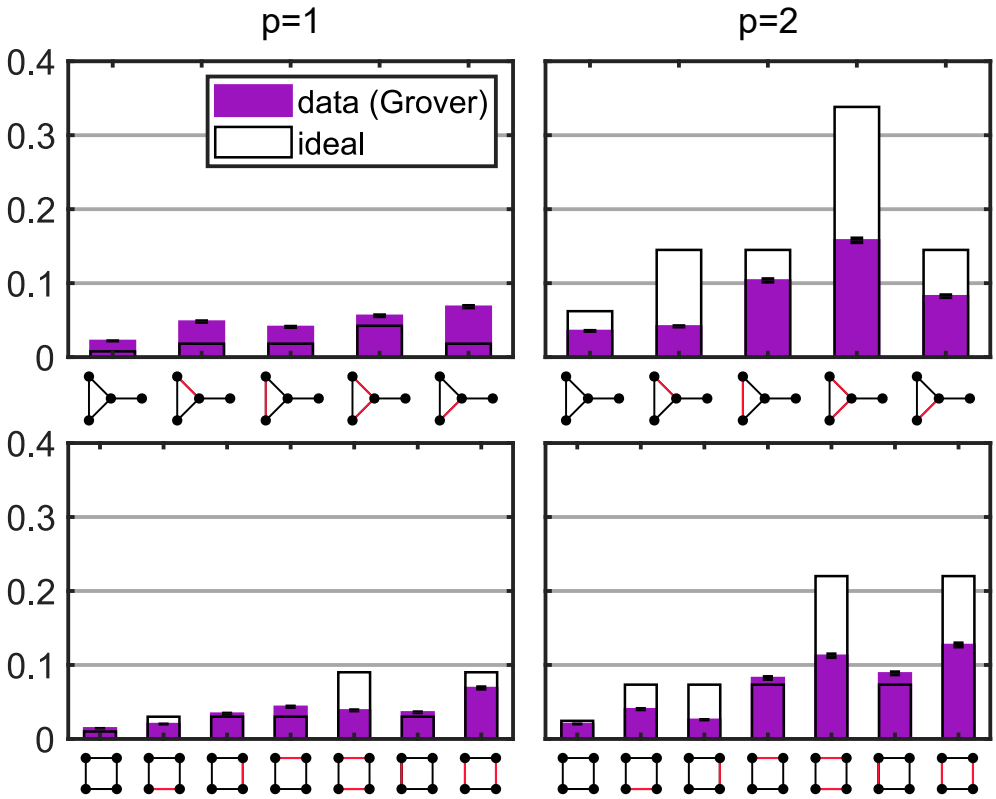

Figure 3.5: Simulated and experimental results from G-QAOA for the edge cover problem on the weighted paw (top) and square (bottom) graph. Error bars shown as short black dashes are calculated from 4000 experimental shots.

Table 3.3 shows the results for N^* from the experimental data with synthetic data for comparison, where synthetic data are random samples drawn from Q_2 on a classical computer. Some ground states on the weighted graphs have very small expected populations, causing H_0 to be more easily rejected in the χ^2 test, which contributes to the sampling results being overall less fair on the weighted than on the unweighted graphs for both experimental and synthetic data. We see a clear improvement in the fairness going from $p = 1$ to $p = 2$ in both weighted problems. This is due to G-QAOA boosting the probabilities of most of the ground states, including the least likely one, in each problem (see Fig. 3.5 and Table 3.1). When generating the synthetic data with a fixed number of draws from the entire population, the ground state counts are larger for $p = 2$ than $p = 1$, leading to different "shots to reject" results.

An alternative way to characterize the differences between probability distributions is

the Kullback–Leibler (KL) divergence. More details about KL divergence and the results for the KL divergence analysis are presented in Table A.2 in Appendix A.2. All trends are consistent with that seen in the “shots to reject" analysis.

3.1.5 Conclusion and Outlook

In this work, we experimentally demonstrated that the standard QAOA results improve with increasing p up to $p = 3$ in optimization problems on arbitrary graphs, and show fair sampling results of G-QAOA up to $p = 2$ on both unweighted and weighted graphs on a trapped-ion quantum computer. To push beyond these small demonstration problems, advances in fidelity and system size of the quantum hardware are crucial. Additionally, future studies on large-scale arbitrary graphs will challenge the connectivity of all hardware platforms, which highlights the importance of efficiently matching graphs and architectures.

Although G-QAOA does not show an advantage at enumerating the ground states over standard QAOA or when going to higher p on unweighted graphs due to experimental noise, we do observe that the total probabilities of ground states grow with increasing p in all cases. We also observe the fairness of sampling improves with increasing p in the two weighted problems. Future experiments could look at the relative advantage provided by more advanced mixers, such as the QED-inspired mixer designed for constrained flow problems [264], follow general guidelines to engineer mixers that ensure solutions satisfy desired constraints [121] or symmetries [221], and study circuits which preserve specific physical symmetries in optimization problems in fermionic systems [95].

3.2 Real-time quantum calculations of phase shifts

In recent years, the idea of simulating quantum field theory with quantum computers has gained considerable interest [201]. In the context of high-energy and nuclear physics, a long term motivation is to develop quantum computing methods that perform real-time evolution for lattice quantum chromodynamics (QCD). This is an ab-initio, ultraviolet complete, theory of strong interactions which has been very successful in describing the static properties of hadrons and nuclei [1]. Importance sampling methods, used successfully today for lattice QCD at Euclidean time, are not effective at dealing with the rapid oscillations of real-time unitary operators acting on large Hilbert spaces. Currently, physicists resort to non ab-initio algorithms such as Pythia and Herwig [13, 228] to interpret hadronic collider data. Doing ab-initio calculations for jet physics would represent a major accomplishment and is a long-term goal for the high-energy community. Strategies to deal with the related question of parton distributions are outlined in Refs. [158, 186]. Progress for out-of-equilibrium processes in many-electron systems and information paradoxes in quantum gravity [200] would also have a large potential impact.

As quantum computers offer new approaches to various sign problems, it is common to advocate following the sequence of models that has been successful for the development of lattice QCD at Euclidean time on classical computers [153, 154]. The first step in this sequence is to study the quantum Ising model (QIM) on current hardware. Real time evolution involving a limited number of sites for the QIM has already been attempted using a few qubits on gate based quantum computers [26, 51, 114, 115, 138, 147, 155, 157, 213, 229, 234, 246, 260, 263], as well as developments in progress for more complicated models [5, 17, 37, 39, 46, 127, 132, 143, 145, 150, 175, 207, 232, 241, 271]. For processes involving a few Trotter steps, error-mitigation methods such as zero-point extrapolation [206], written for a generic noise that can be intentionally increased in order to attempt an extrapolation to zero noise, have been applied successfully [141, 142, 150]. It has been shown [115] that by

[1] See review 17 of the PDG [109].

modelling four qubits on an IBM Q quantum computing hardware platform these mitigation methods together with using significantly larger Trotter steps [114, 179, 180] provide a reasonable extrapolation for times of the order of the approximate periodicity of the problems considered.

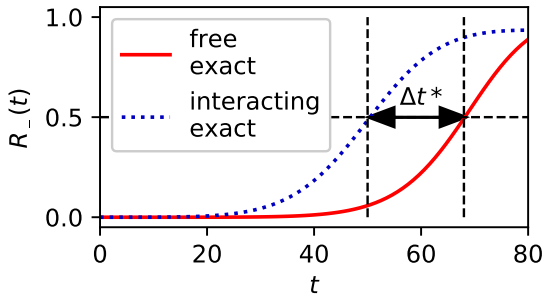

Figure 3.6: The normalized reflection probability $R_{-}(t)$ is defined in Eq. (3.15).

Phase shifts are a key measurement in the scattering process and represent the total change of phase due to interactions. Significant progress has been made in calculating them from lattice QCD in Euclidean time [34–36, 68, 173, 214]. In standard textbooks, phase shifts and scattering amplitudes are estimated from asymptotic data long after the collision processes have occurred. However, for current devices with limited coherence time or gate-depth, using the information from the early stages of the collision is advantageous. In order to optimize the use of limited resources, we will focus on the reduced problem of a particle coming from the left, rebounding on a wall and returning to the left. We show that it is possible to project the wave-function in the early stages of a collision process onto momentum states and to pinpoint a time $t^{\star}$ that corresponds to the middle of the collision with the wall. This time can be estimated by computing the time when the probability for the approximate momentum of the initial wavepacket and its opposite are equal. In practice, this can be done by introducing a normalized probability $R_{-}(t)$ for the reflection, defined later in Eq. (3.15) and which takes the value 0.5 at $t^{\star}$. By introducing an extra interaction close to the wall, we obtain a time delay $\Delta t^{\star}$ illustrated in Fig. 3.6. We will show that $\Delta t^{\star}$ is half of the time delay Δt_W invoked in Wigner formula [256], provided in Eq. (3.12), to estimate the

derivative of the phase shift with respect to the momentum. We implemented this idea on a trapped-ion quantum computer. We also collect data from superconducting qubits at IBM to show that the method can be applied to other quantum computer architecture.

The section is organized as follows. We introduce the quantum Ising model with an extra interaction and its Hilbert space. We show that in the one-particle quantum mechanic limit, a three-step method can be used to extract phase shifts from information about the early stage of the collision. However, this method is not scalable with system size as the Fourier transforms are costly. We then show that it is possible to extend the computations to the case of the quantum field theory formulations [114] , which require more qubits but are guaranteed to scale efficiently for larger volume.

3.2.1 Model

We consider the transverse-field Ising model in one spatial dimension,

$$\hat{H}_0 = -J \sum_{i=1}^{N-1} \hat{\sigma}_i^x \hat{\sigma}_{i+1}^x - h_T \sum_{i=1}^{N} \hat{\sigma}_i^z, \tag{3.7}$$

where N is the number of spatial sites. $\sigma_i^x(\sigma_i^z)$ is the Pauli X(Z) operator acting on site i. The on-site energy h_T is often called a transverse magnetic field and the ferromagnetic nearest-neighbor interaction J is responsible for particle hopping, creation and annihilation. This model is very well understood [154] and has been investigated on current quantum devices [51, 114, 115, 157]. It is equivalent to a theory of free fermions with subtle effects from the boundary.

For simplicity, we first consider the quantum mechanics limit $J \ll h_T$, where the particle number is conserved. This amounts to neglecting terms of the form $\hat{\sigma}_i^+ \hat{\sigma}_{i+1}^+$ and their conjugates. This reduces the size of the Hilbert space from 2^N to N, and allows us to perform Fourier transforms with a reduced number of qubits. Analytic calculations [114] are also possible in this approximation.

For problems invariant under translations and rotations, the standard quantum mechanics two-particle-scattering problem can be reduced to a radial Schroedinger equation in an effective potential. In one spatial dimension, the simplest case of effective potential for the reduced problem is a step adjacent to an infinite wall. To be concrete, we can think of a particle coming from minus infinity and moving towards a wall. As it approaches the wall, it reaches a potential step which is defined as positive and constant. The phase shift due to this type of potential is a standard textbook problem.

In the Ising model, non-trivial interactions capable of generating a phase shift can be introduced with an extra term

$$\hat{H}_{int} = U \sum_{i=1}^{N-1} \hat{\sigma}_i^z \hat{\sigma}_{i+1}^z. \tag{3.8}$$

For the reduced one-particle problem with a right wall, the interaction of Eq. (3.8) introduces an effective potential at the end of the chain. This can be seen in the one-particle basis. If the particle is away from the wall and has a neighbor on each site, it creates an energy -2U, but if it next to the wall, it only creates an energy -U which is +U above the energy when it is away.

This discrete Schrödinger equation obtained in the limit of small J, with $U = 0$, and no boundaries admits plane wave solutions $e^{\pm ikx}$ with energy

$$E(k) = 2J(1 - \cos(k)). \tag{3.9}$$

An additive constant has been adjusted in order to have zero energy at zero momentum. If we introduce a right wall and impose $\psi(N + 1) = 0$, we need a relative phase $-e^{i2k(N+1)}$ for the reflected wave e^{-ikx}. If, in addition, we also introduce a repulsive potential $U > 0$ at the rightmost site N, the problem with a right wall can be solved by introducing the phase shift. A short calculation shows that:

$$e^{i2\delta(k)} = e^{-i2k} \frac{U + Je^{ik}}{U + Je^{-ik}}, \tag{3.10}$$

Notice that this formula is independent of N, because so far there is no left wall. In practice, such left wall will be introduced to restrict the problem to N sites. By imposing $\psi(0) = 0$, we obtain a Luscher formula

$$\delta(k) = -k(N+1) \bmod \pi, \tag{3.11}$$

which introduces a restriction on the momenta. The restriction to a finite number of sites implies a N-dependence that we will discuss below.

The time delay Δt_W of a wave packet with a sharply defined momentum k is related to the derivative of the phase shift by the Wigner formula [256]:

$$\Delta t_W = 2\delta'(k)/(\partial E/\partial k), \tag{3.12}$$

where $\partial E/\partial k$ is the group velocity, which in our case is $2J\sin(k)$. This formula is obtained by considering the superposition of two plane waves with infinitesimally close momenta and energies and calculating the time difference for the two waves to be in phase at a given location with and without interaction. This comparison needs to be done at a time sufficiently longer than the time when the interaction takes place.

From Eq. (3.10) we get:

$$\Delta t_W = (-1 + J\frac{U\cos(k) + J}{U^2 + J^2 + 2JU\cos(k)})/J\sin(k). \tag{3.13}$$

The time delay Δt_W can *also* be estimated from the first half of the real-time evolution of the scattering process and that it is actually twice the time delay $\Delta t^\star$ already mentioned in Fig. 3.6. For this purpose, we define the probabilities to be in the $|\pm k\rangle$ state

$$P_\pm(t) \equiv |\langle \pm k|\psi(t)\rangle|^2, \tag{3.14}$$

and their normalized versions

$$R_{\pm}(t) \equiv \frac{P_{\pm}(t)}{P_{+}(t) + P_{-}(t)} \tag{3.15}$$

which by design satisfy

$$R_{+} + R_{-} = 1. \tag{3.16}$$

With this normalization $R_{+}(t)$ and $R_{-}(t)$ get interchanged under time-reversal with respect to $t^{\star}$. The real-time evolution provides the time $t^{\star}$ necessary to reach the symmetric situation where $P_{+}(t^{\star}) = P_{-}(t^{\star})$ and $R_{-}(t^{\star}) = 0.5$. This corresponds to the time where a classical particle would hit the wall. We can then compare $t^{\star}$ in the case where $U = 0$ and a non-zero value. We call these times $t^{\star}_{free}$ and $t^{\star}_{int.}$ respectively. We define the difference

$$\Delta t^{\star} \equiv t^{\star}_{int.} - t^{\star}_{free}, \tag{3.17}$$

and will argue that

$$\Delta t^{\star} = \frac{\Delta t_W}{2} \tag{3.18}$$

This relation can be justified from the time-reversal argument that after $t^{\star}_{int.}$ only *half* of the phase shift, $\delta(k)$, has built up while the other half builds after $t^{\star}$. This is actually why historically, the total phase shift is denoted $2\delta(k)$.

In order to confirm this statement, we made a numerical calculation with a number of sites $N = 128$. This number is larger than the number that we will use later ($N = 4$) and allows us to minimize the finite volume effects. The results are shown in Fig. 3.7 and support Eq. (3.17).

We now briefly explain how we calculated Δt^{*}. First, it is important to prepare a wave packet that is broad enough in space to have sharply defined momentum but not too broad so that it does not reflect too early. In the numerical calculations, we used an initial wavepacket which in lattice units reads

$$\psi(x) \propto e^{ikx - (x-N/2)^2/(N/4)^2}. \tag{3.19}$$

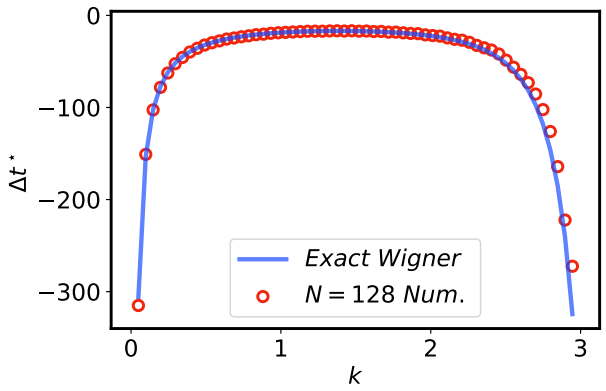

Figure 3.7: Comparison of numerical Δt^* with the analytical formula Eq. (3.13) for $N = 128$.

Second, we used a sigmoid parametrization for the normalized reflection probability

$$R_-(t) \simeq 1/(1 + \exp\left(-(\frac{t - t^\star}{w})\right)). \tag{3.20}$$

Empirically, this provides very good fits of the numerical data. The parameter w describes the width of the transition region in time units and $t^\star$ the time such that $R_-(t^\star) = 0.5$ exactly. The quality of the sigmoid fit is illustrated in Fig. 3.8. The fit was performed by calculating the continuous time evolution by exact diagonalization and doing a sigmoid fit with six points in time, as we will do in the next section. It is useful to notice that the time scale for the duration of the collision is roughly proportional to N. In order to get an

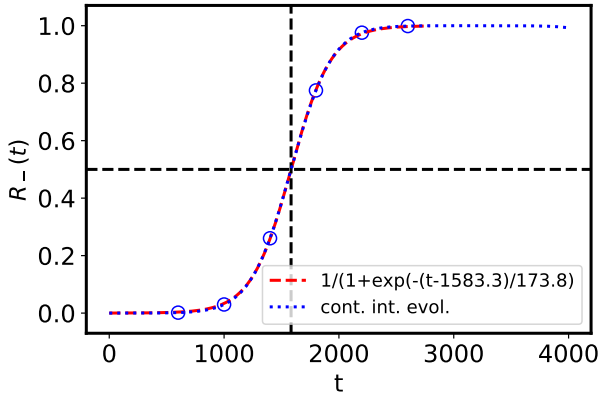

Figure 3.8: The fitted values are $t^\star = 1583.3$ and $w = 173.8$.

idea how the phase shifts change when we decrease N, we plotted $\delta(k)'$ for N= 32, 64 and

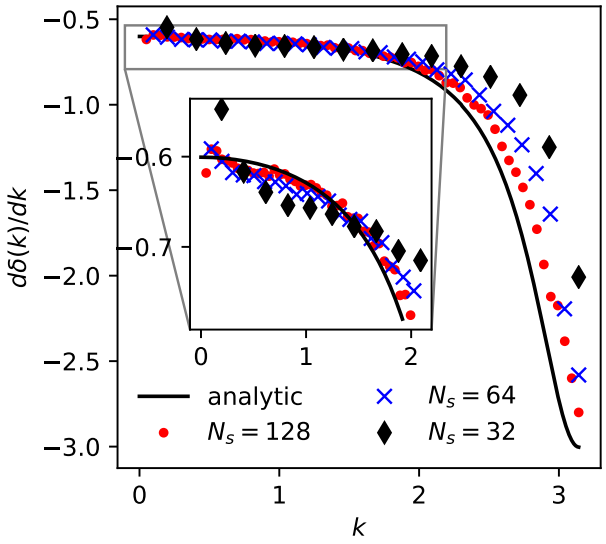

Figure 3.9: Derivative of the phase shift with respect to momentum calculated numerically using the time delays and Eq. (3.12) for N= 32, 64 and 128 compared to the infinite volume results from Eq. (3.13).

128 in Fig. 3.9. This illustrates the magnitude of the volume effects which are clearly more pronounced when k increases. Note that some integration procedure is needed in order to extract $\delta(k)$. From Eq. (3.10), we can expand $\delta(k)$ in power of k. For our numerical values $J = 0.02$ and $U = 0.03$, we obtain

$$\delta(k) \simeq -0.6k + 0.008k^3 + \ldots \tag{3.21}$$

For $0 \leq k \leq 0.5$ the correction to the linear approximation is less then one percent, justifying the approximation

$$\delta(k) \simeq \delta'(0)k. \tag{3.22}$$

This can be used to initialize the integration process to extract $\delta(k)$ from $\delta'(k)$ obtained from the time delay.

3.2.2 Quantum Mechanic Limit Simulation for N=4

Specializing to the case $N = 4$, we have, up to an unimportant additive constant, the following effective Hamiltonian matrix:

$$\hat{H}_{eff} = \begin{pmatrix} 0 & -J & 0 & 0 \\ -J & 0 & -J & 0 \\ 0 & -J & 0 & -J \\ 0 & 0 & -J & U \end{pmatrix}. \tag{3.23}$$

This allows us to reduce the Hilbert space from four qubits needed for the $N = 4$ field theory problem to two qubits for the one particle limit. The re-mapping is shown in Eq. (3.24) with the correspondence illustrated in Fig. 3.10:

$$\begin{aligned} |1000\rangle \to |00\rangle,\ |0100\rangle \to |01\rangle \\ |0010\rangle \to |10\rangle,\ |0001\rangle \to |11\rangle. \end{aligned} \tag{3.24}$$

The Hamiltonian in Eq. (3.23) can now be written as

$$\begin{aligned} \hat{H}_{eff} = &- J\sigma^x_{II} - \frac{J}{2}\Big(\sigma^x_I\sigma^x_{II} + \sigma^y_I\sigma^y_{II}\Big) \\ &+ \frac{U}{4}(1 - \hat{\sigma}^z_I)(1 - \hat{\sigma}^z_{II}). \end{aligned} \tag{3.25}$$

The subscripted roman numerals are used to indicate the use of our two-qubit decomposition.

We now report quantum computations for $J = 0.02$ and $U = 0.03$. In the 2-qubit Hilbert space, the momentum states for $k = \pm\pi/2$ read

$$|k = \pm\pi/2\rangle = \frac{1}{2}(|00\rangle \pm i|01\rangle - |10\rangle \mp i|11\rangle). \tag{3.26}$$

It is necessary for the initial wave packet to have some localization in space so that a distinct scattering event is visible, i.e., there is a point in time when the particle reaches the

interaction region. As a side effect, the wave packet will have some momentum distribution because it no longer is a plane wave. As depicted in Fig. 3.10, we chose our initial wave packet to be $|\pi/2\rangle$ but restrict it to be non-zero only in the middle:

$$|\psi\rangle = \frac{1}{\sqrt{2}}\Big(|01\rangle + i|10\rangle\Big). \tag{3.27}$$

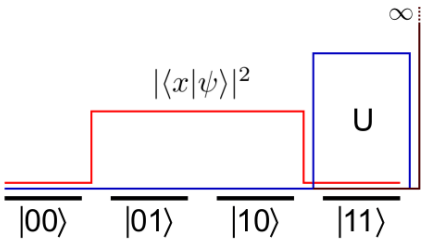

Figure 3.10: Visual depiction of the qubit states (black dashes), potential for the interacting (blue) and non-interacting case (dark red), and initial wave packet (light red).

We construct this wave packet on two sites with the following quantum circuit with all qubits initialized in the $|0\rangle$ state:

$$U_{\text{state prep}} = \quad \text{—}\boxed{X}\text{—}\boxed{XX\Big(-\tfrac{3\pi}{2}\Big)}\text{—} \quad . \tag{3.28}$$

The time evolution operator can be written as a combination of XX, YY, X, rotations and a controlled phase operation (R_ϕ):

$$U_{\text{Tr}}(\rho,\theta) = \quad \text{—}\boxed{R_x(2\rho)}\text{—}\boxed{XX(\rho)}\boxed{YY(\rho)}\text{—}\boxed{R_\phi(\theta)}\text{,} \tag{3.29}$$

where $\rho = J\delta t$, $\theta = U\delta t$, and $\delta t = 12.5$. We use standard notations [191] for the gates,

$$\begin{aligned} XX(\rho) =& e^{-i\rho XX/2},\ YY(\rho) = e^{-i\rho YY/2}, \\ &\text{and } R_X(\rho) = e^{-i\rho X/2}. \end{aligned} \tag{3.30}$$

The very slow growth of the one-step error for large δt [179, 180] allows us to reach $t = 75$ with only six Trotter steps [115].

We then perform a quantum Fourier transform (QFTr) on these two qubits to take this state into momentum space:

$U_{QFTr} =$ 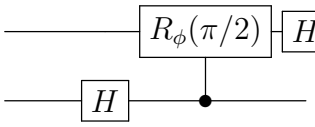

. (3.31)

After applying the QFTr, the qubit states $|10\rangle$ and $|11\rangle$ correspond to the momentum states $|k\rangle$ and $|-k\rangle$ respectively, with $k = \pi/2$.

The time $t^\star$ is determined by the symmetric condition $R_-(t^\star) = R_+(t^\star) = 0.5$. Because of the small volume, we used a *deformed* sigmoid parametrization

$$R_-(t) \simeq A/(1 + \exp\left(-(\frac{t - \tilde{t}^\star}{w})\right)) \tag{3.32}$$

provides very good fits of the numerical data. The parameter w describes the width of the transition region and $\tilde{t}^\star$ is related to $t^\star$ via,

$$t^\star = \tilde{t}^\star - w\ \ln(2A - 1) \tag{3.33}$$

The parameters w and $\tilde{t}^*$ are floated during the fit. For the interacting case, there is a damping due to finite volume and coherence loss and we set A equal to the last data point, which is then excluded from the fit. For the free case, the damping occurs at later time and we set $A = 1$ and fit the standard sigmoid with the six data points.

Type	Continuous	Trotter-exact	Trapped ions	IBM
Q.M.	-17.5(1)	-13.7(9)	-26(2)	-21(2)
Q.F.T.	-17(1)	-14.3(9)	-14(2)	-15(2)

Table 3.4: Results for Δt^* in the quantum mechanics limit (Q.M) and full field theory (Q.F.T.) from sigmoid fits of the simulated continuous and Trotter-exact evolutions as well as the experimental data from the trapped ions and IBM quantum computers.

The data for R_- obtained from both quantum computers are shown in Fig. 3.11a together with the sigmoid fits where the values of $t^\star_{free}$ and $t^\star_{int.}$ are indicated by vertical lines crossing the fits at the 0.5 horizontal line. This provides the numerical values of $\Delta t^\star$ given in Table 3.4. The Trotter-exact and continuous-time estimates have assumed errors on par with the statistical errors from the quantum simulations,

$$\delta R_-(t) = \sqrt{R_-(t) - (R_-(t))^2}/\sqrt{N_{shots}}, \tag{3.34}$$

with $N_{shots} = 1000$. For comparison, we give the values obtained by doing sigmoid fits of the continuous-time evolution (first column) and the Trotter steps (second column) calculated numerically at the same discrete times as the experimental data. Standard State Preparation and Measurement (SPAM) correction applied to the trapped-ion data, and no additional error mitigation is applied. Readout error corrections were applied to both sets of IBM data. In addition, the IBMQ Bogota data used Richardson extrapolations which take into account further systematic errors from the environment which produce larger uncertainties. Details of the fits are given in Appendix B in Ref. [116]. We see that both the IBM and trapped ion estimates provide larger absolute values of Δt^* than the target values. This can be in part explained by the fact that the fits for the free process tend to lag below the Trotter steps for $t > 50$ indicating a loss of coherence.

Measurements from the IBMQ Bogota machine contain both the noisy data with just readout corrections and a mitigated version obtained using methods discussed in Ref. [115] and which account for some slightly negative occupations at low t. This noise mitigation involves increasing the effective error rate in the circuit by applying iterated CNOT's to

increase the decoherence noise and then using a linear fit to data at different noise rates to extrapolate to a noiseless limit.

We see that the quantum mechanics approximation allows us to perform the QFTr and extract reasonable estimates of Δt^* (Table 3.4) for $N = 4$. However, the extension of this procedure for $N > 4$ requires all-to-all connectivity and a CNOT depth increasing with the number of sites. In contrast, the field theory calculation, which is our ultimate goal, requires more qubits but only local interactions[169] with a constant CNOT depth.

3.2.3 Towards scalable field theory calculations

We have performed field theory computations with the same devices using four sites and four qubits. This allows for shallower local circuits but requires a more expensive Fourier transform [86]. The initial state that we prepared,

$$|\psi_i\rangle = \frac{1}{\sqrt{2}}\Big(|01\rangle + i|10\rangle\Big), \tag{3.35}$$

can be remapped to the Ising model by using the inverse mapping originally described in the text:

$$\begin{aligned} &|00\rangle \to |1000\rangle,\ |01\rangle \to |0100\rangle \\ &|10\rangle \to |0010\rangle,\ |11\rangle \to |0001\rangle. \end{aligned} \tag{3.36}$$

This remapping will give us the initial state:

$$|\psi_i\rangle = \frac{1}{\sqrt{2}}\Big(|0100\rangle + i|0010\rangle\Big). \tag{3.37}$$

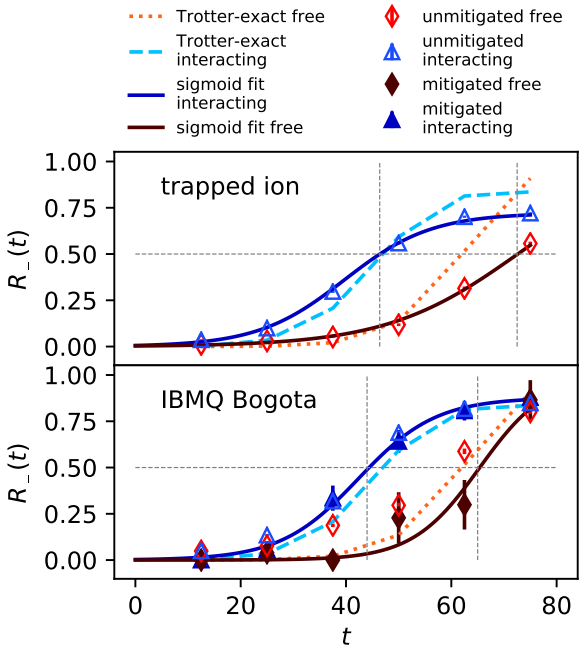

(a) Quantum mechanics limit for $R_{-}(t)$. Systematic errors shown for IBM mitigated results.

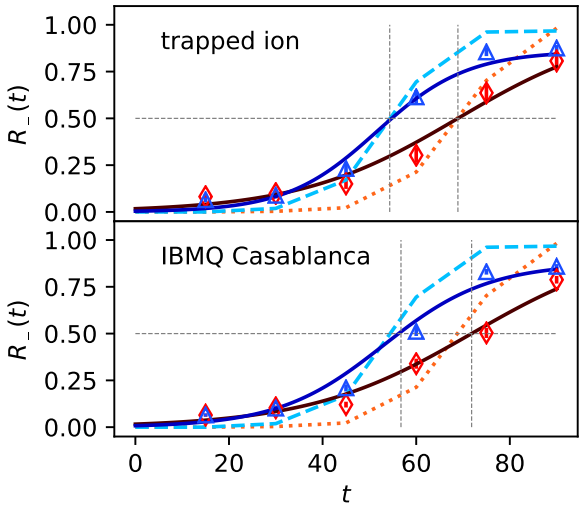

(b) Experimental results for $R_{-}(t)$ using the full Hamiltonian of Eq. (3.7).

Figure 3.11: Experimental results for $R_{-}(t)$ using the quantum mechanics limit (a) and the full Hamiltonian of Eq. (3.7) (b) with and without the interaction term on four qubits for trapped ion (top in figure), IBM (bottom in figure) quantum computers. The Hamiltonians use the parameters $J = 0.02$, $h_T = 1.0$, and $U = 0.03$. Statistical Errors are shown for all except for mitigated results.

This state can easily be prepared with 1 XX gate and one single qubit rotation,

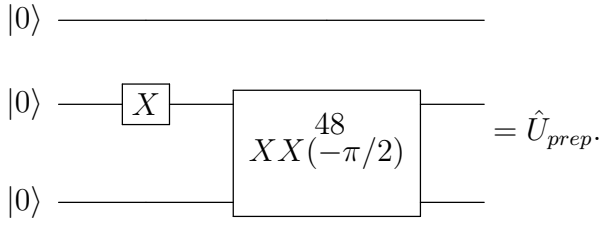

$$= \hat{U}_{prep}. \tag{3.38}$$

The time evolution of the system can be easily written in terms of a circuit requiring at most 3 XX gates per Trotter step when using a four site system, which is 2 XX gates deep, see Eq. (3.39).

$$\hat{U}_{Trot}(\delta t; J, U, h_T) =$$

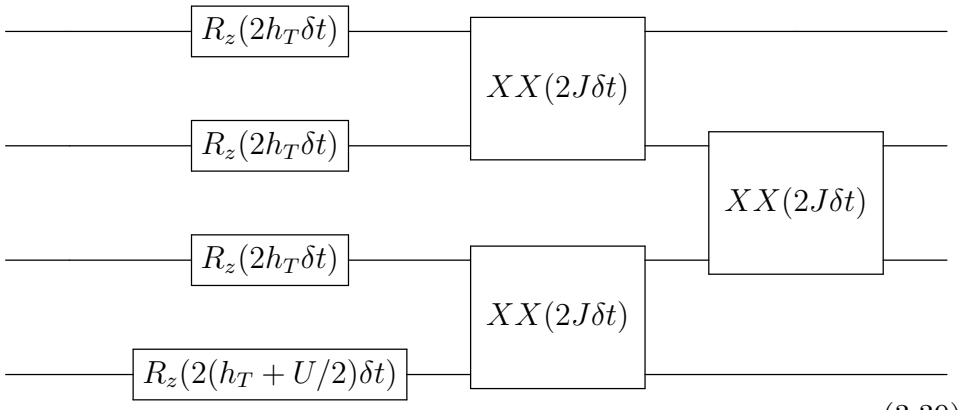

(3.39)

The final portion of the quantum simulation is a Fourier transformation to take the circuit into momentum space [86, 149]. This transformation can easily be done using four two-qubit operations.

$$\hat{U}_{fft} =$$

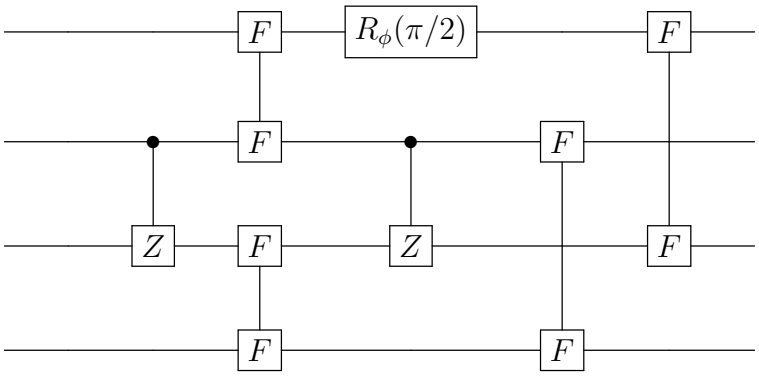

(3.40)

Where F is given by the matrix:

$$F = \begin{pmatrix} 1 & 0 & 0 & 0 \\ 0 & \frac{1}{\sqrt{2}} & \frac{1}{\sqrt{2}} & 0 \\ 0 & \frac{1}{\sqrt{2}} & -\frac{1}{\sqrt{2}} & 0 \\ 0 & 0 & 0 & -1 \end{pmatrix}. \tag{3.41}$$

This can be decomposed into at most 4 CNOT gates. It should be noted this is different from the traditional quantum Fourier transform which uses binary encoding for the qubits. The decompositions for the the F-gate, is shown in Appendix C.1.

The measurement is done then in the z-basis and we select out the states $|0010\rangle$ and $|0001\rangle$ for the $|k\rangle$ and $|-k\rangle$ state respectively.

In Fig. 3.11b we show the results of these calculations on our TIQC and IBM's Casablanca machine using the full Hamiltonian with a Trotter step of $\delta t = 15$ with six Trotter steps. In both cases, unmitigated data is used for the analysis. Fig. 3.11b indicates that the discrepancies between the individual fits and the Trotter exact results are more pronounced than in the previous calculation. However the effects appear to somehow compensate when we calculate the differences and we obtain time delays closer to the Trotter exact ones as shown in Table 3.4. This question could be investigated with more accurate data. As discussed in the SM, the fit methods are similar to the previous ones. No Richardson extrapolations are performed in this simulation because the effective noise rate on the circuit would be well outside the linear regime for the error. The non-linear errors would render a Richardson extrapolation infeasible. As improved quantum computing hardware platforms become available, more accurate estimation for $\Delta t^\star$ may become possible.

When extending the method to larger systems, the circuit cost of the of the Fourier transform is expected to be the most expensive but still scales as $\mathcal{O}(n\log(n))$ [86].

3.2.4 Conclusion and Outlook

We have proposed and implemented a method to estimate the time delay using the early steps of the real-time evolution. We have extracted phase shift from experimental results for a quantum mechanics limit model with two qubits and the field theory formulation with four qubits. We expect that the field theory calculations to scale favorably with system size and to be feasible on a larger number of qubits. In the future, quantum computations for quantum Ising models in two spatial dimensions could offer the possibility to reach quantum

advantage.

3.3 Quantum Advantage in the Bell-Type Non-Local Quantum Game with Cluster States

There are many metrics to characterize the quality of current quantum devices [202]. For example, qubit count, gate count, gate fidelities, and quantum volume [64] are common options. However, it is generally agreed upon that a more comprehensive picture is given by the device's overall performance in executing a variety of computational tasks. To this end, we look toward computational tasks with two desirable properties in this work. First, they should have objective targets, beyond which one can prove that the current devices has outperformed its classical counterpart. Note that the significance of demonstrating so-called quantum supremacy via sampling random quantum circuits [9, 259] or bosonic linear interferometers [265] relies on assumptions of the underlying problem's computational hardness, making it a moving target based on current state-of-the-art classical hardware and algorithms. In contrast, we seek an unconditional demonstration of quantum computational advantage. Second, the computational task should be agnostic to the choice of hardware implementation, so that it allows a fair comparison of results among different architectures.

Natural examples with the first desideratum are Bell-type nonlocal games [22, 41, 60], since the violation of a Bell inequality sets an objective threshold the quantum computer must pass. Experimental demonstrations of Bell inequality violations have a long history (see Ref. [41, Sec. VII]). More recently, the nonlocal features of quantum mechanics implied by such a violation have been experimentally confirmed [96, 123, 209, 222]. Nonlocal games have also been of recent interest for demonstrating classically verifiable quantum advantage in interactive proof systems [30, 31, 139]. The second desideratum is satisfied in cases where the violation is achievable via the preparation and measurement of multipartite entangled states with geometrically restricted, constant-depth formation circuits. A canonical example of such states are graph states [38, 120], which have a long history of study with respect to Bell-nonlocality [113, 216], measurement-based quantum computation [204], and connec-

tions therein [7, 125, 247]. Experimentally, nonlocal features of graph states have also been explored on a variety of hardware platforms [50, 160, 171, 249]. It has also been shown that Bell-type scenarios utilizing Pauli measurements on graph states go beyond the traditional Bell's theorem [18], as they are able to reject even classical theories assisted by a limited amount of communication, which are a particular class of nonlocal hidden-variable models. Much work has since gone into understanding how Bell's theorem can be strengthened to more general causal scenarios [52, 53, 92]. By treating these communication-assisted classical strategies as classical circuits of limited depth, one can show that shallow-depth quantum circuits are more powerful than their classical counterparts [33]. In light of these considerations, the past few years have seen a number of novel works laying the theoretical foundation for unconditionally demonstrating a quantum advantage using only nearest-neighbor entangling gates [32, 61, 94, 106, 107, 118, 254]. This excludes the use of n-qubit Greenberger–Horne–Zeilinger (GHZ) states, which can be prepared in constant depth with an architecture that allows all-to-all connectivity of its entangling gates, but requires linear depth for architectures with only nearest-neighbor connectivity.

In this section, we analyze two kinds of Bell-type nonlocal games and demonstrate proof-of-principle experimental implementations of them on a trapped-ion quantum computer. Both games utilize the six-qubit cyclic cluster state (an example of a graph state) and are motivated as follows. The first game can be viewed as the computation of a particular nonlinear Boolean function via the measurement of the six-qubit cyclic cluster state's stabilizer group, giving a new computational interpretation to the graph-state Bell inequalities introduced in Ref. [113]. Furthermore, it doubles as a method to determine the fidelity of the prepared state and is classically the hardest such game based on any six-qubit graph state.

The second game is based on the smallest instance of the so-called 2D hidden linear function problem introduced in Ref. [33], which is capable of demonstrating an unconditional separation between the power of a constant-depth quantum circuit and logarithmic-depth classical circuits. While prior works [32, 61, 94, 106, 107, 118, 254] focus on such quan-

tum computational advantage in an asymptotic regime, we discuss in detail how quantum-advantageous strategies for this six-qubit game already demonstrate an unconditional separation from shallow-depth classical circuits with the same gate connectivity used on our quantum computer. Furthermore, we show that restricting the set of inputs for this game makes it harder classically, reducing the target success probability required to demonstrate quantum advantage from 87.5% to 80%.

These nonlocal games satisfy our desired criteria, as the corresponding quantum strategies require only nearest-neighbor entangling gates on a ring, which are readily available on most quantum-computing architectures. Furthermore the games scale well, leading to meaningful results for surpassing the same target success probability as the qubit count increases. For our six-qubit demonstration, we summarize the games implemented and our experimental results in Table 3.5.

The section is organized as follows. In Sec. 3.3.1 we review background material necessary to understand our key results and establish notation. In Sec. 3.3.2 we introduce the first type of nonlocal game, called cubic Boolean function games, and show the experimental implementation of the quantum strategy of the game. In Sec. 3.3.3 we discuss the second type of nonlocal game, called stabilizer submeasurement games and its experimental results. Finally, we conclude with a discussion and outlook in Sec. 3.3.4.

3.3.1 Background

Graph states

Stabilizers, stabilizer states, and graph states are essential concepts for understanding quantum games discussed in this work. Stabilizer states are a particular class of many-body quantum states that have a wide range of applications in quantum computing (e.g., for error correction, measurement-based quantum computing, and tests of Bell nonlocality). An n-qubit stabilizer state is defined as the joint $+1$ eigenstate of 2^n commuting Pauli operators, called the stabilizer group. Each element of this stabilizer group is a stabilizer of the n-qubit

Table 3.5: Summary of the nonlocal games studied in this work, along with our main experimental results using a trapped-ion quantum computer. The notation and definition of the games are provided in their respective sections. For the optimal quantum strategy, each game involves preparing the six-qubit cyclic cluster state $|C_6\rangle$ and then evaluating a number of stabilizers from global Pauli measurement settings, which may not necessarily be the same. As the success probability $\Pr_C[\text{win}]$ of a classical strategy may depend on the amount of communication allowed between parties, we report bounds for both depth-0 and depth-1 classical circuits. The cubic Boolean function (CBF) results were obtained by a tomography experiment measuring the relevant stabilizers (data presented in Fig. 3.13). The stabilizer submeasurement (SS) results were obtained by a separate experiment wherein we faithfully played the nonlocal games (data presented in Table 3.6). We report experimental success probabilities $\widehat{\Pr}_Q[\text{win}]$ estimated from both the raw output of our quantum device, and after SPAM correction. The experimental uncertainties, denoted by the values in parentheses, correspond to a 1σ standard error within the number of significant figures reported. For each input of a game, we took $N = 5000$ shots.

Game	Number of (stabilizers, settings)	$\Pr_C[\text{win}]$		Experimental $\widehat{\Pr}_Q[\text{win}]$	
		Depth-0 bound	Depth-1 bound	Raw value	SPAM-corrected
$\text{CBF}(C_6, \{0,1\}^6)$	$(63, 63)$	$23/32 = 71.875\%$	100%	80.30(8)%	83.21(9)%
$\text{CBF}(C_6, \mathcal{I}^{(55)}_{\text{Mermin}})$	$(55, 55)$	$37/55 \approx 67.3\%$	100%	79.51(9)%	82.56(10)%
$\text{SS}(C_6, \mathcal{I}^{(8)}_{\text{HLF}})$	$(5, 8)$	$7/8 = 87.5\%$	87.5%	81.35(59)%	85.79(53)%
$\text{SS}(C_6, \mathcal{I}^{(5)}_{\text{HLF}})$	$(5, 5)$	$4/5 = 80\%$	80%	79.42(25)%	84.68(23)%

stabilizer state. Let X, Y, and Z be the Pauli matrices. I denotes the 2×2 identity matrix and $\mathbb{1}$ the identity operator acting on the whole system. Let $|0\rangle$ and $|1\rangle$ be the $+1$ and -1 eigenstates of Z, respectively. Denote by X_j an n-qubit Pauli operator that acts as X on the jth qubit and as the identity elsewhere (similarly for Y_j and Z_j). Any n-qubit Pauli operator can be written (up to an overall phase) as $E(\mathbf{a}, \mathbf{b}) = \prod_{j=0}^{n-1} i^{a_j b_j} X_j^{a_j} Z_j^{b_j}$, where $\mathbf{a}, \mathbf{b} \in \{0,1\}^n$. Denote the jth term in the product for $E(\mathbf{a}, \mathbf{b})$ by $E_j(a_j, b_j)$.

It is convenient to study stabilizer states in the so-called graph-state formalism [120]. As its name suggests, graph states can be defined with respect to graphs. For each graph $G = (V, E)$, with vertex set V and edge set E, the corresponding graph state $|G\rangle$ is prepared by initializing a qubit at each vertex $v \in V$ in the state $|+\rangle = (|0\rangle + |1\rangle)/\sqrt{2}$ and applying a two-qubit controlled-Z gate, $CZ_{v,w}$, between each pair of vertices v and w connected by an

edge $(v, w) \in E$. The graph state can be expressed as

$$|G\rangle = \prod_{(j,k)\in E} \mathrm{C}Z_{j,k} \, |+\rangle^{\otimes |V|} \, . \tag{3.42}$$

Any stabilizer state is equivalent to a graph state up to single-qubit Clifford gates (the set of gates generated by $H = (X + Z)/\sqrt{2}$ and $S = \sqrt{Z}$) [101, 218, 242]. Conversely, any graph state is uniquely defined by its stabilizer group. From Eq. (3.42) it follows that $|G\rangle$ is the $+1$ eigenstate of all the elements of

$$\mathcal{S}_G = \left\langle X_v \prod_{l\in\mathcal{N}(v)} Z_l \;\middle|\; \forall v \in V \right\rangle , \tag{3.43}$$

where $l \in \mathcal{N}(v)$ if and only if $(l, v) \in E$. The notation $\langle \cdot \rangle$ indicates the set of all possible products generated by the operators contained in the brackets. The operators in the brackets are referred to as stabilizer generators. The generator $S_v = X_v \prod_{l\in\mathcal{N}(v)} Z_l$ can be associated with the vertex v.

In this work, we focus on the six-qubit graph state on the cycle graph $|C_6\rangle$, also known as the six-qubit cyclic cluster state, where C_6 denotes the six-vertex cycle graph. Following Eq. (3.42), the preparation of $|C_6\rangle$ followed by a measurement of an arbitrary Pauli operator $E(\mathbf{a}, \mathbf{b})$, is shown in Fig. 3.12.

It turns out that the fidelity of the experimentally prepared graph state can be estimated by measuring its stabilizer. $|G\rangle$ is the ideal target graph state and ρ is the density matrix of the experimentally prepared (possibly mixed) graph state. Following standard fidelity metric, the fidelity of the ρ can be expressed as

$$\mathcal{F}(\rho, |G\rangle) = \langle G| \, \rho \, |G\rangle = \mathrm{tr}(|G\rangle\langle G| \, \rho). \tag{3.44}$$

The projector $|G\rangle\langle G|$ can be expressed in terms of the 2^n elements of the stabilizer group $\mathcal{S}_G$

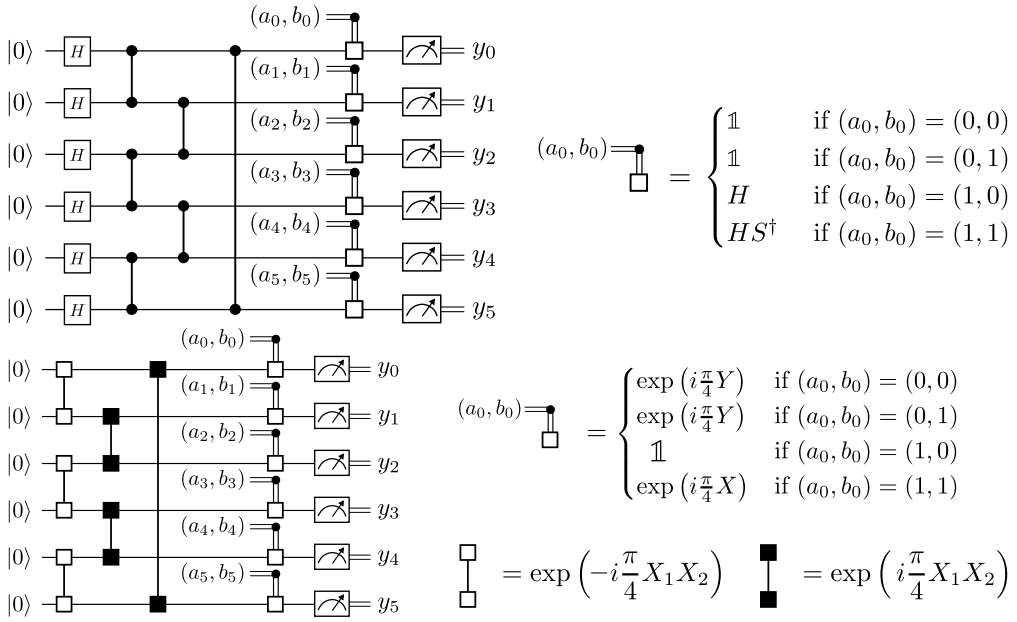

Figure 3.12: (Top): The quantum circuit that prepares the six-qubit cyclic cluster state $|C_6\rangle$ using CZ gates, followed by the measurement of the Pauli operator $E(\mathbf{a}, \mathbf{b})$ for some $\mathbf{a}, \mathbf{b} \in \{0,1\}^6$. Namely, the final conditional rotation changes the measurement basis of the jth qubit to Z, X, or Y whenever the classical input $(a_j, b_j) \in \{0,1\}^2$ is $(0,1)$, $(1,0)$, or $(1,1)$, respectively. Input $(0,0)$ denotes the presence of an identity in the Pauli operator, in which case the qubit is measured in the Z basis. (Bottom): The same circuit, recompiled using $R_{XX}(\theta)$ gates which are native to our trapped-ion device, and optimized to reduce the number of single-qubit gates.

of $|G\rangle$,

$$|G\rangle\langle G| = \frac{1}{2^n} \sum_{S \in \mathcal{S}_G} S. \tag{3.45}$$

Combining the above two equations we see that the fidelity of ρ can be rewritten as the sum of the expectation value of ρ with respect to each stabilizer S.

$$\mathcal{F}(\rho, |G\rangle) = \frac{1}{2^n} \sum_{S \in \mathcal{S}_G} \mathrm{tr}(\rho S). \tag{3.46}$$

Bell-Type Non-Local Games

Nonlocal game is a computational setup that usually involves multiple players and multiple rounds. In each round, every player i receives a piece of informtaion about a global input bit string $\mathbf{x}$. Players process the partial input information they each received separately

according to strategy and each produces an one-bit output y_i. All y_i make up the collective output string $\mathbf{y}$. The referee then checks that the output possesses the desired properties and accordingly tallies the round as a win or loss.

The strategy of the game describes how each player manipulates information received to generate the output y_i. Supposed each player receives l bit of information about $\mathbf{x}$. In a quantum strategy, each player holds a qubit from a multipartite entangled state and measures the qubit in some basis depending on the input information received. Further explicit communication between players is not allowed in the quantum strategy. In a classical strategy, each player may communicate with neighboring parties to obtain a total of $k \leq K$ bits of information about the input. Each player i then manipulates their information via some Boolean function $f : \{0,1\}^k \to \{0,1\}$ and repeats this process for a total of D rounds of communication; in the last round, each output is produced via some $y_i : \{0,1\}^k \to \{0,1\}$. Each classical strategy can therefore be associated to a particular depth-D classical circuit, consisting of gates depending on no more than K outputs of its neighboring gates in the previous layer. Conceptually, it is easy to see that more rounds of communication will improve the win rate of a strategy since the players learn about what each other is doing through communication. If no communication is allowed ($D = 0$), the corresponding classical strategy is called a Depth-0 strategy. If D rounds of communication are allowed, the corresponding classical strategy is a depth-D strategy.

The average success probability for each strategy is defined as Pr[win], which is the average probability of winning the game given an input x chosen uniformly at random. Pr[win] can be written as

$$\Pr[\text{win}] = \frac{1}{|\text{Input}|} \sum_{\mathbf{x} \in \text{Input}} \sum_{\mathbf{y} \in \text{Win}(\mathbf{x})} \Pr[\mathbf{y}|\mathbf{x}]. \tag{3.47}$$

$\Pr[\mathbf{y}|\mathbf{x}]$ is the conditional probability of generating output y given input x, and $\text{Win}(\mathbf{x})$ is the set of all winning output y for a given input $\mathbf{x}$.

Strategies with Pr[win] = 1 are said to be perfect. For each nonlocal game we study, there exists a perfect quantum strategy. On the other hand, classical strategies for these games will produce a hierarchy of bounds depending on the classical circuits considered. For brevity, we express these bounds as

$$\Pr_C[\text{win}] \leq_{\text{Depth-0}} \beta_0 \leq_{\text{Depth-1}} \beta_1 \leq_{\text{Depth-2}} \beta_2, \tag{3.48}$$

where "Depth-0" denotes that β_0 is the maximum value of $\Pr_C[\text{win}]$ for any circuit with $D = 1$, $K = l$, and each output depends only on the l bits received by a party. Furthermore, "Depth-1" and "Depth-2" denote that β_1 and β_2 are the maximal values for any geometrically restricted classical circuit with $D = 1, 2$, respectively, and $K = 3l$. The definition of the bounds will become clearer in the next two sections where two examples of quantum games are discussed. Surpassing any of these bounds with a quantum device is interpreted as a violation of a Bell-type inequality, which in turn demonstrates a quantum computational advantage.

3.3.2 C_6 Cubic Boolean Function Games

Here we present the cubic Boolean function game on C_6 (CBF$(C_6, \mathcal{I})$), which is adapted from the graph state Bell inequalities presented in Ref. [22]. This game can be generalized to a n-player scenario. The six-player version is chosen here for experimental demonstration. In CBF$(C_6, \mathcal{I})$, each player is represented by a vertex in the C_6 state. Each player receives a two-bit input of classical information $s_j = (a_j, b_j) \in \{0, 1\}^2$, $j = 0, \ldots, 5$, where j indexes the player. The inputs s_j are drawn as follows: from a global input $\mathbf{x} = (x_0, \ldots, x_5) \in \mathcal{I} \subseteq \{0, 1\}^6$, each party j is given the bit $a_j = x_j$ and the parity of their neighbors' bits, $b_j = x_{j+1} + x_{j-1} \bmod 2$. Each party j then produces a one-bit output y_j. If the output satisfies condition specified in Eq. 3.49 , the players win the game.

$$\sum_{j\in\mathrm{supp}(\mathbf{s})} y_j = \sum_{j=0}^{5} x_{j-1}x_j x_{j+1} \bmod 2, \tag{3.49}$$

where $\mathrm{supp}(\mathbf{s}) = \{0 \le j \le 5 \mid s_j \neq (0,0)\}$ and all subscripts are taken mod 6. Pr[win] of a certain strategy is probability of winning the game averaging over all 2^6 possible inputs.

There exist a perfect quantum strategy for this game. Each player holds one qubit from the C_6 state and measure the Pauli operator $E_j(a_j, b_j) = i^{a_j b_j} X_j^{a_j} Z_j^{b_j}$ on their qubit given the input s_j. This strategy is perfect with a 1 win rate because, collectively, the parties measure the Pauli part of the stabilizer $S_{\mathbf{x}} = \prod_{j=0}^{5} S_j^{x_j}$, where S_j denotes the stabilizer generator corresponding to vertex j of C_6. The parity of the measurement outcomes for qubits $j \in \mathrm{supp}(\mathbf{s})$ is then deterministically equal to the phase in front of $S_{\mathbf{x}}$, which is $\exp\left(i\pi \sum_{j=0}^{5} x_{j-1}x_j x_{j+1}\right)$. The detailed proof is presented in Ref. [66] Appendix C. Although, theoretically, the quantum strategy has Pr[win] = 1, the Pr[win] of the experimentally implemented quantum strategy is affected by experimental errors in initial state preparation and measurement. Since the measurement done on the C_6 state corresponding to each $\mathbf{x}$ is equivalent to measuring one element in the stabilizer group of C_6. Based on Eq. (3.54), the measurement outcome of the game can be used to construct the fidelity of the graph state, or we can say that playing the entire game can be seen as a state (partial) state tomography for C_6. The experimentally achieved Pr[win] of the quantum strategy is related to the fidelity of C_6 through the following expression

$$\mathcal{F}(\rho, |C_6\rangle) = 2\,\mathrm{Pr}_Q[\mathrm{win}] - 1. \tag{3.50}$$

On the other hand, classical strategies perform with varying success depending on the particular input set $\mathcal{I}$. We now consider two particular input sets, the full input set and a restricted input set, that give to different classical bounds on the depth-0 success probability.

Full-input cubic Boolean function game (fidelity game)

Setting the input set $\mathcal{I}$ to be all possible six-bit binary strings. The depth-0 classical circuits cannot win this game with a probability greater than $\Pr_C[\text{win}] \leq 23/32$. This is proved in Ref. [113] from the upper bound of the local hidden-variable theory for the corresponding graph-state Bell inequality. However, depth-1 circuits can implement perfect strategies. This is achieved by each party individually computing one cubic term in the function of Eq. (3.49) as $y_j = a_{j-1}a_j(b_j + a_{j-1}) = x_{j-1}x_jx_{j+1} \bmod 2$, which satisfies the win conditions of the game. Hence,

$$\Pr_C[\text{win}] \leq_{\text{Depth-0}} \frac{23}{32} \leq_{\text{Depth-1}} 1 \leq_{\text{Depth-2}} 1. \tag{3.51}$$

Restricted-input cubic Boolean function game

This input set yields the game $\text{CBF}(C_6, \mathcal{I}^{(55)}_{\text{Mermin}})$. Following the seminal work of Mermin [178], in Ref. [47] it was shown that by restricting to a 55-element subset $\mathcal{I}^{(55)}_{\text{Mermin}}$ of $\{0,1\}^6$ gives the smallest depth-0 classical success probability for the state $|C_6\rangle$.

$$\mathcal{I}^{(55)}_{\text{Mermin}} = \left\{ \mathbf{x} \in \{0,1\}^6 \;\middle|\; \begin{array}{l} |\mathbf{x}| \neq 0, 1, \\ \mathbf{x} \neq 010101, 101010 \end{array} \right\}, \tag{3.52}$$

where $|\mathbf{x}| = \sum_{j=0}^{5} x_j$ denotes the Hamming weight of $\mathbf{x}$ (i.e., the number of ones in the binary string).

The same quantum strategy presented for $\text{CBF}(C_6, \{0,1\}^6)$ is also perfect for this game. For the classical bounds, depth-0 classical circuits cannot win with probability greater than 37/55, although the same depth-1 circuit presented in the full input game remains perfect. Hence,

$$\Pr_C[\text{win}] \leq_{\text{Depth-0}} \frac{37}{55} \leq_{\text{Depth-1}} 1 \leq_{\text{Depth-2}} 1. \tag{3.53}$$

Experimental Results for $\mathrm{CBF}(C_6, \{0,1\}^6)$ **and** $\mathrm{CBF}(C_6, \mathcal{I}^{(55)}_{\mathrm{Mermin}})$

As discussed earlier, the win rate of the CBF games can be estimated from the fidelity of the $|C_6\rangle$ state. We experimentally prepared the $|C_6\rangle$ state and directly estimated its fidelity by measuring its 63 non-trivial stabilizers (excluding II). The circuit for preparing the $|C_6\rangle$ and performing the stabilizer measurements are shown in Fig. 3.12. Indeed, this would be essentially equivalent to known probabilistic protocols for estimating state fidelities, which in this context use uniformly randomized measurement settings over all stabilizers [89, 227]. In order to obtain an estimate of the fidelity within precision $\pm\epsilon$, with success probability $\geq 1-\delta$, such methods require up to $\lceil 8\ln(4/\delta)/\epsilon^2 \rceil$ measurements. This is notably independent of system size, despite the fact that the total number of stabilizers grows exponentially with n. However, since our six-qubit system is fairly small, this randomization turns out to incur a larger constant overhead compared to a more direct approach.

We further group the 63 stabilizers into 37 locally commuting sets, where within each set the expectation value of all stabilizers can be estimated from the results of one measurement setting. Two Pauli operators $\otimes_{j=0}^{n-1} P_j$ and $\otimes_{j=0}^{n-1} Q_j \in \{X, Y, Z, I\}^{\otimes n}$ are said to locally commute if $[P_j, Q_j] = 0$ for all j. For example, one of these sets is $\{+ZIIIZX, +IZXZII, +ZZXZZX\}$. The expectation values of the first two stabilizers can be estimated from the result of projectively measuring C_6 in the $+ZZXZZX$ basis. Therefore, in reality, we estimated expectation values of 63 stabilizers from 37 measurement settings in total, which are shown in 3.13. The fidelity of the $|C_6\rangle$ state is estimated to be

$$\widehat{\mathcal{F}}(\rho, |C_6\rangle) = \begin{cases} 0.6061(17) & \text{from raw data} \\ 0.6639(19) & \text{SPAM-corrected.} \end{cases} \tag{3.54}$$

Finally, using the relation $\mathcal{F}(\rho, |C_6\rangle) = 2\Pr_Q[\text{win}] - 1$ for the CBF games, we obtain a raw success probability for winning this full-input game with our experimentally prepared

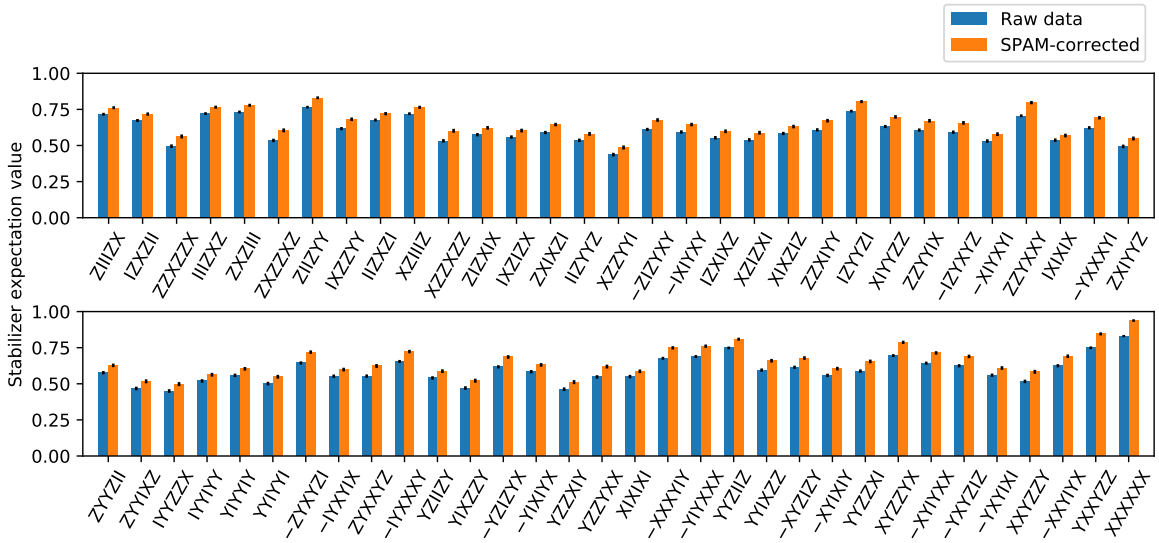

Figure 3.13: Estimated $|C_6\rangle$ stabilizer expectation values from our ion-trap experiment. This data allows us to evaluate the fidelity of our prepared state [Eq. (3.54)] and win probabilities for the cubic Boolean function games $\mathrm{CBF}(C_6, \{0,1\}^6)$ and $\mathrm{CBF}(C_6, \mathcal{I}^{(55)}_{\mathrm{Mermin}})$ [Eqs. (3.55) and (3.56), respectively]. The identity stabilizer is not included, as it trivially satisfies $\mathrm{tr}(\rho\mathbb{1}) = 1$. Each expectation value was estimated from $N = 5000$ shots, from which error bars of 1σ statistical uncertainties are reported. For explicit numerical values, as well as the grouping of simultaneously measured stabilizers that we employed, see Table D.1 in Appendix D

state ρ as

$$\widehat{\Pr}_Q[\mathrm{win}] = 80.30(8)\%. \quad [\mathrm{CBF}(C_6, \{0,1\}^6)\ \mathrm{game}] \tag{3.55}$$

This value significantly surpasses the classical bound of $23/32 \approx 72\%$.

Here, we have reported only the probability estimated from the raw data; we argue that any conclusions drawn from SPAM-corrected data in this context can be criticized. This is because the nonlocal game is evaluated on a shot-to-shot basis: a given output either does or does not satisfy the requisite win conditions. The final success rate is then merely an average over many individual shots (rounds of the game). SPAM correction, on the other hand, is a postprocessing technique that is necessarily applied to the observed distribution of outputs, rather than to each output individually. In contrast, we show corrected values to quantify the contribution of SPAM errors in our results and illustrate the quality of the entangled state created.

Using the same experimental data, we can also estimate our device's average success probability for the game $\mathrm{CBF}(C_6, \mathcal{I}^{(55)}_{\mathrm{Mermin}})$. This game was also recently implemented in Ref. [225] using IonQ's cloud-accessible quantum computer, where a winning probability of 87(1)% was reported. Using the data, we estimate

$$\widehat{\Pr}_Q[\mathrm{win}] = 79.51(9)\%, \ [\mathrm{CBF}(C_6, \mathcal{I}^{(55)}_{\mathrm{Mermin}}) \text{ game}] \tag{3.56}$$

far surpassing the classical bound of $37/55 \approx 67\%$. We remind the reader that this result corresponds to the raw output of our quantum device with no SPAM correction.

3.3.3 C_6 Stabilizer Submeasurement Games

In the previously discussed C_6 cubic Boolean function games, the quantum strategy can beat depth-0 classical strategies but depth-1 classical strategies have perfect win rate. We now move on to another class of games called stabilizer submeasurement games. Unlike the CBF games, the best depth-1 classical strategies are not perfect here.

In the C_6 stabilizer submeasurement game, each player receives a a one-bit input x_j, $j = 0, \ldots, 5$, from a global input $\mathbf{x} = (x_0, \ldots, x_5) \in \mathcal{I} \subseteq \{0,1\}^6$, drawn at random from a uniform distribution. With each input we can associate a global Pauli operator $E(\mathbf{1}, \mathbf{x}) = \prod_{j=0}^{5} i^{x_j} X_j Z_j^{x_j}$, where $\mathbf{1}$ denotes the all-ones string. Each party then produces an output $y_j \in \{0,1\}$, which collectively forms a string $\mathbf{y} \in \{0,1\}^6$. The parties are said to win the game whenever

$$\forall P \subseteq E(\mathbf{1}, \mathbf{x}) \text{ s.t. } P \in \mathcal{S}_{C_6} \sum_{j \in \mathrm{supp}(P)} y_j = 0, \tag{3.57a}$$

$$\forall P \subseteq E(\mathbf{1}, \mathbf{x}) \text{ s.t. } P \in -\mathcal{S}_{C_6} \sum_{j \in \mathrm{supp}(P)} y_j = 1, \tag{3.57b}$$

where $P \subseteq E(\mathbf{1}, \mathbf{x})$ means that P is a Pauli operator obtained by replacing some nonidentity tensor factors in $E(\mathbf{1}, \mathbf{x})$ with the identity. Furthermore, $\mathrm{supp}(P) = \mathrm{supp}(\mathbf{a}, \mathbf{b})$ where $P =$

$E(\mathbf{a}, \mathbf{b})$ (i.e., supp(P) indexes the qubits where P acts nontrivially) and all arithmetic is performed modulo 2.

The SS$(C_6, \mathcal{I})$ games always have a perfect quantum strategy wherein each party j holds one qubit from the state $|C_6\rangle$, measures it in the basis of X_j or Y_j if $x_j = 0$ or 1, respectively, and then outputs the measurement outcome. This strategy is proved to be perfect in Ref. [66] Appendix A. Classical strategies perform with varying success depending on the particular input set $\mathcal{I}$. Below we discuss classical strategies for two specific input sets.

2D hidden linear function (HLF) game

Fixing the input set to be

$$\mathcal{I}_{\text{HLF}}^{(8)} = \left\{ \mathbf{x} \in \{0,1\}^6 \;\middle|\; \begin{array}{l} (x_0, x_2, x_4) \in \{0,1\}^3, \\ x_j = 0 \text{ for all other } j \end{array} \right\}, \tag{3.58}$$

we have the game SS$(C_6, \mathcal{I}_{\text{HLF}}^{(8)})$.

As shown in [66] Appendix D, all geometrically restricted depth-0 and depth-1 fan-in ≤ 3 circuits cannot win this game on more than 7/8 inputs; however, there is a depth-2 circuit that wins on all inputs. Hence,

$$\Pr_C[\text{win}] \leq_{\text{Depth-0}} \frac{7}{8} \leq_{\text{Depth-1}} \frac{7}{8} \leq_{\text{Depth-2}} 1. \tag{3.59}$$

Restricted-input 2D hidden linear function (HLF) game

By restricting the input set to be

$$\mathcal{I}_{\text{HLF}}^{(5)} = \left\{ \mathbf{x} \in \{0,1\}^6 \;\middle|\; \begin{array}{l} (x_0, x_2, x_4) \in \mathcal{V}, \\ x_j = 0 \text{ for all other } j \end{array} \right\}, \tag{3.60}$$

where the set $\mathcal{V} \subset \{0,1\}^3$ is defined as

$$\mathcal{V} = \{(0,0,0),(0,1,1),(1,0,1),(1,1,0),(1,1,1)\}, \tag{3.61}$$

we obtain the game $\mathrm{SS}(C_6, \mathcal{I}^{(5)}_{\mathrm{HLF}})$. Analogous to how a restricted input set makes the game $\mathrm{CBF}(C_6, \mathcal{I}^{(55)}_{\mathrm{Mermin}})$ classically harder than $\mathrm{CBF}(C_6, \{0,1\}^6)$ (i.e., the depth-0 lower bound on $\Pr_C[\mathrm{win}]$ decreases), the same behavior occurs when restricting from $\mathcal{I}^{(8)}_{\mathrm{HLF}}$ to $\mathcal{I}^{(5)}_{\mathrm{HLF}}$. As shown in [66] Appendix D, the depth-0 and depth-1 classical bounds are reduced to

$$\Pr_C[\mathrm{win}] \leq_{\text{Depth-0}} \frac{4}{5} \leq_{\text{Depth-1}} \frac{4}{5} \leq_{\text{Depth-2}} 1. \tag{3.62}$$

Table 3.6: Experimental results for the stabilizer submeasurement games, $\mathrm{SS}(C_6, \mathcal{I}^{(8)}_{\mathrm{HLF}})$ and $\mathrm{SS}(C_6, \mathcal{I}^{(5)}_{\mathrm{HLF}})$. The rules and winning conditions of the game are described in Sec. 3.3.3. For each input, 5000 rounds of the game were played, from which we estimate a win rate and a 1σ statistical uncertainty. For completeness, we include the SPAM-corrected probabilities, although as argued in the main text, the proper figure of merit for claiming quantum computational advantage here (or lack thereof) is the raw value.

	Win rate (%)		Classical
Input	Raw value	SPAM-corrected	bound (%)
000000	80.42(56)	86.45(48)	-
000010	84.76(51)	87.85(46)	-
001000	83.92(52)	86.94(48)	-
001010	75.58(61)	81.12(55)	-
100000	85.04(50)	88.11(46)	-
100010	78.12(58)	83.98(52)	-
101000	78.46(58)	84.28(51)	-
101010	84.52(51)	87.56(47)	-
$\mathcal{I}^{(8)}_{\mathrm{HLF}}$	81.35(59)	85.79(53)	87.5
$\mathcal{I}^{(5)}_{\mathrm{HLF}}$	79.42(25)	84.68(23)	80

Experimental results for $\mathrm{SS}(C_6, \mathcal{I}^{(8)}_{\mathrm{HLF}})$ and $\mathrm{SS}(C_6, \mathcal{I}^{(5)}_{\mathrm{HLF}})$

We performed the game $\mathrm{SS}(C_6, \mathcal{I}^{(8)}_{\mathrm{HLF}})$ on our trapped-ion quantum computer. This game was also recently implemented in Ref. [225] on IBM, IonQ, and Honeywell's cloud-accessible

quantum computers. Their highest reported success probability was 85(1)%, using Honeywell's H0 trapped-ion device, which does not surpass the depth-1 classical bound of 87.5%.

In this experiment, we played 5000 rounds of the game per input to determine the average success probability for our device. The results for each input are presented in Table 3.6. The estimated average success probability is

$$\widehat{\Pr}_Q[\text{win}] = 81.35(59)\%, \quad [\text{SS}(C_6, \mathcal{I}^{(8)}_{\text{HLF}}) \text{ game}] \tag{3.63}$$

which is below the depth-1 classical bound.

Using the same experimental data from Table 3.6, we also estimate our device's average success probability for the game $\text{SS}(C_6, \mathcal{I}^{(5)}_{\text{HLF}})$. The estimated average success probability in this case is

$$\widehat{\Pr}_Q[\text{win}] = 79.42(25)\%. \quad [\text{SS}(C_6, \mathcal{I}^{(5)}_{\text{HLF}}) \text{ game}], \tag{3.64}$$

which is very close to meeting the depth-1 classical bound of 80%. The experimental results are shown in Table. 3.6.

3.3.4 Conclusion and Outlook

In this work, we have proposed and tested two types of nonlocal games, which can be interpreted as computational tasks that unconditionally prove quantum advantage against a particular class of geometrically restricted, shallow-depth classical circuits. We implemented proof-of-principle experimental demonstrations using six qubits on a trapped-ion quantum computer. As summarized in Table 3.5, our experimental results surpass the conventional depth-0 bounds for the cubic Boolean function games by a significant margin. These games also provide fine-grained details like state fidelity, which is useful for the characterization of noise in a quantum device. On the other hand, our results suggest that state-of-the-art devices are now at the level of challenging the more difficult depth-1 bounds of the stabilizer

submeasurement games.

While the work presented so far concerned only a six- qubit system, both games generalize nicely to the n-qubit scenario. Such games offer a scalable demonstration of the advantage that constant-depth quantum circuits have over geometrically restricted classical cir- cuits of depth linearly growing with n[66] Sec. VI. However, the demonstration of an advantageous quantum strategy for the C_n stabilizer submeasurement games gives a particularly meaningful separation against classical circuits with larger circuit depth. For example, the stabilizer submeasurement game on an 18-qubit device provides a clear future target, in that surpassing the corresponding bounds would demonstrate an advantage against depth-3 classical circuits. Indeed, as this classical depth is greater than the number of layers of two-qubit CZ gates without overlap, it would make more rigorous the comparison between the required quantum and classical circuits. Furthermore, these nonlocal games are friendly to a number of experimental platforms as their advantageous quantum strategies could generalize to condensed-matter platforms realizing 1D symmetry-protected topological order [65].

Note that after the completion of the work, it is brought to our attention that a new version of Ref. [225] reports, without detailed data, the Honeywell H1 processor [199] achieves a success probability of 96.9(3)% for the 2D hidden linear function game, which surpasses the depth-1 classical bound.

Chapter 4

Benchmarking and Error Characterization on a Trapped-Ion Quantum Computer

Quantum computers are inherently prone to noise, which can severely impact their capability to solve real-world problems. As the number of qubits in quantum computers increases, classical verification of computational results from quantum computers becomes impractical. At the same time, larger quantum systems tend to be noisier. Efficient error correction requires detailed knowledge about device noise. However, noise characterization usually require computational resources that scales exponentially with the system size.

This chapter explores two critical challenges in the advancement of quantum computing: the need for efficient protocols for output validation and noise characterization.

4.1 Cross-Platform Benchmarking of Arbitrary Quantum States

As the number of qubits in available quantum platforms scales up and classical simulation becomes difficult or intractable, it is vital that the output of quantum computers can be verified. While algorithmic success can be easily checked in some instances such as factoring or oracular algorithms, these approaches only provide pass/fail information for executing specific tasks for a single quantum computer. Validation for more general tasks remains a challenge. As an analogy to evaluating atomic clocks, one natural approach is to compare one quantum computer to another of its own.

The fully quantum-mechanical way to compare generic output from different quantum computers is to coherently teleport information from one system to the other using a quantum link or quantum internet and compare the output locally[43, 148], for example with a swap test. However, such a quantum internet is extremely challenging to build, and high-fidelity teleportation of large quantum states is not yet feasible. Another approach is full quantum state tomography [28]. The drawback is the exponential scaling of resource cost with system size. One can argue that there exist more efficient tomography protocols for transforming quantum information to classical measurements. However, these protocols generally rely on knowing some information about the theoretical target and using this exact knowledge to improve their efficiency[20, 62, 90, 108], which is not applicable to the general cases.

The following discussion attempts to answer this question: Can we perform this comparison more efficiently than full-state tomography, before a quantum internet becomes available?

Randomized measurement-based fidelity estimation protocols still scales exponentially with the number of qubits. However, it has a significantly smaller exponent prefactor compared with full quantum state tomography [8], allowing scaling to intermediate-sized quantum computer systems. These methods usually allow efficient evaluation of functions of a density matrix ρ without full reconstruction of ρ. We demonstrate a cross-platform compar-

ison based on randomized measurements [49, 77, 128], obtained independently over different times and locations on several disparate quantum computers built by different teams using different technologies. We compare the outcomes of four families of quantum circuits and and show that the randomized measurement-based methods have good enough resolutions to reveal differences between platforms. We also investigate the intra-technology similarities and differences between the underlying hardware platforms.

4.1.1 Randomized Measurement-Based Fidelity Estimation Protocols

There are multiple ways to estimate fidelity within a common framework of randomized measurement-based protocols. We investigate the validation problem in the following settings. Imagine asking two quantum computers to prepare the same quantum state ρ. Both quantum computers will perform state preparation to their best ability, resulting in states ρ_A and ρ_B respectively. How to determine how similar ρ_A and ρ_B are or what is the cross-platform fidelity between these two states? Note even when the target state ρ is a pure state, ρ_A and ρ_B can still be mixed due to noise processes in quantum devices. Hilbert-Schmidt metric (Eq.4.1) is one way to quantify the overlap between two mixed states. We chose to use F to quantify the cross-platform fidelity for the rest of the chapter.

$$F = \frac{tr(\rho_A \rho_B)}{tr(\rho_A^2) tr(\rho_B^2)} \tag{4.1}$$

F can be extracted from randomized measurement results on ρ_A and ρ_B. In the experiment, ρ_A and ρ_B are prepared by initializing N qubits in the state $|0, 0, \ldots, 0\rangle$ and applying the unitary V on each platform. Then a distinct combination of random single-qubit rotations $U = u_1 \otimes u_2 \otimes \cdots \otimes u_N$ are sampled and appended to the state preparation circuit before performing projective measurements in the computational basis. This process is repeated M_U times, allowing us to measure the quantum states in M_U unique bases. An example cir-

cuit is shown in Fig. 4.1 a. For each rotation setting U, the measurements are repeated M_S times("shots") on each platform. F can be inferred from the randomized measurement results via either the statistical correlations between the randomized measurements[77] (Protocol I) or constructing an approximate classical representation of a quantum state using randomized measurements, the so-called the classical shadow [1, 128] (Protocol II).

Classical correlation-based protocol

In Protocol I, we calculate the second-order cross-correlations [77] between the outcomes of the two platforms i and j via the relation

$$\mathrm{Tr}[\rho_i \rho_j] = 2^N \sum_{s,s'} (-2)^{-D[s,s']} \overline{P_U^{(i)}(s) P_U^{(j)}(s')}, \tag{4.2}$$

where $s = s_1, s_2, ..., s_N$ is the bit string of the binary measurement outcomes s_k of kth qubit, $D[s, s']$ is the Hamming distance between s and s', which equals to the number of qubits with different outcome between s and s'. $P_U^{(i)}(s) = \mathrm{Tr}[U\rho_i U^\dagger |s\rangle\langle s|]$, and the overline denotes the average over random unitaries U.

Shadow tomography

The second protocol we use to extract cross-platform fidelity combines shadow tomography with randomized measurement. This method builds a classical shadow from each randomized measurement shot and reconstructs the overlap between density matrices from these classical shadows. The classical shadow of the quantum state for each shot of measurement is constructed as $\hat{\rho} = \bigotimes_{k=1}^{N} (3u_k^\dagger |s_k\rangle\langle s_k| u_k - I)$, where I is the 2×2 identity matrix [1, 128]. The overlap can be calculated as [128]

$$\mathrm{Tr}[\rho_i \rho_j] = \overline{\mathrm{Tr}[\hat{\rho}_i \hat{\rho}_j]}, \tag{4.3}$$

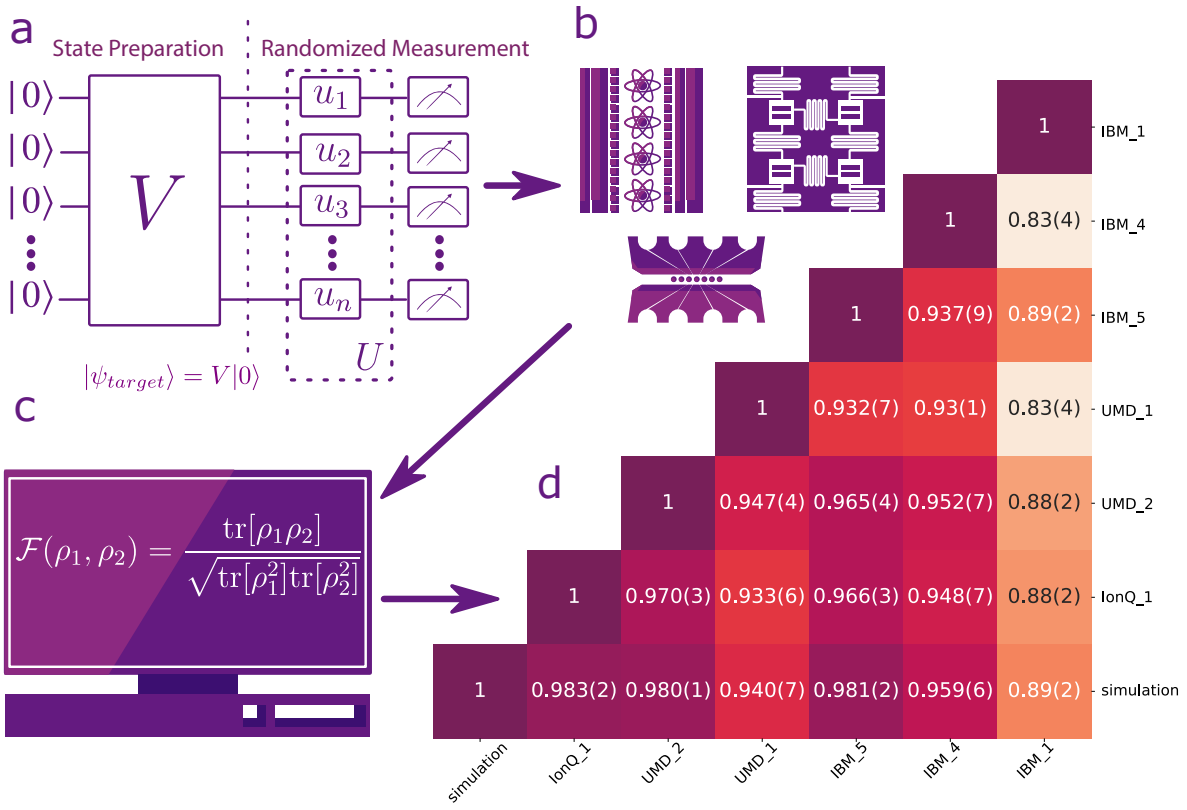

Figure 4.1: Schematic diagram of the cross-platform comparison. **a,** Test quantum circuit, represented by unitary operator V for state preparation, with appended random rotations u_i to each qubit i for measurements in a random (particular) basis. **b,** The circuits are transpiled for different quantum platforms into their corresponding native gates. Each of the M_U circuits is repeated M_S times for each platform. **c,** The measurement results are sent to a central data repository for processing the fidelities defined in Eq. (4.1). As an example, **d,** shows the cross-platform fidelity results for a 5-qubit GHZ state, including a row of comparisons between each of the six hardware systems and theory (labeled "simulation"). Entry i, j corresponds to the cross-platform fidelity between platform-i and platform-j. The cross-platform fidelity is inferred from $M_U = 100$ randomized measurements and $M_S = 2000$ repetitions for each U.

where the overline denotes the average over all the experimental shots for all random basis. We note that, for both protocols, unbiased estimators are necessary when calculating the purity $i = j$[77, 128] using Eq. (4.2) and (4.3).

4.1.2 Scaling and Performances

The fidelity inferred from the two protocols is identical in the asymptotic limit with $M = M_S \times M_U \to \infty$. We evaluated the resource overhead and found that Protocol II converges faster in the number of random unitaries M_U[128], while Protocol I is less costly in post-processing. As a result, Protocol II are applied to all 5- and 7-qubit experiments and Protocol I for the 13 ion experiments in this study.

4.1.3 Experimental Platforms

The platforms that participated in this study included four trapped-ion platforms and five IBM superconducting platforms. The four ion-trap platforms are the University of Maryland (UMD) EURIQA system [76] (referred to as UMD_1), the University of Maryland TIQC system [266] (UMD_2), and two IonQ quantum computers [167, 258] (IonQ_1, IonQ_2). The five separate IBM superconducting quantum computing systems are hosted in New York, *ibmq_belem* (IBM_1), *ibmq_casablanca* (IBM_2), *ibmq_melbourne* (IBM_3), *ibmq_quito* (IBM_4), and *ibmq_rome* (IBM_5) [131]. More details of these systems can be found in Ref. [63, 70, 76, 131, 177, 187].

Each trapped ion system has all-to-all connectivity, while superconducting systems have nearest-neighbor interaction available. UMD1 had 13 qubits in a micro-fabricated surface trap with a high numerical aperture(NA) objective and fiber-coupled detection system, eliminating detection crosstalk. Therefore SPAM correction was not needed for data from UMD1. The IonQ_1 and IonQ_2 systems both use linear Paul traps with surface electrodes, and no SPAM correction was applied to data from these two systems. UMD2 system located in UMD GATES lab has up to 9 qubits in a linear Paul trap with blades. Detection is done by

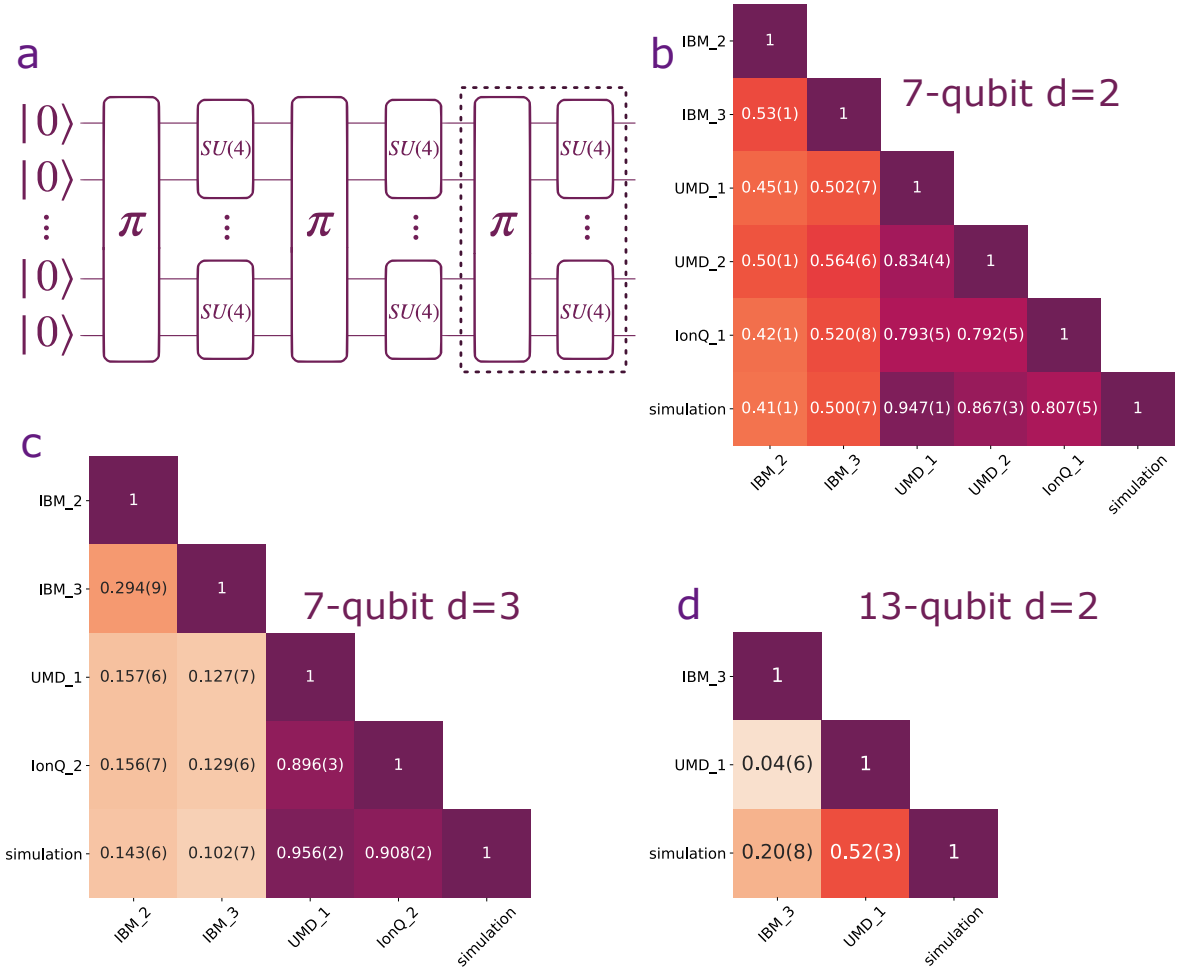

Figure 4.2: **a,** The quantum volume circuit diagram for $d = 3$. The $d = 2$ case does not have the operations in the dashed rectangle. **b** to **d,** Cross-platform fidelity between different quantum computers. Entry i, j corresponds to the cross-platform fidelity $\mathcal{F}(\rho_i, \rho_j)$ between platform-i and platform-j as defined in Eq. 4.1. **b,** $N = 7$ and $d = 2$; **c,** $N = 7$ and $d = 3$; **d,** $N = 13$ and $d = 2$. UMD_2 did not participate in the 13-qubit $d = 2$ and 7-qubit $d = 3$ because of the limitation in qubit number and also because this experiment is not fully automated as UMD_1 and IonQ_2. It would have been challenging to collect the data required for the 7-qubit $d = 3$ experiment in terms of experiment time.

focusing the state-dependent fluorescence of each ion onto a different PMT channel with free-space optics, relying on the spatial separation of the focused images of the ions. Crosstalk during detection is larger in this system compared with the previously mentioned trapped-ion systems. SPAM correction has been applied to all experimental data from UMD2. Additionally, we accessed five IBM superconducting quantum machines via their cloud service, We applied measurement error mitigation for all the superconducting data, as these platforms are affected by measurement errors.

4.1.4 5-qubit GHZ Experiment

We first demonstrate the application of randomized measurements for comparing 5-qubit GHZ (Greenberger–Horne–Zeilinger) states[104] generated on different platforms and the ideal 5-qubit GHZ state obtained from classical simulation. Later, using the same protocol, we also compare states generated with three random circuits of different widths and depths, each sharing a similar construction to circuits used in quantum volume (QV) measurements [137].

We distributed the circuits for GHZ preparation and randomized measurements across all participating platforms, allowing them to compile and optimize it locally before implementation under the principle that the 5-qubit GHZ state has to exist in the system before the basis rotation and projective measurements are performed. We chose the $243 = 3^5$ five-qubit Pauli strings as the randomized measurement basis $U \in \{X, Y, Z\}^{\otimes 5}$, which aligns with previous unitary sets discussed in Sec. 4.1.1. This is a valid random unitary transformation for the classical shadow analysis used in this work [128]. Since the Pauli basis is a tomographically complete basis, we have all the measurements needed for a full quantum state tomography. Each circuit is repeated for $M_S = 2000$ shots. We sample $M_U = 100$ out of the 243 different Us to calculate $\mathcal{F}$.

The results in Fig. 4.1d showed high cross-platform fidelities between the simulation and 5 machines (UMD_1,UMD_1,IonQ_1,IBM_4, and IBM_5) as well as among the 5 machines.

The good agreement with simulation indicates these platforms performed well in GHZ state preparation. And when this is the case, it is reasonable that the 5 platform also highly agree with each other. The results from IBM_1 do not have a good overlap with any other platforms. We see that our method has a good enough resolution to reveal the performance difference between platforms. We also benchmark our method against full quantum state tomography by computing the fidelity as a function of M_U. The fidelity error $|\mathcal{F}_e - \mathcal{F}|$ is defined as the difference between the fidelity estimated by the randomized measurement $\mathcal{F}_e$ and the fidelity calculated through full state tomography $\mathcal{F}$. The average of $|\mathcal{F}_e - \mathcal{F}|$ and the standard deviation are calculated through a bootstrap resampling method [75]. The comparison in Fig. 4.3 shows the fidelity obtained via randomized measurement approaches obtained via the full quantum state tomography rapidly, demonstrating the efficiency and accuracy of the randomized approach.

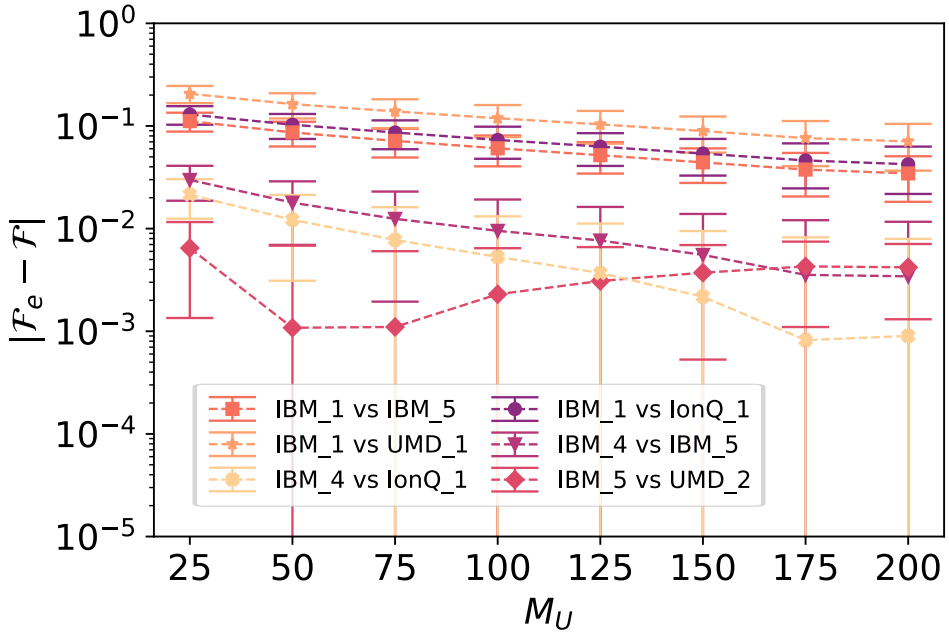

Figure 4.3: Fidelity error, $|\mathcal{F}_e - \mathcal{F}|$, for six randomly selected 5-qubit GHZ state cross-platform fidelities implemented on different platforms vs. the number of randomized measurements M_U. The number of measurement is $M_S = 2000$ for all cases.

4.1.5 7 and 13 Qubits QV-like Experiments

Next, we benchmarked a quantum state prepared by a quantum volume-like circuit[64, 137, 198], which consists of layers of unitaries with random permutations of qubit labels followed by random nearest-neighbor entangling gates drawn from SU(4). This construction resembles a quantum volume circuit but with fewer layers. QV circuits have been studied extensively, both theoretically and experimentally, making them an ideal choice for cross-platform comparison. Also, quantum volume provides a single-number metric for the overall performance of one quantum computer. However, in our randomized measurement scheme, we estimate many observables from randomized measurement data by using Protocol II.

Specifically, an N-qubit QV circuit consists of $d = N$ layers: each layer contains a random permutation of the qubit labels, followed by random two-qubit gates among every other neighboring pair of qubits. In our study, we call circuits of such construction but different circuit depth d QV-like circuits. A QV-like circuit can be written as a unitary operation $V = \prod_{i=1}^{d} V^{(i)}$, where $V^{(i)} = V^i_{\pi_i(N'-1),\pi_i(N')} \otimes \cdots \otimes V^i_{\pi_i(1),\pi_i(2)}$ and $N' = 2\lfloor N/2 \rfloor$. The operation $\pi(a)$ is a random permutation sampled from the permutation group S_N, of which the elements are all permutations of qubit labels. The unitary operation $V^i_{a,b}$ is a random two-qubit gate acting on qubits a and b and sampled from $SU(4)$. The circuit diagram of an example QV-like circuit is shown in Fig. 4.2 a. In this experiment, we infer the fidelity for 7-qubit QV-like states with $d = 2$ and $d = 3$, each with $M_U = 500$ randomized measurements, and a 13-qubit QV-like state with $d = 2$ and $M_U = 1000$ randomized measurements. Notably, a full state tomography of the 13-qubit system would require an astronomically large number of measurements $M_U = 3^{13} = 1594323$ and is impractical to implement, but our randomized protocol provided sensible results with far fewer.

Similar to the GHZ case, we first distribute the circuits, synthesize them into device-specific native gates, and allow optimizations/error-mitigation that satisfies the aforementioned state-preparation rule. The cross-platform fidelities for 7-qubit QV-like states with $d = 2$ and $d = 3$ are shown in Figs. 4.2 b,c. Our results verify that with only a fraction

of the number of measurements required to perform full quantum state tomography, we can estimate the fidelities to sufficiently high precision to be able to see clear differences among them. The cross-platform fidelities for a 13-qubit QV-like circuit with $d = 2$ are shown in Fig. 4.2d.

We find several interesting features by analyzing the cross-platform fidelity of 7-qubit QV-like results. First, we observe that the cross-platform fidelity drops significantly when the number of layers d increases from $d = 2$ to $d = 3$ for the IBM quantum computers. The drop may be due to the restricted nearest-neighbor connectivity of superconducting quantum computers [168], requiring additional SWAP gates overhead for the execution of the permutation gates. We see that according to IBM's native compiler QISKit), extra entangling gates are used to perform two-qubit gates for non-nearest-neighbor qubits on superconducting platforms, resulting in extra errors.

The cross-platform fidelity between the two superconducting machines, IBM_2 and IBM_3, is higher than the cross-platform fidelity between either of them and ion-trap systems or the classical simulation. This indicates that even though these two systems have prepared relatively faulty states, these two states are faulty in a similar way. This motivates us to study whether quantum states generated from different devices tend to be similar to each other if the underlying technology of the two devices is the same. Therefore, we perform a further analysis to investigate this phenomenon, which we refer to as intra-technology similarity.

4.1.6 Intra-Technology Similarity

Subsystem study

The subsystem fidelity provides a scalable way to estimate the upper bound for the full system fidelity since the cost of measuring all possible subsystem fidelities of a fixed subsystem size scales polynomially with the full system size. We first study the fidelity between subsystems of the 7-qubit QV-like states prepared on different quantum computers for both

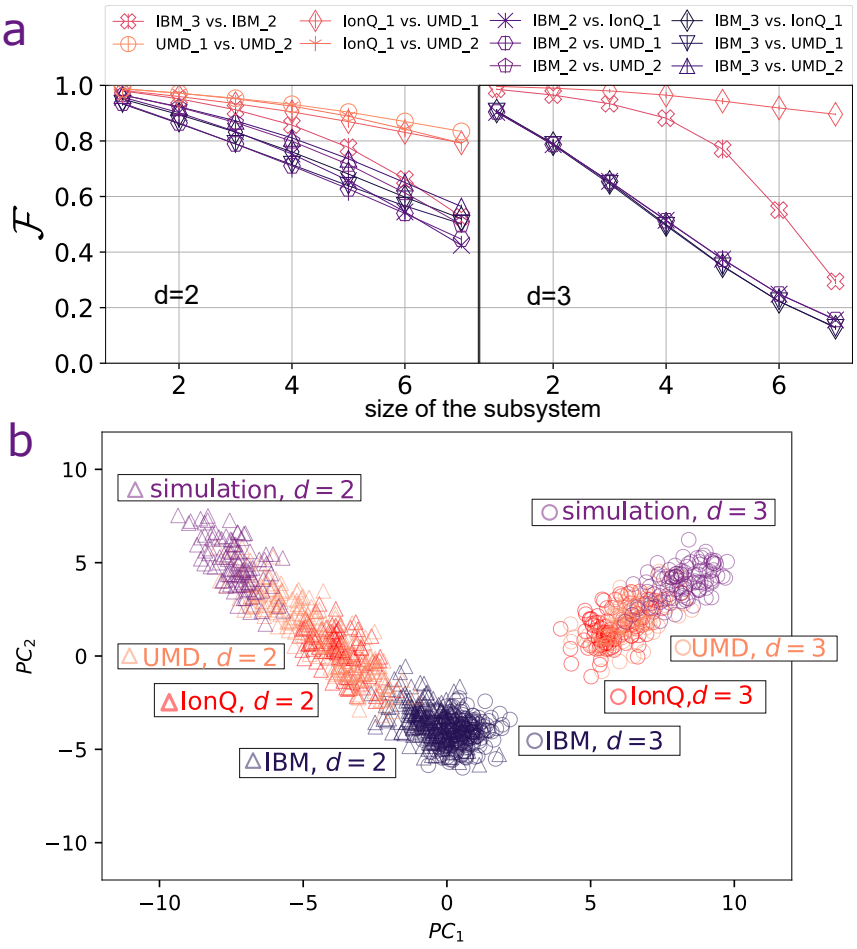

Figure 4.4: **a,** The cross-platform fidelity between subsystems prepared on different quantum computers. Left : 7-qubit quantum volume circuit of 2 layers. Right: 7-qubit quantum volume circuit of 3 layers. The mean for each subsystem size is calculated via bootstrap re-sampling. **b,** The projection of randomized measurement dataset onto the first two principal axes, PC_1 and PC_2. Triangle marker is the 7-qubit quantum volume state with $d = 2$. Each modality set contains data from all hardware used. For example, data labeled "UMD" contained data from both UMD_1 and UMD_2. Circle marker is the 7-qubit quantum volume state with $d = 3$. Magenta, orange ,and violet correspond to simulation, trapped-ion, and IBM systems respectively.

$d = 2$ and $d = 3$. For a given subsystem, we use the same data collected for the full system but trace out qubits not within the subsystem of interest. Cross-platform fidelities between different platforms for various subsystem sizes are plotted in Fig. 4.4 a. We observe that the cross-platform fidelity between systems with the same technology (ion-ion and superconducting-superconducting)is consistently higher than cross-platform fidelites between systems with different underlying technologies (ion-superconducting) for all subsystem sizes. This distinction becomes even clearer in the data set for the depth-3 circuit. Notably, in the first half of the figure, the data indicated by the cross symbol represents the comparison between the two IBM machines. Despite having a high overlap between themselves, these machines already show a significant difference when compared with the trapped ion machines. It also makes sense that this effect is more obvious in $d = 3$ than $d = 2$ since the results of $d = 3$ is more dominant by error than $d = 2$.

principal component analysis

To further characterize the intra-technology similarity, we perform principal component analysis[136] (PCA), an unsupervised machine learning technique, on the randomized measurement data for the 7-qubit quantum volume states with $d = 2$ and $d = 3$. PCA is commonly used to reduce the dimensionality of a dataset. It has been applied extensively in signal processing such as human face recognition and audio compression. Intuitively, the dataset data is regrouped, averaged, and then projected into a feature space represented by feature vectors during the process. The feature space is rotated to identify principal axes that show the most significant differences between data sets. This allows us to obtain lower-dimensional data, which represents the condensed key characteristics of the original data, while preserving as much of the variation as possible.

To prepare the data for PCA, we randomly sample 1000 shots from the randomized measurement data out of $M_U \times M_S = 1,000,000$ for each platform. We identify the set of Pauli strings whose expectation values can be evaluated using the sample. We then

evaluate the expectation value of these identified Pauli strings by taking the average over the samples, and repeating the sampling $N_{\text{sample}} = 500$ times without replacement to make N_{sample} data points in the 4^N dimensional feature space. The feature vectors represent the averaged classical shadow of the quantum state generated from the quantum computers [128, 129]. We perform a rotation on the feature space and find the first two principal axes, which are the axes that show the two most significant variances on the dataset. Figure. 4.4b shows the projection of the N_{sample} data points to the first two principal axes. We observe that the first principal component separates the two quantum volume states, and the second principal component can distinguish the technology that generates the states. The clustering of the data from the same technology indicates that each technology may share similar noise characteristics that can be distinguished through the cross-platform fidelity and machine-learning techniques.

Fig. 4.4 (b) shows the projection of our experimental data onto the two principal axes that capture the most significant variance among the data sets. Light purple data points represent simulations, with those on the left corresponding to the depth-2 circuit and those on the right to the depth-3 circuit. Orange and reddish data points are from trapped ion platforms, while the dark purple data points are from IBM superconducting platforms. From this figure, we observed that quantum states are separated along principal axis one (the horizontal axis), as all data for the depth-2 circuit cluster is on the left, while depth-3 data are on the right. Additionally, different quantum platforms exhibit a clear separation along the y-axis, which corresponds to principal axis two. Light purple data points have similar y-values, as do the green, red, and orange data points. Moreover, data tend to cluster together for the same technology and quantum state. We believe this clustering occurs because platforms with the same underlying technology share similar noise characteristics, which influences their positioning along the principal axes.

4.1.7 Summary and Outlook

We performed the cross-platform comparison of four quantum states between up to six systems using randomized measurement-based methods with significantly fewer measurements than those required by full quantum state tomography. We showed that randomized-based protocol have good enough resolution to reveal difference between different platforms. Additionally, we explored intra-technology similarity by examining cross-platform fidelities of subsystems of various sizes and performing principal component analysis. To expand our understanding of the intra-technology similarity, more quantum states, in particular those designed to probe the effect of different settings on the cross-platform comparison results, should be studied. Our method could be extended to additional technological platforms such as Rydberg atoms and photonic quantum computers[105]. With the large volume of quantum data generated from the randomized measurement protocol, we have only begun to explore the possibilities that machine learning techniques can offer. We envision extensions of our method will be indispensable in quantitatively comparing near-term quantum computers, especially across different qubit technologies.

4.2 Entanglement-Assisted-Benchmarking on a TIQC

Learning the noise in quantum systems can not only guide future low-noise hardware design but also inform efficient and high-performance error mitigation, error correction code and fault-tolerance scheme co-design. The performance of error correction codes depends significantly on the noise environment [29, 176, 189, 236, 237, 239]. Much research effort has been dedicated to adapting existing error correction codes and designing new codes for tailored noise models to reduce resource overhead or to improve performance [102, 162, 181, 238, 239]. Realistic noise models can also allow more accurate threshold and overhead estimates for quantum error correction [195].

The challenge remains that the cost for full characterization of quantum noise scales exponentially with system size and with an even larger prefactor than quantum state tomography. Additionally, in order to justify the validity of most noise characterization protocols, assumptions usually need to be made on the noise environment in the system, such as whether it is Markovian or time-independent [78, 151]. Certain operations, such as single-qubit rotation, and qubit initialization and measurement, are often assumed error-free. Reality deviates from these assumptions, adding more complexity to performing accurate characterization.

Pauli noise is a subset of quantum noise that can be interpreted as probabilistic Pauli errors. Pauli noise is a particularly useful model because it not only captures the characteristics of a wide range of incoherent noises presented in real quantum devices but also can be efficiently simulated on classical computers, and therefore becomes the most basic and widely used model in studies of quantum error correction and fault tolerance. Although noise mechanisms in real quantum devices are generally not purely Pauli, the randomized compiling technique, which maps general quantum noise to its Pauli projection, has been proved to work very well in practice [119, 248, 252]. Furthermore, researchers have found that biased Pauli channels, where some Pauli error occurs more often than others, are more realistic descriptions than depolarizing noise, where all Pauli errors occur at the same probability. This motivates more detailed characterizations of real-device noises and the use of more accurate

noise models in resource evaluation and code design for quantum error correction [239].

In collaboration with a theory team at the University of Chicago, we investigate an ancilla-assisted protocol for efficient characterization of Pauli noise [54]. This protocol provides exponential speedup over any ancilla-free Pauli noise characterization methods. We perform the first experimental validation of this protocol in a noise environment native to trapped ion machines and benchmark it against an ancilla-free protocol. We propose and demonstrate a new method to improve its performance on trapped-ion architecture. In this work, we focus on learning Pauli fidelities, a set of values that can fully describe Pauli noises.

4.2.1 Noise characterization and common challenges

In noise characterization, a trade-off between resource cost and the amount of information learned always exists as depicted in Fig. 4.5. The resource cost usually refers to the number of measurements required for characterization. Full process tomography and self-consistent gate set tomography [190] are examples of high-cost high-gain protocols that theoretically provide all learnable information about a quantum channel or a quantum gate set, but the number of measurements scales exponentially with system size. On the low-cost low-gain side, protocols such as Randomized Benchmarking (RB) [152] scale favorably with system size while only producing a single number describing the average fidelity of a gate set[67, 151]. Many protocols that have been developed lie in between as shown in Fig. 4.5, which is inspired by a presentation given by J. Helsen. The particularly interesting region is the upper-left quadrant, where partial information about the process, for example, its Pauli projection, is provided while maintaining non-exponential scaling. In reality, full information about the process is not always needed, only key characteristics. In those cases, full tomography is unnecessary, and these protocols provide practical and economical alternatives.

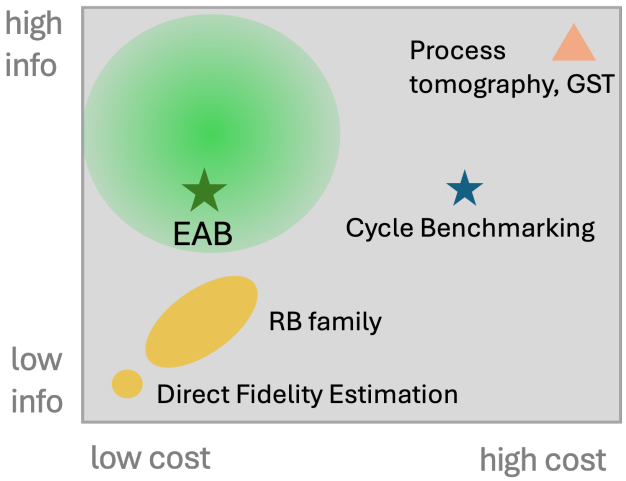

Figure 4.5: This figure compares the resources cost vs. information gain of several representative benchmarking methods. The green circle highlights the quadrant where ideal benchmarking protocols that are low-cost and high-gain lie. This thesis work validates the lower-cost EAB against the widely tested, but more expensive, Cycle Benchmarking technique.

Quantum Channels

Noise processes in quantum systems often originate from unwanted entanglement between the system, where useful information is stored and processed, and the environment. At initial time t_0, the system ρ_s and the environment ρ_e are in a product state $\rho = \rho_s \otimes \rho_e$. The combined system evolves under unitary U. If we only look at the system state ρ_s' after the evolution by tracing out the environment, $\rho_s' = \mathrm{tr}_{env}(U\rho_s \otimes \rho_e U^\dagger) = \mathcal{E}(\rho_s)$. ρ_s' can be mixed state. The evolution of the system alone under the influence of the environment (noise), can be expressed as quantum channel $\mathcal{E}$, which is not necessarily unitary. Unitary evolutions are special cases of general quantum channels. There are several different mathematical conventions for the representation of quantum channels. Since we will be working with Pauli noise later, the two most convenient representations are the process matrix (or Chi matrix) and the Pauli Transfer Matrix (PTM), both defined in the Pauli basis.

A general quantum channel can be written in the operator-sum representation as

$$\mathcal{E}(\rho) = \sum_k E_k \rho E_k^\dagger, \tag{4.4}$$

where $\sum_k E_k E_k^\dagger = I$, so that $\mathcal{E}$ is trace-presevering. E_k and $E_k^\dagger$ are called Kraus operators. Since we will be studying Pauli noise, it is useful to rewrite the expression in the Pauli basis. Each operator E_k can be expanded as

$$E_k = \sum_{j=0}^{4^N-1} c_{kj} P_j, \tag{4.5}$$

where N is the number of qubits in the system and $P_i \in \{X, Y, Z, I\}^{\otimes N}$. Rewrite Eq. (4.4) as

$$\mathcal{E}(\rho) = \frac{1}{2^N} \sum_{i,j} \chi_{i,j} P_i \rho P_j, \tag{4.6}$$

Matrix χ of dimension $2^{2N} \times 2^{2N}$ is the chi matrix representation of $\mathcal{E}$.

The Chi matrix is a useful description of the quantum process. But it can not be directly used to evolve quantum operators by matrix multiplication. The matrix representing a quantum channel in the Superoperator formalism can act on vectorized quantum operators directly. A superoperator is a linear operator acting on the vector space of linear operators. The Pauli Transfer Matrix (PTM) representation of $\mathcal{E}$, of dimension $2^{2N} \times 2^{2N}$, is

$$R_{i,j} = \frac{1}{2^N} \mathrm{tr}(P_i \mathcal{E}(P_j)). \tag{4.7}$$

The vectorized form of the density matrix of an N-qubit system $\rho = \sum_{i,j} \rho_{ij} |i\rangle \langle j|$ is

$$|\rho\rangle\rangle = \sum_{i,j} \rho_{ij} |i\rangle \otimes |j\rangle \tag{4.8}$$

In this representation, the channel is applied to the state by multiplication. After the

evolution, the state is $|\rho'\rangle\rangle = |\mathcal{E}(\rho)\rangle\rangle$

$$|\rho'\rangle\rangle = R|\rho\rangle\rangle \tag{4.9}$$

Both the χ and R matrix give a full description of a quantum channel. However, full characterization is a challenging task since the computational resources scale exponentially with the system size N. As a result, full process tomography has only been done for systems with a very small number of qubits.

Pauli Channels

Pauli channels are special quantum channels whose eigenoperators are exactly the Pauli operations. Pauli channels apply a set of Pauli errors following certain probability distributions. Hence, they can be written as Eq. (4.10). Compared to the description of a general channel in Eq. (4.6), a Pauli channel only contains terms where $P_i = P_j$, and its χ matrix is diagonal in the Pauli basis. The diagonal elements $\boldsymbol{p} := \{p_k\}_k$ are referred to as Pauli error rate. p_k can be understood as the probability of Pauli error P_k.

$$\Lambda(\rho) = \sum_a p_a P_a \rho P_a \tag{4.10}$$

The PTM representation of a Pauli channel is Eq. 4.11, where λ_b are called Pauli fidelities or Pauli eigenvalues. The physical meaning of Pauli fidelity can be seen when we set $\rho = P_i$ and $\Lambda(P_i) = \lambda_i P_i$. The λ_i describe how much Pauli operator P_i is preserved when it is sent through channel Λ. It is easy to see that $\lambda_{II} = 1$ is always true.

$$\Lambda(\rho) = \frac{1}{2^N} \sum_b \lambda_b \mathrm{Tr}[P_b \rho] P_b \tag{4.11}$$

Pauli fidelities and Pauli error rates are related to each other through the Walsh-Hadamard

transform. Knowing one set of values will allow us to calculate the other.

$$p_a = \frac{1}{4^n} \sum_b \lambda_b (-1)^{\langle a,b \rangle}, \lambda_b = \sum_a p_a (-1)^{\langle a,b \rangle} \tag{4.12}$$

Pauli Channel Estimation

Although compared to a general quantum channel with 2^{4N} elements in its chi matrix or PTM, Pauli channels have a reduced number of elements (2^{2N} elements), the full description of a Pauli channel still scales exponentially with the system size. Efficient learning of Pauli channels is a nontrivial and essential task. Despite many efforts (cite works), the sample complexity of Pauli channel estimation has not been fully established.

Cycle Benchmarking (CB) is a recently developed Pauli channel learning protocol[78] among others. In a full Pauli channel estimation with CB, the system is prepared in the eigenstate of each N-qubit Pauli term and measured in a corresponding basis (with the caveat that some terms can be saved). The number of different circuits required scales exponentially with system size. The experimental resources required by CB are too large, and even the authors of its original paper were not able to fully characterize a 6-qubit Pauli channel with CB.

4.2.2 Entanglement-Assisted Benchmarking (EAB) of Pauli Channels

EAB utilizes ancilla qubits to significantly reduce the resources needed for Pauli channel characterization. It can be combined with a concatenation technique inspired by RB, which will be introduced later, for robustness against SPAM errors. The more ancilla qubits are included in the protocol, the fewer measurements are needed, and with the maximum number of ancillae N, the sample size required to fully learn an N-qubit Pauli channel scales linearly with N. A more generalized version of the algorithm is presented in [54]. We described its application in characterizing quantum noise associated with a specific group of quantum

gates with the maximum number of ancillae. Compared to many other platforms, trapped-ion qubits have longer gate times and lower ancilla error, therefore they are suitable for us to trade more ancillae for fewer circuits.

Protocol

First, we explain how the protocol efficiently measures Pauli channels with the smallest example consisting of one data qubit and one ancilla qubit shown in Fig. 4.6. The data and ancilla qubit pair is initialized in the $|\Psi^+\rangle = \frac{1}{\sqrt{2}}(|00\rangle + |11\rangle)$ state. The principle behind this method is similar to that of teleportation. Fig. 4.6 (a) illustrates that if a Pauli error $P \in \{I, X, Y, Z\}$ occurs on the data qubit followed by a Bell measurement, the specific Pauli error can be uniquely identified by the outcome of the Bell measurement. Each outcome in the computational basis state is associated with a different value of P. In Fig. 4.6 (b), a Pauli channel Λ is acting on the data qubit. Since Λ can be understood as probabilistic Pauli noise, in each experimental shot Λ manifests as a Pauli error P which can be determined from the measurement result of that shot. In order to know the Pauli fidelity λ_k of $P_k \in \{X, Y, Z, I\}$, we repeat the experiment for M_s shots, and record the number of shot $M_k^{commute}$ for which $[P_k, P] = 0$. When $[P_k, P] = 0$, P_k commute through the error in this shot and is preserved. $\mathcal{F}_{\lambda_k}$ denotes $M_k^{commute}/M_s$. By definition $\mathcal{F}_{\lambda_k}$ equals to λ_k. All λ_k can be constructed simultaneously as long as we know P for each experimental shot, and this means that a full description of Λ can be obtained from just implementing one measurement setting M_s times. Generalizing to the N data qubits and N ancillea case, M_s will increase in order to reduce statistical uncertainty. However, the number of measurement settings does not change. The total sample size scales as $O(\frac{N}{\epsilon^2})$, where ϵ is the additive error on the measured λ_k. In the experiment, the Bell state preparation and measurement are not error-free operations. An RB-inspired concatenation technique can be combined with the protocol described above to achieve SPAM-robustness. A sketch of the idea of concatenation is in Fig. 4.6. Specifically, a list of depths $\boldsymbol{d} = [d_1, d_2, ..., d_m]$ is constructed. The circuit in

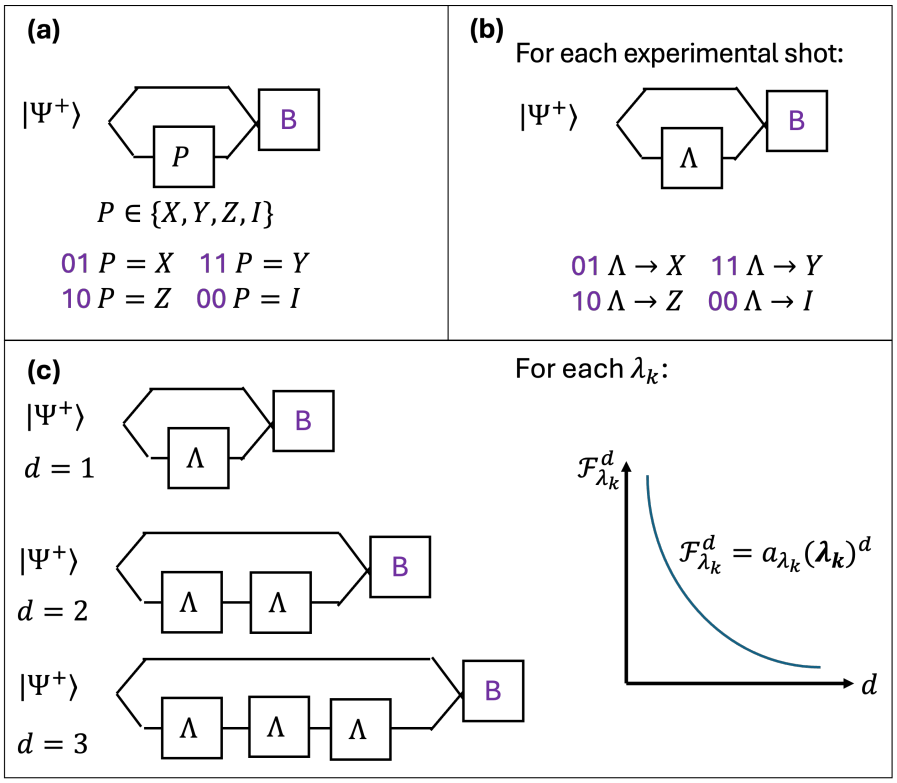

Figure 4.6: (a) Measuring single-qubit Pauli error with EAB. A Pauli error P occurs on one of the qubits in a Bell pair Ψ^+. The purple B represents a Bell measurement. The purple numbers 01,11,10, and 00 are possible measurement outcomes in computational basis. Each outcome corresponds to one possible value of P. Based on the measurement outcome, P can be uniquely identified. (b) Measuring single-qubit Pauli channel Λ with EAB. For each experimental run, the measurement result corresponds to one single-qubit Pauli operator or I. Over many shots, statistical information about Λ can be extracted. (c) A sketch of the idea of concatenation. In the circuits of different depths on the left, Λ is repeated 1,2 and 3 times respectively, corresponding to $d = 1, 2, 3$. $\mathcal{F}^d_{\lambda_k}$ is extracted from results for circuit of depth d and fitted to function $\mathcal{F}^d_{\lambda_k} = a_{\lambda_k}(\lambda_k)^d$ with respect to d. a_{λ_k} is determined by SPAM and does not affect the extract of λ_k from the fit.

Fig. 4.6 needs to be modified to a depth-d circuit such that Λ is applied d times repeatedly, and circuits need to be constructed for each $d \in \boldsymbol{d}$. $F^d_{\lambda_k}$ is $\mathcal{F}_{\lambda_k}$ measured with the depth-d circuit. Based on the physical meaning of λ_k, it is easy to see that $F^d_{\lambda_k} = (\lambda_k)^d$. By fitting $F^d_{\lambda_k}$ to a single-exponential decay, λ_k can be extracted in a SPAM-free way since SPAM error does not affect the decay of the curve.

A useful application of EAB is to measure Pauli error in N-qubit Clifford gates. Clifford gates are elements of the Clifford group generated by the Hadmard gate (H), the phase gate $S = \sqrt{Z}$, and CNOT. One problem is that general gate noise is usually not a Pauli channel. Through Pauli twirling [78, 91], the general noise channel $\mathcal{E}$ associated with the noisy Clifford gate $\tilde{G}'$ can be projected into Pauli noise Λ. The Pauli projection of a quantum channel is a Pauli channel with the same diagonal elements as the original channel in its PTM and chi-matrix. Clifford gates have the property of mapping Pauli operators to Pauli operators through conjugation, which is utilized in randomized compiling. The qubits where the $\tilde{G}'$ acts are called data qubits. We also include N ancilla qubits. The noise is assumed to satisfy the gate-independent(single-qubit gates), time-invariant, and Markovian (GTM) assumptions, which are standard assumptions for benchmarking and reasonable for our experimental platform.

Under the GTM assumptions, a noisy implementation of the Clifford Gate $\tilde{G}'$ can be modeled as

$$\tilde{G}' = G \circ \mathcal{E}, \tag{4.13}$$

where G is the ideal Clifford gate and $\mathcal{E}$ is a general noise channel attached to G. Through Pauli twirling, $\mathcal{E}$ can be averaged into its Pauli projection Λ. The Pauli twirling process can be written as $\mathcal{E} \rightarrow \frac{1}{4^N}\sum_{P_i \in \mathbf{P}^N} P_i \mathcal{E} P_i$, where $\mathbf{P}^N$ is the N-qubit Pauli group. It is done by P_i randomly sampled from a uniform distribution of all elements in $\mathbf{P}^N$ on both sides of $\mathcal{E}$

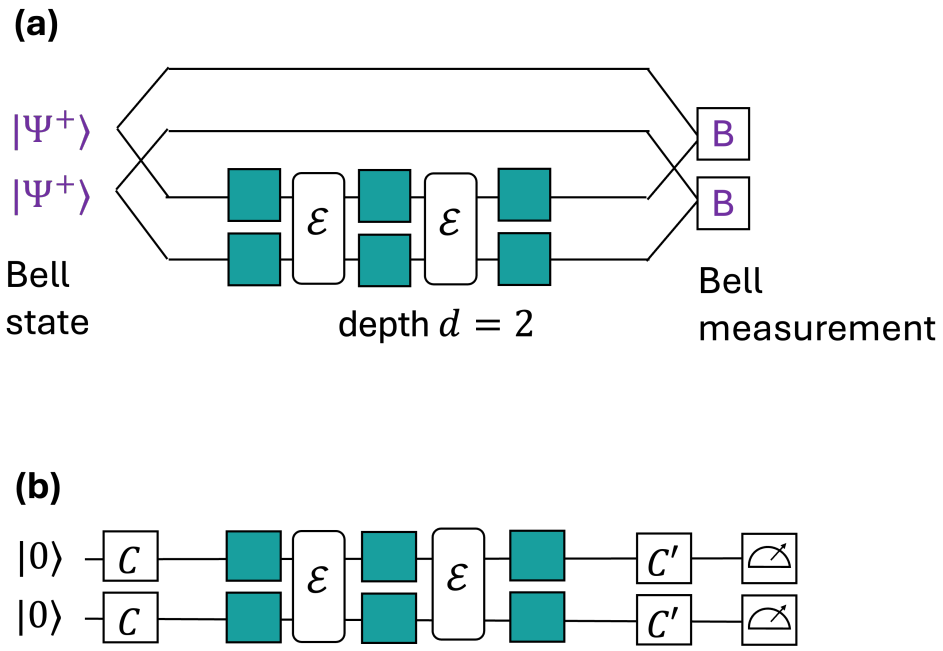

Figure 4.7: (a) Schematic of a depth-2 EAB circuit benchmarking a general quantum channel $\mathcal{E}$.The upper two qubits are ancilla and the lower two qubits are data qubits. $\mathcal{E}$ is repeated twice, interleaved with Pauli operators and I (teal squares) randomly drawn from a uniform distribution for twirling. (b) Schematic of a CB circuit of depth 2 benchmarking $\mathcal{E}$. C and C' are basis change operations for state preparation and measurements.

and averaging over many instances. After Pauli twirling, $\tilde{G}$ can be expressed as

$$\tilde{G} = G \circ \Lambda, \tag{4.14}$$

In the experiment, for each depth d, C circuits with different random twirling operators are sampled. Fig. 4.7 (a) shows an example EAB circuit of depth three.

4.2.3 Experimental Results

In order to experimental validate the EAB method, we use both EAB and the more established CB method to estimate the fidelity of our native two-qubit entangling gate. An example of the circuit is shown in Fig. 4.8. Other Parameters are chosen to be $C = 20$, $\boldsymbol{d} = [2, 8, 16, 32]$ for EAB, and $d = [2, 8, 32]$ for CB. The depth and circuit number per depth

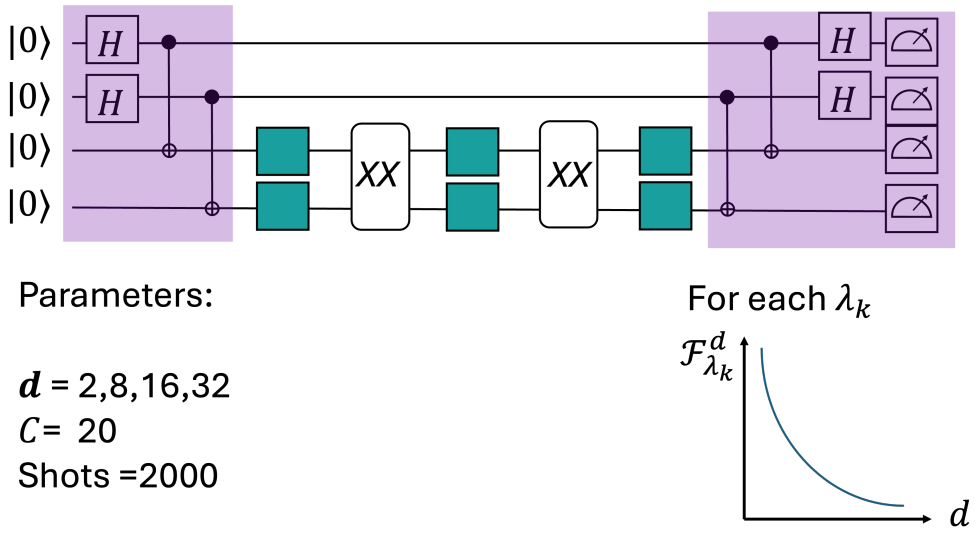

Figure 4.8: Schematic of a depth-2 EAB circuit benchmarking an XX gate. The sections highlighted in purple are for state preparation and measurements. The example circuit in the figure is for $d = 2$. In the full experiment to benchmark the XX gate, data were also taken for $d = 8, 16, 20$ with $C = 20$ circuits per depth. The bottom left shows the sketch of an exponential fit of $\mathcal{F}^d_{\lambda_k}$ with respect to d where λ_k can be extracted.

are determined by the estimated total error in the XX gate and the system size. The choice of these parameters are verified via statistical analysis of simulated and real data.

$F^d_{\lambda_k}$ with respect to depth d is plotted in Fig. 4.9, which shows good exponential behaviors, confirming that noise in our system complies with the GTM assumptions well.

There is a caveat that λ can only be characterized up to a fundamentally unlearnable degree of freedom[55]. Specifically, certain Pauli eigenvalues can not be learned exactly, and which Paulis are unlearnable is determined by the specific Clifford gate characterized. To see this, imagine we put Pauli operator XX on the data qubits right after the state preparation (purple box in Fig. 4.8) and evolve it with the circuit. The XX gate maps XX to itself, therefore the probability of XX being preserved at the end of the circuit averaging over random Pauli twirling is $\pm A_{XX}(\lambda_{XX})^2$, where A_{XX} depends on SPAM and will be removed by concatenation and curve fitting. The $\pm$ sign comes from Pauli twirling and can be corrected in post-processing. λ_{XX} can be learned exactly this way. However, if we put XZ right after the state preparation purple box, the case is entirely different. The XX

gate maps XZ to IY and vice versa. Therefore at the end of the circuit, XZ is preserved with probability $A_{XZ}\lambda_{XZ}\lambda_{IY}$. After concatenation and the curve fitting described in the previous section, we will actually obtain $\sqrt{\lambda_{XZ}\lambda_{IY}}$ instead of λ_{XZ}. The same applies to IY and we call $\{\lambda_{IY}, \lambda_{XZ}\}$ an unlearnable pair. For the XX gate, the other unlearnable pairs are $\{\lambda_{YI}, \lambda_{ZX}\}, \{\lambda_{IZ}, \lambda_{XY}\}$,and $\{\lambda_{ZI}, \lambda_{YX}\}$. The unlearnability arises from the fact that state preparation errors and measurement errors are not separately identifiable, introducing a gauge freedom. In the experiment, violations of the GTM criteria or imperfect Pauli twirling can cause Pauli fidelities of an unlearnable pair to be measured as different values. In order to mitigate the effect, in the following data analysis, their fidelities are symmetrized to be the mean square root of the product of the pair. For example, $\lambda_{IY} = \lambda_{XZ} = \sqrt{\lambda_{IY} * \lambda_{XZ}}$[25, 78, 119]. Symmetrized Pauli fidelities are presented in Figure 4.10.

Feasible regions

We learned from Eq. (4.12) that Pauli error rates can be inferred from the Pauli fidelities determined by EAB and CB. However, this inference is not natively constrained to valid (nonnegative) Pauli error rates. Inferred Pauli error rates can become negatives due to experimental error, violation of the GTM assumptions, and/or statistical fluctuations. Conditioning on Pauli error rates of all learnable Paulis to be positive, the values of unlearnable degrees of freedom in the system can be further constrained. Denote

$$\lambda_{YI} = 1 - x_1, \tag{4.15}$$

$$\lambda_{ZI} = 1 - x_2, \tag{4.16}$$

$$\lambda_{IY} = 1 - x_3, \tag{4.17}$$

$$\lambda_{IZ} = 1 - x_4, \tag{4.18}$$

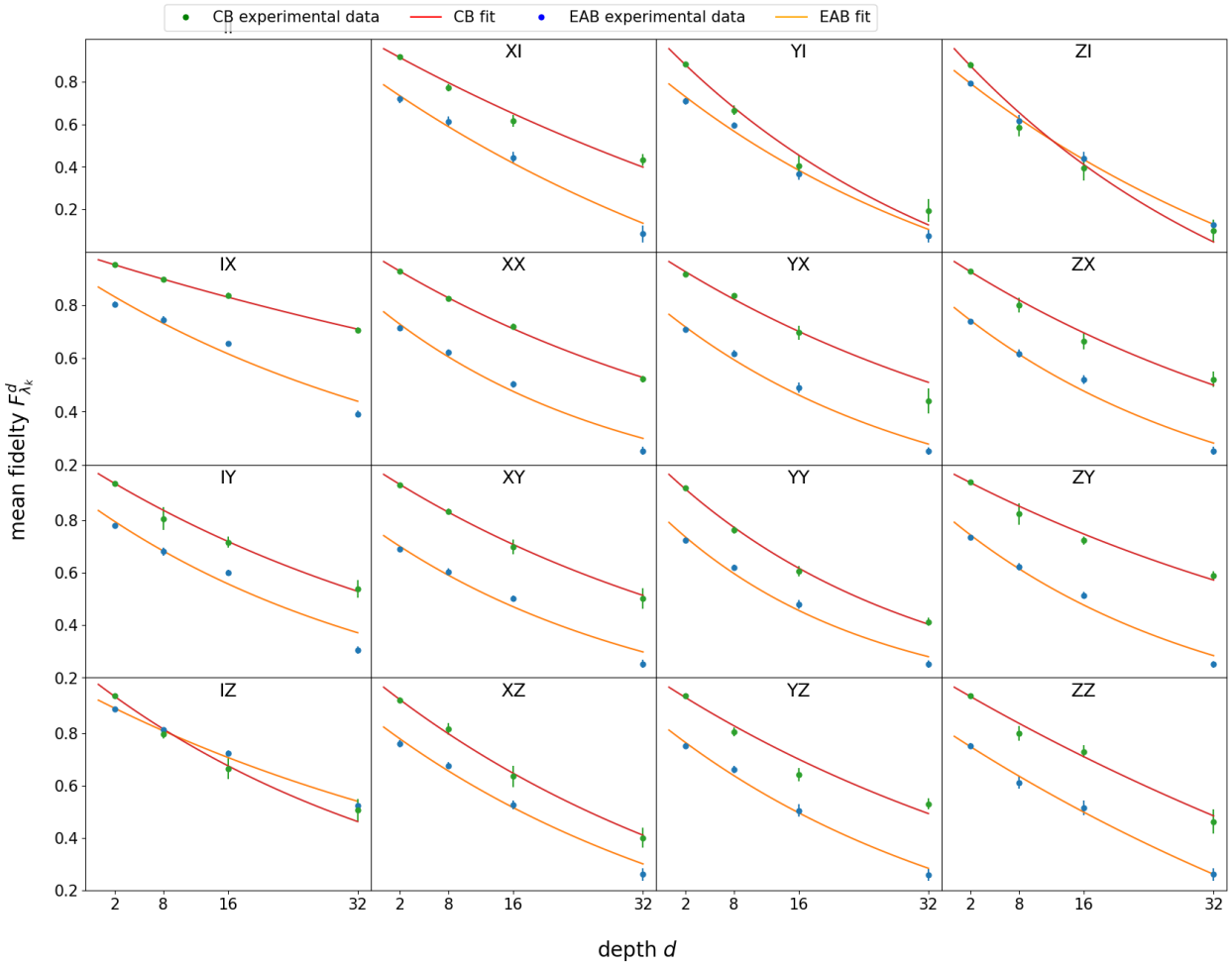

Figure 4.9: Exponential fits of $\mathcal{F}^d_{\lambda_k}(d)$ experimentally measured with EAB and CB for the two-qubit Pauli group. Each plot is for one element P_k from the two-qubit Pauli group. λ_k is the Pauli fidelity of P_k. The data points are $\mathcal{F}^d_{\lambda_k}$ measured experimentally at different depth d averaged over all $C = 20$ circuits. The blue points are from EAB and the green points are from CB. The error bars are generated from bootstrapping. The orange curves are exponential fits for EAB data, and the red curves are fits for CB data.

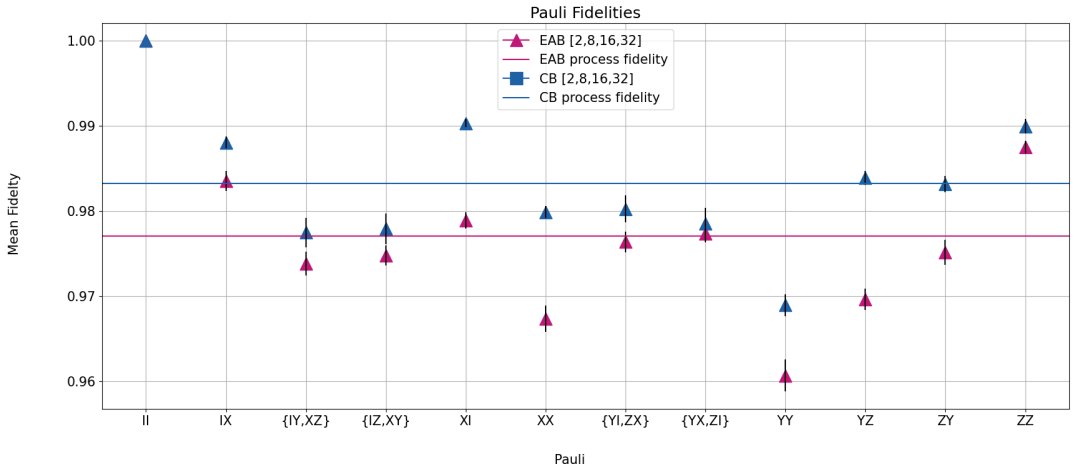

Figure 4.10: Symmetrized Pauli fidelities of Pauli noise in an XX gate measured with EAB (pink) and CB (blue). Pauli fidelities for non-degenerate pairs are symmetrized and plotted as one data point. The colored horizontal solid lines are the process fidelities of the XX gate estimated from the measured Pauli eigenvalues, which is 97.7% for EAB and 98.3% for CB. The error bars are from bootstrapping.

where $x_1, x_2, x_3, x_4 \in [0, 1]$.Then we have

$$\lambda_{ZX} = \lambda_{YI}\lambda_{ZX} * (1 + x_1), \tag{4.19}$$

$$\lambda_{YX} = \lambda_{ZI}\lambda_{YX} * (1 + x_2), \tag{4.20}$$

$$\lambda_{XZ} = \lambda_{IY}\lambda_{XZ} * (1 + x_3), \tag{4.21}$$

$$\lambda_{XY} = \lambda_{IZ}\lambda_{XY} * (1 + x_4), \tag{4.22}$$

All unlearnable Pauli eigenvalues are parameterized by the four variables x_1, x_2, x_3, and x_4. The full set of Pauli error rates can be expressed as functions of these four variables (See Appendix B.1 for more details). Conditioning on all learnable Pauli error rates to be nonnegative, we search through the parameter space to find feasible values for x_1, x_2, x_3, and x_4 and therefore also find feasible regions for each unlearnable Pauli fidelity.

We reuse the experimental data presented in Fig. 4.10 for feasible region analysis. The Results of the analysis are shown in Fig. 4.11 and Fig. 4.12. Note that, for CB data, if we strictly impose the positivity constraint, there are no feasible values for unlearnable Pauli

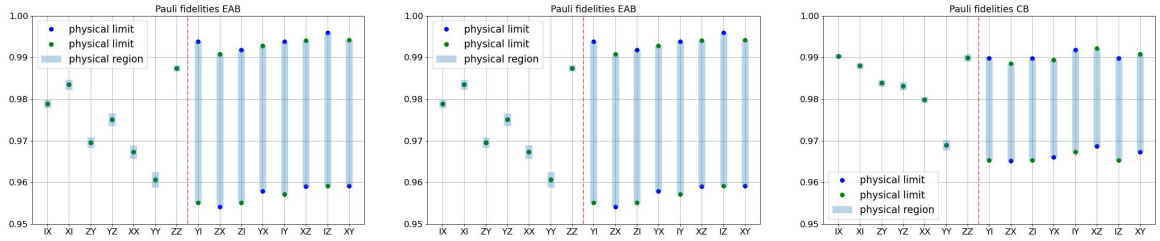

(a) EAB $p > -0.0005$ (b) EAB $p > 0$ (c) CB $p > -0.0005$

Figure 4.11: Light blue vertical lines show the feasible regions of all Pauli fidelites. All unlearnable Paulis are on the right hand side of the vertical dashed line. (a) Pauli fidelites measured with EAB conditioning on all unlearnable Pauli error rates to be greater than -0.0005.(b) Pauli fidelites measured with EAB conditioning on all unlearnable Pauli error rates to be greater than 0. (c) Pauli fidelites measured with CB conditioning on all unlearnable Pauli error rates to be greater than -0.0005.

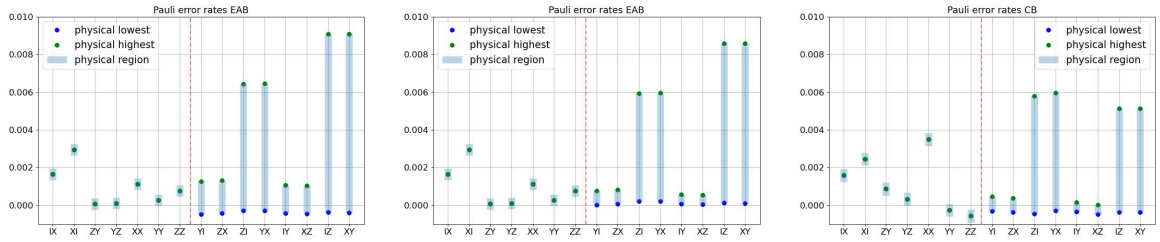

(a) EAB $p > -0.0005$ (b) EAB $p > 0$ (c) CB $p > -0.0005$

Figure 4.12: Light blue vertical lines show the feasible regions of all Pauli error rates. All unlearnable Paulis are on the right hand side of the vertical dashed line. (a) Pauli error rates measured with EAB conditioning on all unlearnable Pauli error rates to be greater than -0.0005.(b) Pauli error rates measured with EAB conditioning on all unlearnable Pauli error rates to be greater than 0. (c) Pauli error rates measured with CB conditioning on all unlearnable Pauli error rates to be greater than 0.

fidelities. Learnable Pauli error rates can be measured as negative due to system fluctuations as well. We can estimate the amount of this type of fluctuation by looking at the most negative learnable Puali error rate measured, which in this case is $p_{ZZ} = -0.0005$. It is reasonable to relax the constraint to require Pauli error rates larger than -0.0005 instead.

Discrepancy between CB and EAB results

In Fig.4.10, there is a discrepancy of about 0.5% in process fidelity between EAB and CB. Differences in individual Pauli fidelities can be even more. Although the discrepancy is small,

multiple repetition of experiments consistently shows that fidelities reported by CB are higher than that from EAB by a small margin. This could be caused by different constructions of the two protocols. The rest of the chapter explores the possible causes of this discrepancy.

The main difference between EAB and CB protocol is the ancilla system in EAB. We consider the following scenarios when ancilla can contribute to additional errors:

- data-ancilla crosstalk
- idle error

Data-ancilla crosstalk

Light in the individual addressing beam spilling over to neighboring ions can introduce optical crosstalk between the data and ancilla qubits. In the experiment, each ion is illuminated by a tightly focused laser beam. Due to the finite beam width and optical aberrations, the neighbor ions also see a small fraction of this beam, resulting in an unintended quantum operation. The magnitude of the crosstalk error scales with the intensity of the laser beam and the duration of the operation. Two-qubit entangling gates have much longer durations and higher optical power than single-qubit gates. Therefore we mostly considered crosstalk error during two qubit gates. Optical crosstalk can cause data and ancilla qubits to become entangled during XX gates, allowing correlation to build up between them which increases non-Markovianity in the data qubit system. This type of crosstalk error can be effectively eliminated when the system qubits and ancilla qubits are separated in space. To investigate whether system-ancilla crosstalk error contributes to the discrepancy between EAB and CB results, we implement two EAB experiments benchmarking an XX gate. In the first experiment, the two ions used as data qubits are directly next to the two ions used an ancilla qubits in the ion chain (Fig. 4.13 (a) configuration 2). In the other experiment, an idle dark ion is inserted in between data and ancilla ions (Fig. 4.13 (a) configuration 1). A comparison of the results is shown in Fig. 4.13 (b). The EAB results with the two different configurations are not meaningfully different, indicating that data-ancilla optical crosstalk is negligible in

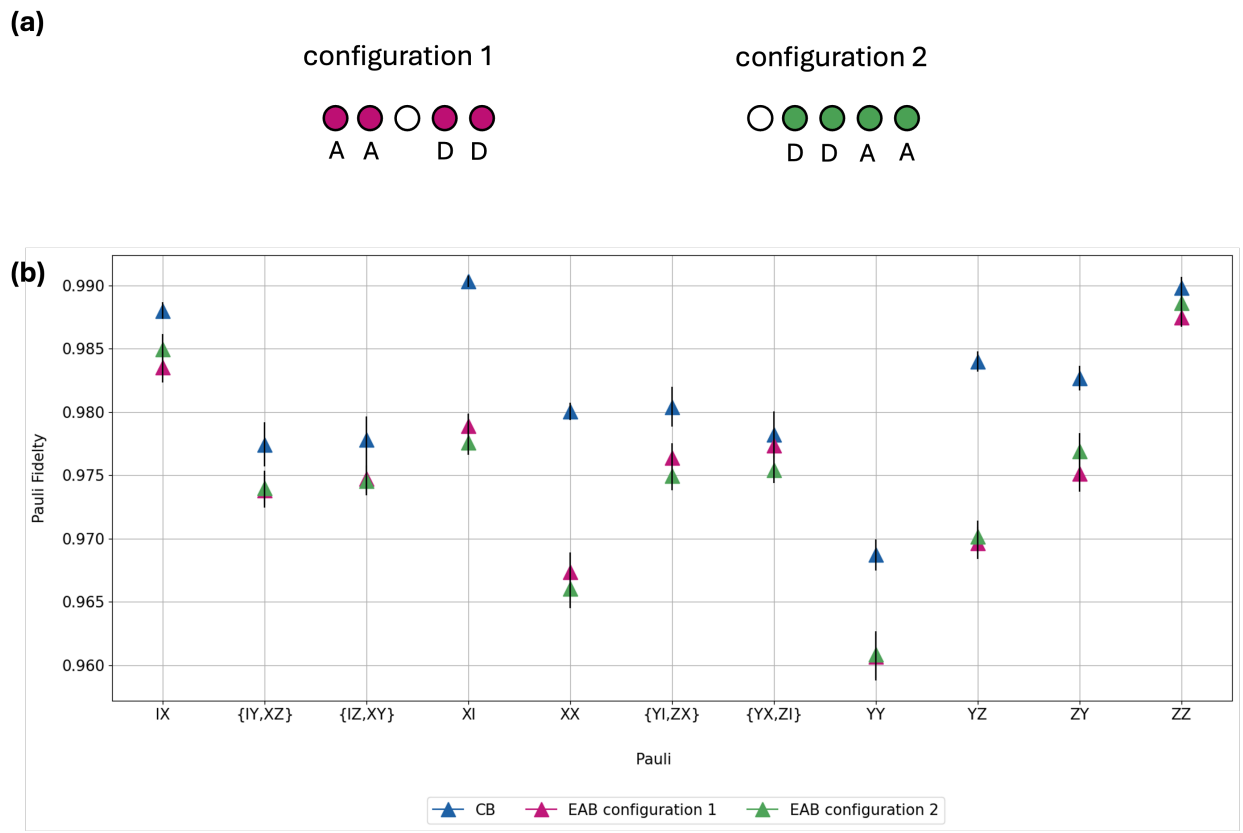

Figure 4.13: (a) Two configurations of data and ancilla qubits in an ion chain. Both open and colored circles represent ion qubits. "A" labels ancilla qubits and "D" labels data qubits. In configuration 1, one idle ion is inserted between data qubits and ancilla qubits. In configuration 2, data qubits directly neighbor ancilla qubits, in which case optical crosstalk between data and ancilla qubits should be strongly suppressed. (b) Experimental EAB results with configuration 1 (pink triangles) and configuration 2 (green triangles) compared with CB (blue triangles). Error bars are from bootstrapping.

these experiments even when the system and ancilla qubits are directly next to each other.

Ancilla idle error

In EAB, ancilla qubits are idle the entire time except for during the state preparation and measurement at the very beginning and very end of the circuit, and ancilla are assumed to be error-free. However in experiments, when no operation is being applied, qubits accumulate idle errors. When the depth d is large, large idle errors can build up. Ancilla error will be interpreted as a part of the Pauli noise on data qubits in EAB. The idle error is biased towards phase error originating from beam path fluctuations in our system. Dynamical

Decoupling (DD) is a common method for mitigating correlated errors in qubit systems[240, 243–245]. We implement different types of DD protocols on ancilla qubits in EAB circuits attempting to reduce ancilla error. All DD-EAB experiments in fact produce results much worse than EAB without DD. DD protocols rely on errors that occurred at different times to cancel out because of their temporal correlations. When uncorrelated error dominants, the error suppressed by DD is much smaller than the gate error introduced by DD pulses. This is also verified in a separate measurement while DD is applied to the qubit during a Ramsey experiment, qubit coherence time decreases as the interval between DD pulses decreases which is the effect of increased DD pulse error. Although Z rotation gates are error free, since idle error is dominately Z error as well, we can not only use Z rotations in DD. See B.2 for more details.

In experimental paper [220], DD was used to enhance the performance of EAB on superconducting qubits. Again we are witnessing the different noise structures between quantum computing platforms with different underlying technologies.

4.2.4 Noiseless EAB

Ancilla error affects EAB performance. Since uncorrelated errors dominate in our system, DD does not help. From now on, we refer to the EAB combined with concatenation as **noisy EAB** and the Pauli fidelities and Pauli error rates measured this way as noisy EAB results. In order to improve EAB performance, we design a protocol to extract noiseless EAB results, Pauli fidelities and Pauli error rates that are ancilla error-free, from noisy EAB results. We call this protocol **noiseless EAB**. This is realized by twirling and measuring ancilla noise separately and using this information to error-mitigate noisy EAB data in post-processing. A similar protocol is also implemented in Reference [220] on superconducting qubits using a different method for ancilla error measurement.

The noiseless EAB protocol consists of two noisy EAB experiments modified by adding Pauli twirling on the ancilla qubits (Fig. 4.14). The general noise on ancilla are projected to

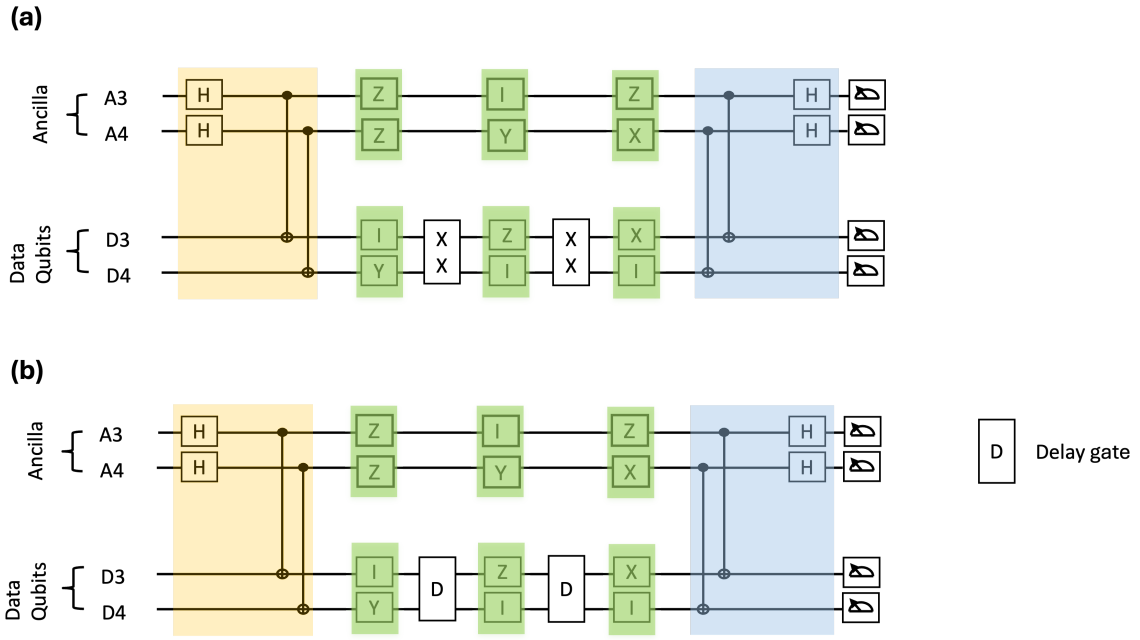

Figure 4.14: (a) Depth-2 circuits for noisy EAB with ancilla twirling. XX gates are implemented on data qubits and Pauli twirling on both data and ancilla qubits. (b) Depth-2 EAB circuit for ancilla error measurement, where XX gates on the data qubits are replaced by a delay of the same duration. Pauli twirling is applied to both data and ancilla qubits. Both data and ancilla qubits experience the same noise under the assumption that trapped-ion qubits are identical.

Pauli noise.

In the first noisy EAB with ancilla twirling experiment, a noisy Clifford is benchmarked. Fig. 4.14(a) shows an example circuit of $d = 2$, and the Clifford gate is XX in this example. This experiment is designed to produce noisy EAB results with Pauli twirled ancilla errors. Converting general noise on the ancilla to Pauli noise allows us to write EAB results of this experiment as a simple expression of ancilla noise and XX gate noise. Let Λ_{anc} denote the ancilla noise after twirling, and Λ denote the XX gate noise after twirling. λ'_k and λ_k are Pauli eigenvalues for Λ_{anc} and Λ respectively. Given that Λ_{anc} and Λ are uncorrelated, the composite channel acting on both the system and ancilla can be written as the tensor product of the two $\Lambda_{comp} = \Lambda_{anc} \circ \Lambda$. When Λ_{comp} acts on the the combined system of ancilla and data qubits initialized into Bell pairs

$$\Lambda(|\Psi^+\rangle \langle\Psi^+|)^{\otimes N} = (\Lambda_{anc} \circ \Lambda)(|\Psi^+\rangle \langle\Psi^+|)^{\otimes N} = \sum_k \lambda_k \lambda'_k P_k \otimes P_k^T / 4^N, \tag{4.23}$$

where P_k^T is P_k transpose. Eq. (4.23) shows that the measured Pauli fidelity of P_k from this experiment is actually $\lambda'_k \lambda_k$. Noiseless results λ_k of Λ can be extracted if λ'_k can be separately measured.

The second noisy EAB with ancilla twirling experiment measures λ'_k. An example of the circuit for $d = 2$ is shown in Fig 4.14 (b). Instead of XX gates, the delay gate, during which no operation occurs, is benchmarked. Each delay gate is set to be the same duration as the XX gate in Fig 4.14 (a). In this case, the ancilla qubits and the system qubits are essentially under the influence of the same noises. This is valid since trapped-ion qubits are identical to a good approximation. We have $\Lambda_{anc} = \Lambda$ and $\lambda_k = \lambda'_k$. The Pauli fidelities measured from this experiment can be written as $(\lambda'_k)^2$. λ'_k can be extracted by taking the square root. Combining these two experiments, λ_k can be calculated by scaling $\lambda'_k \lambda_k$ with λ'_k.

Experimental results for λ_k are shown in Fig.4.15. For comparison, CB, noisy EAB, and noisy EAB with ancilla twirling results are also shown. Noiseless EAB results (pink x symbol) show improvement from noisy EAB (cyan triangles) and higher agreement with CB. The

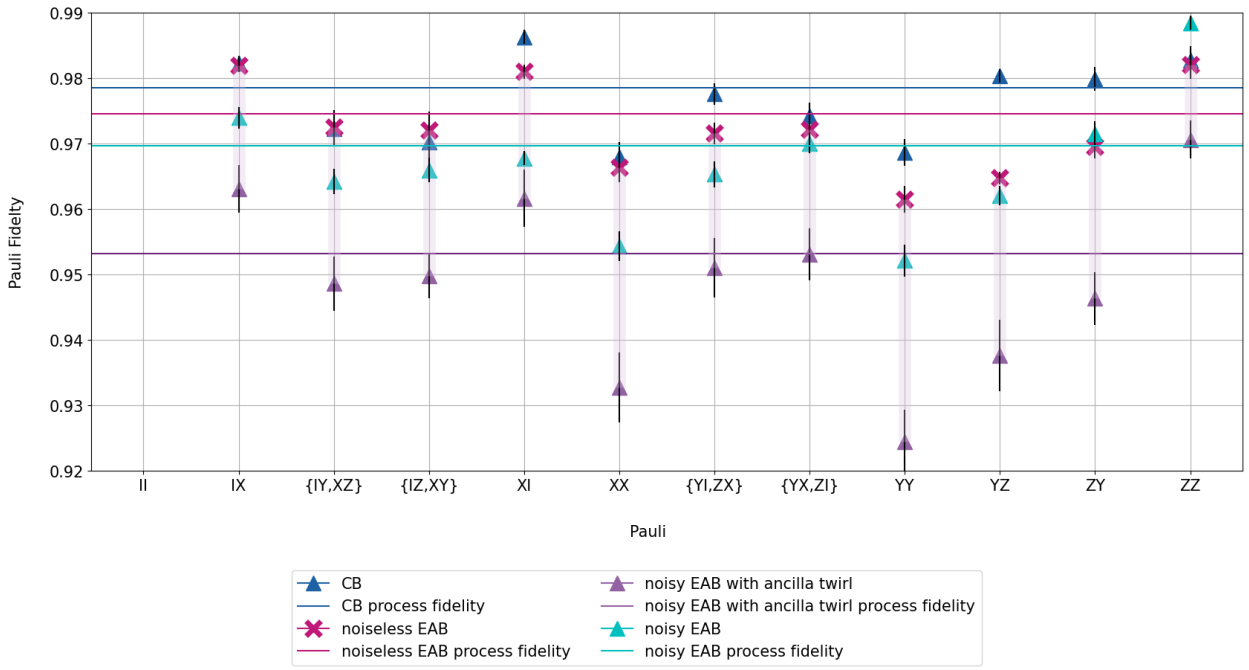

Figure 4.15: Eperimental results for symmetrized Pauli fidelities of Pauli noise in the XX gate. Pauli fidelities of the non-degenerate pairs are symmetrized and plotted as one entry. Results from CB are plotted in dark blue triangles, noisy EAB in cyan triangles, noiseless EAB in pink crosses, and EAB with ancilla twirling in purple triangles. Solid horizontal lines are the process fidelities calculated from the measured Pauli fidelities. The error bars are from bootstrapping and error propagation.

agreement is especially good for the left side of the plot ($\{IX, IY, XZ, IZ, XY, XI, XX\}$).

4.2.5 Summary and Outlook

We verified that noisy EAB combined with concatenation can benchmark Pauli noise in Clifford gates in a SPAM-robust way with computational resources and a number of ancillae that both scale linearly with the system size. We designed a protocol to improve noisy EAB results by measuring and mitigating the effect of ancilla error. The noiseless EAB result is close to that of CB. The modified protocol still scales linearly with system size when an ancilla register of the system size is available. We also note that, unlike superconducting qubits, dynamical decoupling does not suppress ancilla noise in our system effectively since DD pulse error is much bigger than the correlated ancilla error.

Due to the long experimental duration, the drift in the system can affect results. The new calibration method proposed in [220] may significantly reduce experiment time if concatenation is no longer needed for SPAM robustness. Another way to carry out a fairer comparison is to randomize the data-taking order of all circuits which will even out the effect of experimental drift in each data set.

Chapter 5

Parallel Gates on Orthogonal Motional Modes in a Trapped-Ion Chain

Parallel operations are important for both near-term quantum computers and larger-scale fault-tolerant machines because they reduce execution time and qubit idling. We propose and implement a pairwise-parallel gate scheme on a TIQC. The gates are driven simultaneously on different sets of orthogonal motional modes of a trapped-ion chain. We demonstrate the utility of this scheme by creating a GHZ state in one step using parallel gates with one overlapping qubit. We also show its advantage for circuits by implementing a digital quantum simulation of the dynamics of an interacting spin system, the transverse-field Ising model. This method effectively extends the available gate depth by up to two times with no overhead when no overlapping qubit is involved, apart from additional initial cooling. This scheme can be easily applied to different trapped-ion qubits and gate schemes, broadly enhancing the capabilities of trapped-ion quantum computers.

5.1 Introduction

In all trapped-ion entangling gate schemes realized so far, parallel or sequential, only one set of motional modes is considered, corresponding to the direction of strongest overlap between

the driving field and a principle trap axis. However, the ion chain has multiple sets of independent motional modes along orthogonal directions in space as discussed in Sec. 2.1.2. The other sets of motional modes are usually ignored, or decoupled by a rotation of the trap principle axes. While used in a few analog quantum simulations [4, 100] and considered in cost estimation for error correction [235], this resource remains untapped for entangling gates and digital quantum circuits. In this work, we use an additional set of modes to implement two entangling gates on arbitrary pairs of ions in parallel, including cases where there is one overlapping ion between the two pairs, with Raman laser beams [69].

Since the two sets of modes are orthogonal, there is no need to calculate unique parallel gate pulses, as existing laser pulse designs for sequential implementation of entangling gates can simply be applied simultaneously. For addressing beam array with a fixed maximum power per beam, no extra laser power is required when there is no overlapping ion since idle energy in the laser beams is used. For overlapping pairs, this scheme may require twice the laser power of a single entangling gate on the shared ion, but typically less than that. The idea is directly applicable to any addressed entangling gate scheme that uses the ion motion [14, 21, 24, 58, 82, 87, 111, 112, 144, 164, 172, 219, 224, 230]. It can also be extended to the third motional direction.

Figure 5.1 shows the concept for running pairwise parallel gates. In the depicted setup, the ion chain is illuminated by an array of individual addressing beams and one counter-propagating global beam for driving coherent Raman transitions. The beam directions overlap with the two radial principle axes. We use the MS scheme as our two-qubit gates. Using different frequencies, one pair of beams drives an MS gate on the x-modes (shown in green), and another pair simultaneously does the same on another pair of ions on the y-modes (shown in purple). This protocol can be applied to addressed trapped-ion chains in any trap geometry, not limited to the one shown in Figure 5.1, provided that the driving field has non-zero projections along multiple principal axes. Other gate schemes can also be used, as noted in the introduction.

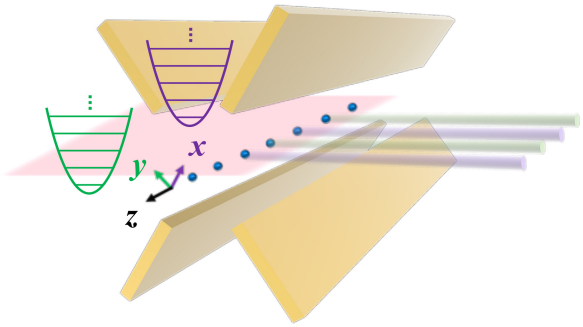

Figure 5.1: Experimental setup for parallel MS gates on orthogonal motional modes. A chain of ions is trapped in a linear Paul trap indicated by the four trap electrodes. The center five ions are used as qubits, numbered 1-5 from left to right. x, y, and z are the three principal axes of the trap. The harmonic oscillator modes along the x- and y-axis are shown in purple and green, respectively. Transitions are driven by a pair of Raman beams consisting of a global beam (pink) and a counter-propagating addressing beam array. The colors of the individual beams indicate different detunings, which excite motional modes along different principal axes. As an example, this figure shows an MS gate on qubits 1 and 3 via the x modes in parallel with an MS gate on qubits 2 and 4 via the y modes. Any gate pair can be parallelized this way.

Here we describe our experiment and protocol as an example. The laser beams used for coherent operations between qubit states are derived from a mode-locked laser and drive a Raman transition between the two qubit states. The beat-notes between the two beams are at $\omega_0 \pm \mu$, which are closely detuned from blue and red motional sidebands [69], where ω_0 is the carrier frequency. In order to disentangle the modes from the qubits at the end of the gate, modulation schemes for the amplitude, phase, and frequency of the laser pulse, respectively, or a combination of these are employed, leaving only the qubit states of the ion pair in entanglement [103, 166, 208, 223, 269]. We use amplitude modulation [56] for this demonstration, but any of the above schemes can equally be used. Our gate duration is 235 μs.

The unitary representing an MS gate on the qubit pair $\{p, q\}$ is $U = \exp\left(i\chi_{pq}\sigma_x^p\sigma_x^q\right)$, where σ_x^p is the Pauli-X operator acting on qubit p, and χ_{pq} is the gate angle which can be varied arbitrarily by applying a scale factor to the amplitude of laser pulse. A single MS gate via the y modes can be implemented in the same way with beat-notes of the counter-

propagating Raman beams tuned to $\omega_0 \pm \mu'$, close to the y modes. We simultaneously drive an MS gate on qubits $\{p, q\}$ via x modes and another on qubits $\{m, n\}$ via the y modes by applying the two gate pulses at the same time. In the example illustrated in Figure 5.1, $\{p, q\} = \{2, 4\}$ and $\{m, n\} = \{3, 5\}$.

We now show that these simultaneous operations do not introduce cross-couplings. In our experimental setup, the center-of-mass x and y modes are about 150 kHz apart, while the span of each set of motional modes is about 100 kHz. These two spacings are independent of the number of ions in the chain N. The average spacing within a set of modes is $\frac{100}{N-1}$kHz. For $N = 7$, the average spacing within a set of modes is about 17 kHz. When the gate is driven via the $x(y)$ modes, the closest $y(x)$ mode is 50 kHz away at worst, typically 100 kHz, which is large compared to the typical sideband Rabi frequency of 5 kHz. The shaped gate pulse also helps suppress excitation of the other set of modes because of its slow turn-on rate compared to a square pulse. Therefore, off-resonant driving of the other set of modes can be neglected. In the interaction picture and the Lamb-Dicke regime, neglecting the off-resonant carrier term, the Hamiltonian describing the interactions present during the parallel gate (PG) is

$$H_{\mathrm{PG}}(t) = H_x(t) + H_y(t), \tag{5.1}$$

where

$$H_x(t) = \sum_{i\in\{p,q\}} \sum_{k=1}^{N} \Omega_i(t)\eta_k^i \cos(\mu t - \phi_i)(a_k e^{-i\omega_k t} + h.c.)\sigma_x^i$$

and

$$H_y(t) = \sum_{j\in\{m,n\}} \sum_{k'=1}^{N} \Omega_j(t)\eta_{k'}^j \cos(\mu' t - \phi_j)(b_{k'} e^{-i\omega_{k'} t} + h.c.)\sigma_x^j.$$

N is the total number of ions in the chain. $\omega_k(\omega_{k'})$ is the frequency of the motional mode $k(k')$ in the $x(y)$-direction and $a_k^\dagger$ and $a_k(b_{k'}^\dagger$ and $b_{k'})$ are the creation and annihilation operator for mode $k(k')$ in the $x(y)$-direction. $\Omega_i(\Omega_j)$ is the Rabi frequency of qubit $i(j)$. $\eta_k^i(\eta_{k'}^j)$ is

the Lamb-Dicke parameter coupling qubit $i(j)$ to mode $k(k')$ in $x(y)$. $\phi_i(\phi_j)$ is determined by the laser phase.

In order to calculate the evolution unitary, we exponentiate Equation (5.1) using the Magnus expansion. Looking at the first two terms in the Magnus series, we have

$$U_{\mathrm{PG}}(\tau) = e^{-i\int_0^\tau dt H_{\mathrm{PG}}(t) - \frac{1}{2}\int_0^\tau dt_2 \int_0^{dt_2} dt_1 [H_{\mathrm{PG}}(t_2), H_{\mathrm{PG}}(t_1)]}, \tag{5.2}$$

where τ is the gate time. Expanding the commutator yields

$$\begin{aligned}[H_{\mathrm{PG}}(t_2), H_{\mathrm{PG}}(t_1)] =& [H_x(t_2), H_x(t_1)] + [H_y(t_2), H_y(t_1)] \\ &+ [H_x(t_2), H_y(t_1)] + [H_y(t_2), H_x(t_1)].\end{aligned} \tag{5.3}$$

Note that, σ_x^i commutes with σ_x^j, and since the x and y modes are orthogonal a_k and $a_k^\dagger$ commute with $b_{k'}$ and $b_{k'}^\dagger$. As a result, $[H_x(t_1), H_y(t_2)] = 0$ at any time as well as the last two terms in Equation (5.3), which are the cross-coupling terms between x and y. We emphasize that the scheme also applies to cases where the two qubit pairs share an ion since $[\sigma_x^i, \sigma_x^j] = 0$ includes the case of $i = j$. Either remaining term in Equation (5.3) contains motion in the x-direction only or the y-direction only. Same as the case of one MS gate, the dependence on motion eventually vanishes in Equation (5.3) due to the commutation relations between the motional operators. Therefore, the higher-order terms not shown in the Magnus expansion in Equation (5.2) are also zero. We can rewrite Equation (5.2) as

$$U_{\mathrm{PG}}(\tau) = \exp\left(\sum_{i\in\{p,q\}} (G_i \sigma_x^i) + i\chi_{pq}\sigma_x^p\sigma_x^q + \sum_{j\in\{m,n\}} (G'_j \sigma_x^j) + i\chi_{mn}\sigma_x^m\sigma_x^n \right), \tag{5.4}$$

where G_i is defined as

$$G_i = \sum_{k=1}^{N} \alpha_{i,k}(\tau) a_k^\dagger + \alpha_{i,k}^\star(\tau) a_k \tag{5.5}$$

$$\alpha_{i,k}(\tau) = -\int_0^\tau \eta_k^i \Omega_i(t) \cos(\mu t - \phi_i^m) e^{i\omega_k t} dt. \tag{5.6}$$

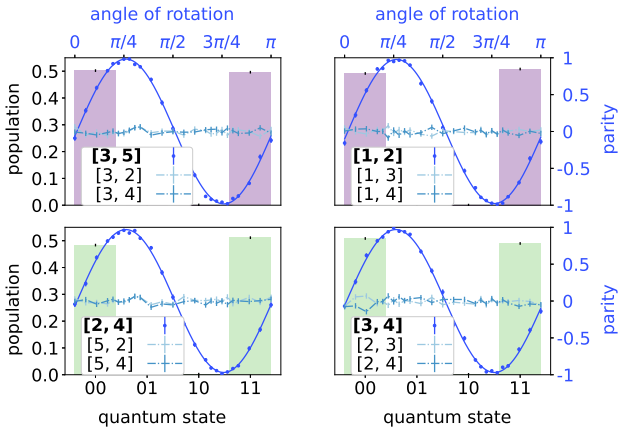

Figure 5.2: Fidelity measurements for two representative pairs of parallel MS gates on non-overlapping pairs of qubits in a seven-ion chain. The populations in the computational basis (left ordinate, bottom abscissa) and the parity scan (right ordinate, top abscissa) are plotted for each MS gate. The left column shows parallel pair {3,5} (purple) entangled via the x modes and pair {2,4} (green) entangled via the y modes. Dark blue solid curves are fitted to the parity scan data. The measured fidelities are $F_{35} = 99.1(4)\%$ and $F_{24} = 98.2(4)\%$. Parity measurements of the cross-pairs plotted in lighter blue colors in the background show no oscillation. The right column of the figure shows pair {1,2} (purple) entangled via the x modes and {3,4} (green) entangled via the y modes, where $F_{12} = 98.8(5)\%$ and $F_{34} = 98.4(4)\%$. All uncertainties are statistical.

The expression for G'_j is similar to Equation (5.5) except that the sum over x modes is replaced by a sum over y modes and μ is replaced by μ'. Since the first two terms in the exponential in Equation (5.4) only involve x modes while the last two terms only involve y modes, these two parts can be treated separately. The Rabi frequencies $\Omega_i(t)(i \in \{p, q\})$ are modulated such that $G_i(\tau) = 0$. The pulse modulation is done likewise for the qubit pair $\{m, n\}$ to set $G'_j(\tau) = 0$ $(j \in \{m, n\})$. The gate angles χ_{pq} and χ_{mn} can be set independently. Finally, the resulting unitary Equation (5.7) describes parallel MS gates on $\{q, p\}$ and $\{m, n\}$ with angle χ_{pq} and χ_{mn}, respectively:

$$U_{\mathrm{PG}}(\tau) = \exp(i\chi_{pq}\sigma_x^p\sigma_x^q + i\chi_{mn}\sigma_x^m\sigma_x^n) \tag{5.7}$$

.

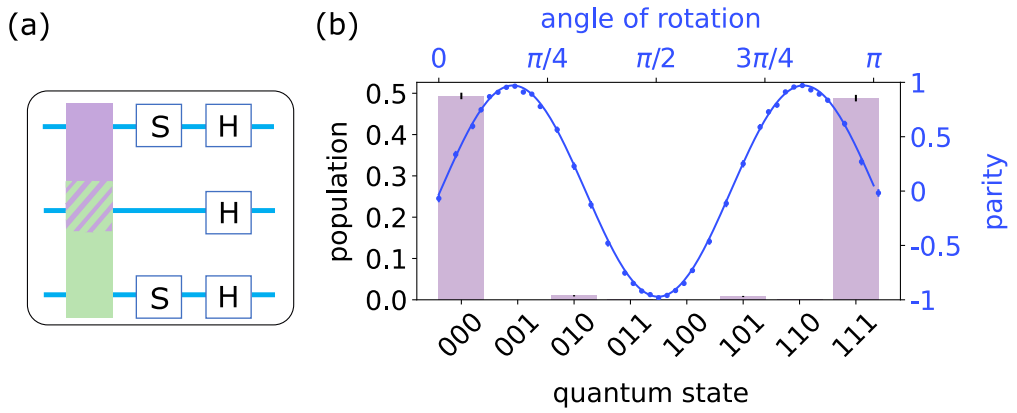

Figure 5.3: (a) Circuit for preparing a three-qubit GHZ state with parallel gates. All qubits are initiated in the $|0\rangle$ state. The first gate is a pair of parallel MS gates overlapping on the middle qubit. H is the Hadamard gate. The S gate is defined as $S = e^{-i\sigma_z \frac{\pi}{4}}$. (b) Parity contrast (top abscissa, right ordinate) and populations (bottom abscissa, left ordinate) of an experimentally prepared GHZ state on a seven-ion chain. The estimated fidelity is $F_{\mathrm{GHZ}} = 97.6(3)\%$. Error bars are statistical.

5.2 Experimental Results

Using a chain of seven ions, we experimentally demonstrate parallel MS gates on different qubit pairs, including the case where one qubit is shared between the two pairs. We then show their benefit for long circuits by running a digital quantum simulation of a paradigmatic spin model, the transverse field Ising model.

For two parallel MS gates of angle $\pi/4$ implemented on two non-overlapping pairs of qubits, we estimate the fidelity of each MS gate for the corresponding two-qubit density matrix, by measuring the even-parity state populations of the output state and the parity contrast [16, 212]. The parity contrast is extracted by appending single-qubit $\pi/2$ rotations to the MS gate and varying their phases. The results are shown in **Figure 5.2**. SPAM errors are removed by applying the inverse of a separately measured SPAM matrix to the experimental data. We find that the fidelity of our parallel gates is overall very similar to that of our sequential gates (see **Table 5.1**). We also probe the cross-talk error by estimating the degree of entanglement of the cross-pairs that are not supposed to be entangled. This could occur due to optical cross-talk or motional cross-talk. Parity measurements plotted in gray scale

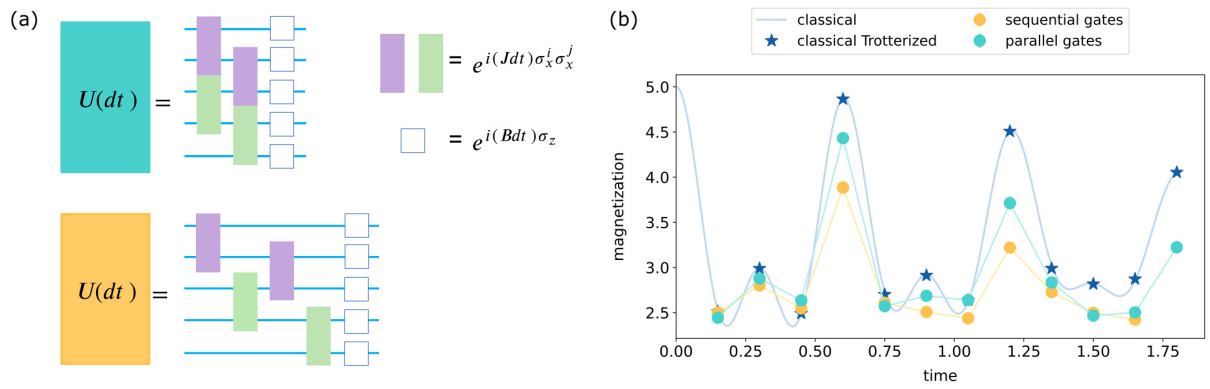

Figure 5.4: (a) TFIM circuits of one Trotter step with parallel gates (top) and sequential gates (bottom), using the x modes (purple) and y modes (green). (b) TFIM experimental results, where $\frac{B}{J} = 0.096$. The total magnetization m of the spin chain in the z direction is evaluated at different evolution times. The evolution with parallel MS gates shows a much higher contrast than the evolution with sequential gates. The error bars on the experimental points are statistical and are smaller than the marker.

in Figure 5.2 show no oscillation within errors, which indicates no unwanted entanglement between the cross-pairs. Cross-talk can also result in residual motional entanglement, which manifests in the population of the odd parity states (01 and 10) after an XX gate. The combined population of the two odd-parity states is less than 0.006 for all four gates shown in Figure 5.2. These observations indicate that no additional error, such as motional cross-talk between the two sets of radial modes due to trap non-linearities, is caused by the parallel operation. Yet, the reduction in execution time will improve the fidelity of a complete circuit implementation with parallel gates.

Table 5.1: The table compares parallel gate (PG) fidelities to sequential gate fidelities.

Pair	PG	Sequential
XX35	99.1(4)%	99.1(3)%
XX24	98.2(4)%	99.2(4)%
XX12	98.8(5)%	97.5(4)%
XX34	98.4(4)%	99.2(4)%

5.2.1 Three-Qubit Entanglement

We use our scheme to entangle three ions in one step, generating a three-qubit GHZ state. The circuit is shown in **Figure 5.3(a)**. It consists of a three-qubit entangling gate followed by $\pi/2$ phases gates and Hadamard gates.

Figure 5.3(b) shows the populations and parity contrast of the GHZ state prepared with parallel MS gates on qubits $\{3, 5\}$ and $\{2, 5\}$. We estimate the fidelity using parity contrast and even-parity state populations again to find $F_{\mathrm{GHZ}} = 97.6(3)\%$, which is as good as the three-qubit GHZ of 97.1(1)% fidelity prepared on the same system with sequential MS gates and improves upon the three-qubit GHZ state prepared with global parallel gates reported on another trapped ion experiment [172]. The laser pulses for both MS gates are summed up in the software and applied simultaneously to the overlapping ion. In the worst-case scenario, this will require the sum of two gate powers to implement them in parallel. However, it can often be done with less power because the gate pulse segments with the highest amount of power in the two gate pulse shapes do not always overlap.

5.2.2 Transverse Field Ising Model with Parallel Gates

Quantum spin models can describe a wide range of quantum many-body dynamics and are suitable for implementation on different hardware platforms [146, 217]. They can be used to study a variety of classically intractable problems in condensed matter physics, such as quantum magnetism [211], spin glasses [27], and others [184]. We demonstrate the experimental advantage of our parallel gate scheme over sequential gates by digitally simulating the dynamics of 1D Transverse Field Ising Model (TFIM) of five spins with nearest-neighbor interactions. The Hamiltonian can be written as

$$H = -J \sum_{i=1}^{4} \sigma_x^i \sigma_x^{i+1} - B \sum_{i=1}^{5} \sigma_z^i, \tag{5.8}$$

where J and B characterize the strength of interaction between the neighboring spins and the magnitude of the external field, respectively. The spin $|\uparrow\rangle$ ($|\downarrow\rangle$) state is mapped to the qubit $|+\rangle(|-\rangle)$ state. All qubits are initialized in the $|0\rangle = \frac{1}{\sqrt{2}}(|\uparrow\rangle + |\downarrow\rangle)$ state. The time-evolution unitary is Trotterized and decomposed into gates [170, 233]. Circuits representing one Trotter step are shown in **Figure 5.4 (a)**. Both circuits consist of MS gates, applied in sequence or in parallel, and single-qubit z-rotations. After N Trotter steps, the qubits are measured in the z basis, and the total magnetization along z, $m = \sum_{i=1}^{5} \sigma_z^i$, is calculated. Since the single-qubit z-rotations are done as instantaneous classical phase advances on the controller, the circuit execution time with sequential MS gates is twice as long as that with parallel MS gates.

The results are plotted in **Figure 5.4 (b)**. In the experiment, the sequential gates are also done on both x and y motional modes, consistent with the parallel gates, to ensure a fair comparison. The same MS gate pulse is used for each qubit pair in both the parallel implementation and the sequential implementation. For points of high-magnetization, for which the observable is most sensitive to errors, we see a reduction in error by up to a factor of two in the parallel gate implementation as a consequence of halving the circuit run time using parallel gates. This demonstrates that there is an advantage in using parallel gates, even for shorter circuits.

5.3 Conclusion and Outlook

While employing these pairwise-parallel gates in an ion trap quantum computer does not reduce algorithm complexity, it can shorten the circuit execution time by up to a factor of 2 and, therefore, increase the fidelity for gate sequences (see Figure 5.4). The only cost is a fixed overhead for ground-state cooling the additional set of modes, which is already cooled to below the Doppler limit by the high-intensity laser sideband cooling of the first set of modes. There is no calibration overhead in the parallel implementation. In fact, the required number

of calibrations is usually reduced as gates can be calibrated in parallel. In the worst case, where a gate for each qubit pair needs to be calibrated with both sets of modes, the number of calibrations is the same as in the sequential case. Therefore this parallel gate scheme should be used whenever possible. Our scheme is advantageous compared to aligning the Raman beams with one motional direction only because it is faster for a given beam power, as the duration of pulse-shaped gate pulse sequences for decoupling multiple modes does not scale linearly with power.

This parallel gate is easily transferable to other linear trap geometries. It can be generalized to any MS gate pulse modulation and addressing schemes, provided that the controllers can target multiple ions in space and multiple modes in frequency. It could also be extended to the axial direction and be combined with other parallel gate schemes that use motional modes only along one principal axis [87, 111, 172] to further increase the maximum number of simultaneous two-qubit gates. Finally, other entangling gate mechanisms, such as light shift gates [14, 164], those driven by a synthetic σ_z spin-dependent force [21], the multi-qubit gate based on the Cirac-Zoller scheme with ancillary motional states [82], and gates based on mode squeezing via second-sideband driving [144, 224] can be pairwise-parallelized in the same way.

Appendix A

QAOA circuits, parameters, and statistical tests

A.1 Circuits and parameters

Variational parameters α and β for the three-qubit and four-qubit Grover mixer for each problem are listed in Table A.1. These optimal parameter sets are derived from a noise-free theory using exact numerics. For the edge-cover problems, we perform a global grid search for the parameters starting with a resolution of 0.1 and keep refining the best results via a local grid search with successively finer resolutions until we reach the desired resolution, which is set to 0.01 for most problems and 0.1 for $p = 3$ paw graph with the simple mixer. For the Max-Cut problem, we use the *FindMinimum* function in *Mathematica* [133] and pick the best result out of at least 10 independent searches.

A.2 Statistical tests for fair sampling

The "shots to reject" test used in Sec. 3.1.4 is based on the one-tailed χ^2 test. To find N^*, we implement the following steps: 1) randomly draw 1000 sets of samples of size M (starting from $M = 2$) from Q_1, perform a χ^2 test between each sampled distribution and Q_2, and

	$p=1$	$p=2$	$p=3$
triangle	$\alpha=-0.95$, $\beta=1.00$	$\alpha_1=-0.83$, $\beta_1=3.14$ $\alpha_2=0.85$, $\beta_2=-1.66$	
square	$\alpha=-0.87$, $\beta=-2.60$	$\alpha_1=0.80$, $\beta_1=-1.58$ $\alpha_2=-0.82$, $\beta_2=-2.28$	
paw	$\alpha=1.04$, $\beta=-0.61$	$\alpha_1=0.62$, $\beta_1=0.75$ $\alpha_2=0.88$, $\beta_2=-1.04$	$\alpha_1=0.5$, $\beta_1=1.6$ $\alpha_2=-0.5$, $\beta_2=0.5$ $\alpha_3=-0.5$, $\beta_3=0.3$
bridge	$\alpha=0.29$, $\beta=0.31$	$\alpha_1=-0.55$, $\beta_1=0.42$ $\alpha_2=-2.95$, $\beta_2=0.87$	$\alpha_1=-2.09$, $\beta_1=0.43$ $\alpha_2=-2.17$, $\beta_2=1.28$ $\alpha_3=-1.02$, $\beta_3=2.3$

(a) Standard QAOA parameters corresponding to results in Fig. 3.1 and Table 3.1 (left)

	$p=1$	$p=2$
triangle	$\alpha=2.48$, $\beta=1.37$	$\alpha_1=0.69$, $\beta_1=1.32$ $\alpha_2=1.22$, $\beta_2=0.92$
square	$\alpha=0.65$, $\beta=1.46$	$\alpha_1=0.48$, $\beta_1=1.52$ $\alpha_2=0.91$, $\beta_2=0.92$
paw	$\alpha=0.79$, $\beta=1.60$	$\alpha_1=0.56$, $\beta_1=1.47$ $\alpha_2=0.98$, $\beta_2=1.17$

(b) G-QAOA parameters for unweighted problems corresponding to results in Fig. 3.4 and Table 3.1 (right)

	$p=1$	$p=2$
square	$\alpha=2.67$, $\beta=-2.30$	$\alpha_1=0.68$, $\beta_1=2.20$ $\alpha_2=1.05$, $\beta_2=1.95$
paw	$\alpha=-2.85$, $\beta=2.81$	$\alpha_1=2.05$, $\beta_1=2.80$ $\alpha_2=1.98$, $\beta_2=2.98$

(c) G-QAOA parameters for weighted problems corresponding to results in Fig. 3.5

Table A.1: Standard QAOA and G-QAOA parameters.

record the 1000 p-values from the tests, 2) compare the median of the p-values with the preset significance level, which is chosen to be 0.05 here, 3) if the median of the p-values exceeds the threshold, set $M := 2M$ and repeat steps 1 to 2; otherwise, if the median p-value is smaller than the threshold, H_0 is rejected, then a bisection method is used to locate the exact N^* between M and $M/2$.

The KL divergence used in Sec. 3.1.4 is defined as

$$D_{KL}(Q_1||Q_2) = \sum_{x \in X} Q_1(x) \frac{Q_1(x)}{Q_2(x)}, \tag{A.1}$$

where X is the sample space. It can be intuitively understood as the information loss when we model Q_2 by Q_1, providing the distance between the two distributions. The results for this analysis in Sec. 3.1.4 are presented in Table A.2.

		$p = 1$	$p = 2$
unweighted	triangle	0.0007(4)	0.007(2)
	paw	0.015(2)	0.016(2)
	square	0.007(1)	0.020(2)
weighted	paw	0.079(8)	0.037(4)
	square	0.089(9)	0.074(6)

(a) Experimental data

		$p = 1$	$p = 2$
unweighted	triangle	0.0004(2)	0.0003(1)
	paw	0.0006(3)	0.0005(2)
	square	0.0008(3)	0.0007(3)
weighted	paw	0.004(2)	0.0005(2)
	square	0.0021(8)	0.0009(3)

(b) Synthetic data

Table A.2: KL divergence between the simulation and experimental data, and synthetic data. The error bar on each experimental result is calculated by resampling from the experimental distribution 300 times, while for each synthetic result it comes from 300 sets of synthetic data generated for each problem.

Appendix B

EAB

B.1 Parameterized Pauli error rates for feasible region analysis

All unlearnable Pauli eigenvalues are parameterized by the four variables x_1, x_2, x_3, and x_4 as discuss in Sec. 4.2.3 The full set of Pauli error rates can be expressed as functions of these four variables through the Walsh-Hadamard transform. Parameterized Pauli error rates can be written as

$p_{II} = -0.00323131078016112 * x_1 - 0.0031183479343113 * x_2 - 0.00292197085083963 * x_3 - 0.00279764468654777 * x_4 + 0.976843559555855,$

$p_{XI} = 0.00323131078016112 * x_1 + 0.0031183479343113 * x_2 - 0.00292197085083963 * x_3 - 0.00279764468654777 * x_4 + 0.0029330375679675,$

$p_{YI} = -0.121768689219839 * x_1 + 0.121881652065689 * x_2 - 0.12207802914916 * x_3 - 0.122202355313452 * x_4 + 0.00625399002377206,$

$p_{ZI} = 0.121768689219839 * x_1 - 0.121881652065689 * x_2 - 0.12207802914916 * x_3 - 0.122202355313452 * x_4 + 0.00869235853402681,$

$p_{IX} = -0.00323131078016112 * x_1 - 0.0031183479343113 * x_2 + 0.00292197085083963 * x_3 + 0.00279764468654777 * x_4 + 0.00167295121379744,$

$p_{XX} = 0.00323131078016112 * x_1 + 0.0031183479343113 * x_2 + 0.00292197085083963 * x_3 + 0.00279764468654777 * x_4 + 0.000982108059574938,$

$p_{YX} = -0.121768689219839 * x_1 + 0.121881652065689 * x_2 + 0.12207802914916 * x_3 + 0.122202355313452 * x_4 - 0.00252094684904836,$

$p_{ZX} = 0.121768689219839 * x_1 - 0.121881652065689 * x_2 + 0.12207802914916 * x_3 + 0.122202355313452 * x_4 - 0.00541116674270239,$

$p_{IY} = -0.121768689219839 * x_1 - 0.121881652065689 * x_2 - 0.12207802914916 * x_3 + 0.122202355313452 * x_4 + 0.00678395750152917,$

$p_{XY} = 0.121768689219839 * x_1 + 0.121881652065689 * x_2 - 0.12207802914916 * x_3 + 0.122202355313452 * x_4 - 0.0018743139126293,$

$p_{YY} = -0.00323131078016112 * x_1 + 0.0031183479343113 * x_2 - 0.00292197085083963 * x_3 + 0.00279764468654777 * x_4 + 0.000281662518727493,$

$p_{ZY} = 0.00323131078016112 * x_1 - 0.0031183479343113 * x_2 - 0.00292197085083963 * x_3 + 0.00279764468654777 * x_4 + 8.5748210750948e - 5,$

$p_{IZ} = -0.121768689219839 * x_1 - 0.121881652065689 * x_2 + 0.12207802914916 * x_3 - 0.122202355313452 * x_4 + 0.0105763511877318,$

$p_{XZ} = 0.121768689219839 * x_1 + 0.121881652065689 * x_2 + 0.12207802914916 * x_3 - 0.122202355313452 * x_4 - 0.00616401225599934,$

$p_{YZ} = -0.00323131078016112 * x_1 + 0.0031183479343113 * x_2 + 0.00292197085083963 * x_3 - 0.00279764468654777 * x_4 + 0.000108474847635015,$

$p_{ZZ} = 0.00323131078016112 * x_1 - 0.0031183479343113 * x_2 + 0.00292197085083963 * x_3 - 0.00279764468654777 * x_4 + 0.000756240539010848$

B.2 Ramsey experiment with DD

We use the Ramsey experiment to measure the phase coherence of the qubit. During the experiment, the following operations are applied to the qubit: a $\pi/2$ pulse around x axis of the block sphere, a delay of duration t, a $-\pi/2$ pulse around x.Then we perform a phase scan by appending rotation $R(\pi/2, \phi)$ to the sequence and scan ϕ. The result of the phase scan is a cos wave and we extract the contrast $A(t)$ through fitting. Then experiment is repeated for different t and plot decay of $A(t)$ with respect to t. During the delay, we implement DD consisting of pairs of Y pulses at different intervals and . Fig. B.2 shows the decay of $A(t)$ for DD at different intervals (every 75us, 150us and no DD). The more frequent DD is, the faster the contrast decays and the shorter the coherence time, indicating that the net effect of DD is adding more noise into the qubit. The curve for no DD is lower than the other curves because of a phase offset was set incorrectly in the experiment. However it would only affect the height of the curve but not the decay rate. Green curve with no DD still has the lowest decay rate.

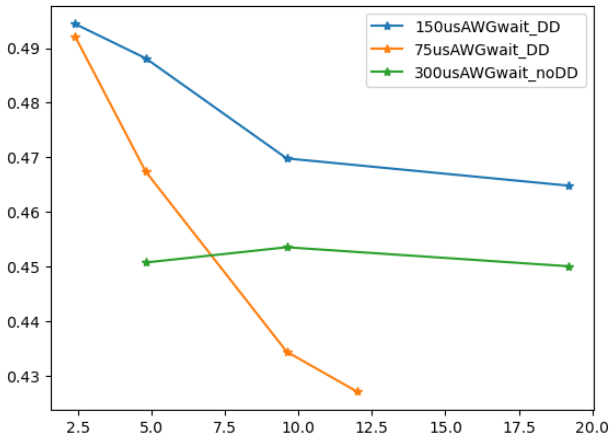

Figure B.1: Decay of the Ramsey contrast with DD of different frequency.

This is consistent with our understanding of the source of phase incoherence on idle qubits. In our experiment, qubit phase coherence time is limited by the stability of the path length difference of the two counter-propogating Raman beam, which is more likely to generate stochastic noise rather than correlated noise. Therefore DD will not be helpful.

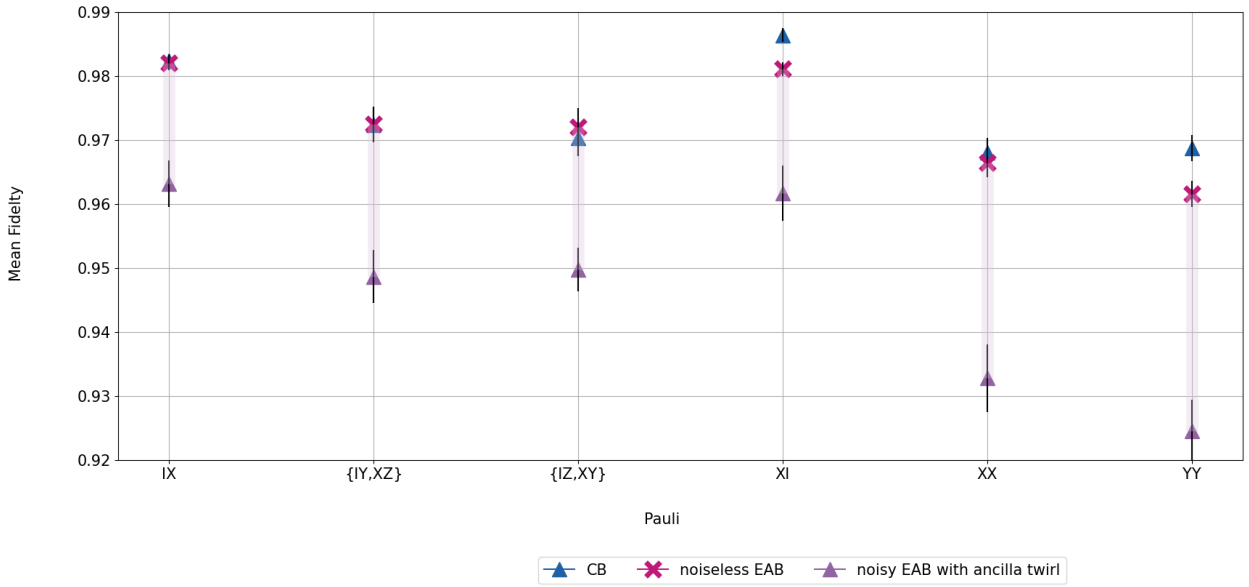

Figure B.2

B.3 Experimental drift in noiseless EAB results

In Fig. 4.15, the noiseless EAB results (pink x symbol) agrees with noisy EAB (cyan triangles) especially well for the left side of the plot ($\{IX, IY, XZ, IZ, XY, XI, XX\}$). This might be related to experimental drift. Gate fidelity fluctuates slightly due to unstabilized variables in the system, such as stark shift fluctuations, beam path stability, and so on. CB data for $\{IX, IY, XZ, IZ, XY, XI, XX, YY\}$ were collected during the same experiment period with noiseless EAB data. However, CB data for $\{YI, ZX, YX, ZI, YZ, ZY, ZZ\}$ were collected a weekend after, at which point small drifts might have happened and affected the agreement between the results. Fig. B.2 shows the subset of CB data collected in the same experimental period as noiseless EAB .

Due to the high volume of circuits required for CB, the data collection usually spans for multiple days, during which experimental drifts can occur. During each data collection, the experiment always undergoes a standard calibration procedure and is calibrated to its best possible performance within our control. However, stark shift fluctuation, bean path stability, and other unexpected shifts in the system that are not actively stabilized can cause

experimental performance to vary between or even during each data collection. We observed that, although the discrepancy between EAB and CB is real (multiple sets of comparison data taken at different times showed CB consistently yields process fidelity $0.5\% - 1\%$ higher than noisy EAB), the overall fidelity of process measured by both protocols can drift by about 0.5%.

A better way to carry out a comparison is to randomize the data-taking order of all circuits which will even out the effect of experimental drift in each data set. The calibration method mentioned in [220] will reduce both EAB and CB experimental time significantly, which will reduce the effect of experimental drift as well.

Appendix C

QFT formulation circuits and phase shift derivation

C.1 QFT circuit

We want to scale up from the quantum mechanics picture to the field theory perspective, in other words the full Ising model. As in the quantum mechanical case, we will need to break up this circuit into three parts: 1) state Preparation, 2) Trotter Evolution, 3) momentum Projection. The various circuits and the relative costs are discussed below.

We want to prepare the same initial state that we proposed in the main text mapped on to the Ising Model. The initial state that we prepared,

$$|\psi_i\rangle = \frac{1}{\sqrt{2}}\Big(|01\rangle + i|10\rangle\Big), \tag{C.1}$$

can be remapped to the Ising model by using the inverse mapping originally described in the text:

$$\begin{aligned} &|00\rangle \to |1000\rangle,\ |01\rangle \to |0100\rangle \\ &|10\rangle \to |0010\rangle,\ |11\rangle \to |0001\rangle. \end{aligned} \tag{C.2}$$

This remapping will give us the initial state:

$$|\psi_i\rangle = \frac{1}{\sqrt{2}}\Big(|0100\rangle + i|0010\rangle\Big). \tag{C.3}$$

This state can easily be prepared with 1 XX gate and one single qubit rotation.

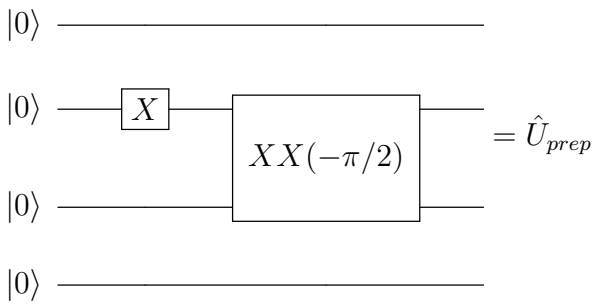

(C.4)

The time evolution of the system can be easily written in terms of a circuit requiring at most 3 XX gates per Trotter step when using a four site system, which is 2 XX gates deep, see Eq. (3.39).

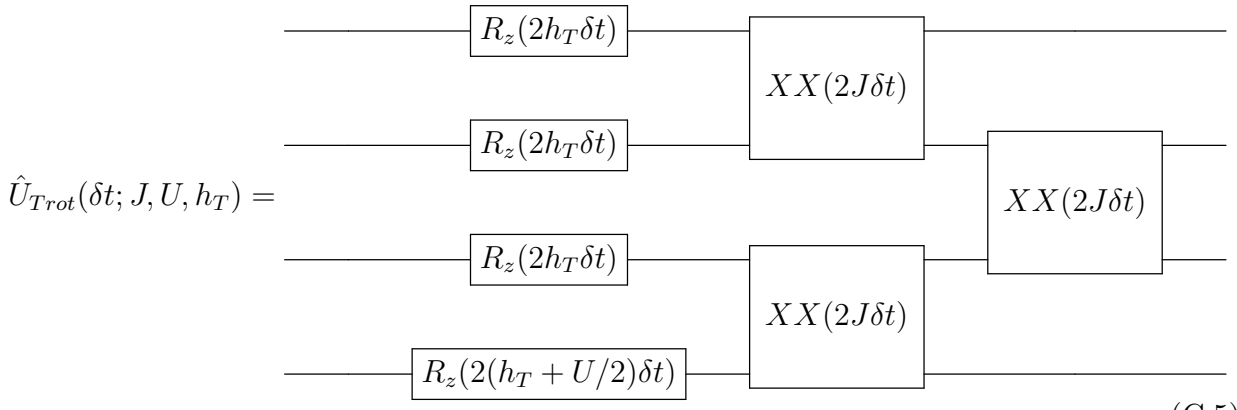

(C.5)

The final portion of the quantum simulation is a Fourier transformation to take the circuit into momentum space [86, 149]. This transformation can easily be done using four two-qubit

operations.

$\hat{U}_{fft} =$ 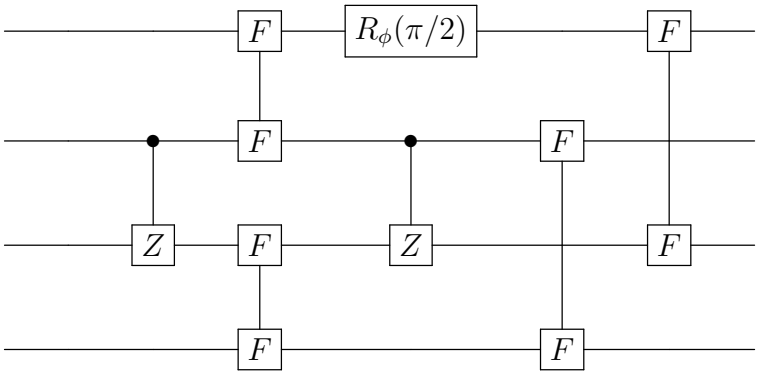

(C.6)

Where F is given by the matrix:

$$F = \begin{pmatrix} 1 & 0 & 0 & 0 \\ 0 & \frac{1}{\sqrt{2}} & \frac{1}{\sqrt{2}} & 0 \\ 0 & \frac{1}{\sqrt{2}} & -\frac{1}{\sqrt{2}} & 0 \\ 0 & 0 & 0 & -1 \end{pmatrix}. \tag{C.7}$$

This can be decomposed into at most 4 CNOT gates. It should be noted this is different from the traditional quantum Fourier transform which uses binary encoding for the qubits.

The measurement is done then in the z-basis and we select out the states $|0010\rangle$ and $|0001\rangle$ for the $|k\rangle$ and $|-k\rangle$ state respectively.

C.2 Phase Shift Derivation

The discrete Schrödinger equation obtained in the limit of small J, with $U = 0$, and no boundaries admits plane wave solutions $e^{\pm ikx}$ with energy $2J(1 - \cos(k))$. The additive constant has been adjusted in order to have zero energy at zero momentum. If we introduce a right wall and impose $\psi(N + 1) = 0$, we need a relative phase $-e^{i2k(N+1)}$ for the reflected wave e^{-ikx}. If, in addition, we also introduce a repulsive potential $U > 0$ at the rightmost site N, the problem with a right wall can be solved by introducing the phase shift. A short

calculation shows that:

$$e^{i2\delta(k)} = e^{-i2k}\frac{U + Je^{ik}}{U + Je^{-ik}}, \tag{C.8}$$

We are now in position to make two independent calculations of $\Delta t^\star$. In the first one, we use

$$\Delta t_W = 2\delta'(k)/(\partial E/\partial k), \tag{C.9}$$

and

$$\Delta t^\star \equiv t^\star_{int.} - t^\star_{free} = \frac{\Delta t_W}{2}, \tag{C.10}$$

discussed in the main text, together with the exact expression for $\delta'(k)$ from Eq. (3.10) to get:

$$\Delta t^* = (-1 + J\frac{U\cos(k) + J}{U^2 + J^2 + 2JU\cos(k)})/2J\sin(k). \tag{C.11}$$

The other method consists in using the real-time evolution to calculate $R_-(t)$ and determine the time $t^\star$ where $R_-(t^\star) = 0.5$. This second method depends on the volume and the details of the initial wavepacket. It is important to prepare a wave packet that is broad enough in space to have sharply defined momentum but not too broad so that it reflects too early. In the numerical calculations, we used an initial wavepacket

$$\psi(x) \propto e^{ikx - (x-N/2)^2/(N/4)^2}. \tag{C.12}$$

The comparison between these results and Wigner formula are shown in the text.

A few words of explanation regarding the low k approximate formula for $\delta(k)$. From Eq. (3.10), we can expand $\delta(k)$ in power of k. For our numerical values $J = 0.02$ and $U = 0.03$, we obtain

$$\delta(k) \simeq -0.6k + 0.008k^3 + \ldots \tag{C.13}$$

As we see, for $0 \leq k \leq 0.5$ the correction to the linear approximation are less then one

percent and we are justified in using the approximation

$$\delta(k) \simeq \delta'(0)k. \tag{C.14}$$

Appendix D

Bell-type non-local games

In Table D.1 we explicitly list our experimental estimates for each stabilizer expectation value, before and after SPAM correction, along with 1σ statistical uncertainties. These values are the same as those plotted in Fig. 3.13 of the main text. Furthermore, in this table the stabilizers are partitioned into our choice of locally commuting sets, such that we measure all stabilizers in each set by a single Pauli measurement setting.

Table D.1: Expectation values for the 63 nontrivial stabilizers of $|C_6\rangle$ estimated from the CBF experiment. Uncertainties denote 1σ standard errors. Horizontal rules indicate our partitioning of the stabilizers into 37 locally commuting sets, such that we estimate all stabilizers in that set from the same global Pauli measurement.

		Expectation value	
Input	Stabilizer	Raw value	SPAM-corrected
000001	$+ZIIIZX$	0.7164(10)	0.7616(10)
001000	$+IZXZII$	0.6732(10)	0.7178(11)
001001	$+ZZXZZX$	0.4952(12)	0.5627(14)
000010	$+IIIZXZ$	0.7208(10)	0.7654(10)
010000	$+ZXZIII$	0.7320(10)	0.7787(10)
010010	$+ZXZZXZ$	0.5352(12)	0.6046(14)
000011	$+ZIIZYY$	0.7656(9)	0.8302(10)

TABLE D.1. *(Continued).*

		Expectation value	
Input	Stabilizer	Raw value	SPAM-corrected
010011	$+IXZZYY$	0.6168(11)	0.6813(12)
000100	$+IIZXZI$	0.6764(10)	0.7205(11)
100000	$+XZIIIZ$	0.7200(10)	0.7646(10)
100100	$+XZZXZZ$	0.5324(12)	0.6019(14)
000101	$+ZIZXIX$	0.5748(12)	0.6221(13)
010001	$+IXZIZX$	0.5584(12)	0.6034(13)
010100	$+ZXIXZI$	0.5900(11)	0.6448(12)
000110	$+IIZYYZ$	0.5360(12)	0.5803(13)
100110	$+XZZYYI$	0.4368(13)	0.4862(14)
000111	$-ZIZYXY$	0.6112(11)	0.6765(12)
010111	$-IXIYXY$	0.5936(11)	0.6449(12)
001010	$+IZXIXZ$	0.5536(12)	0.5984(13)
100010	$+XZIZXI$	0.5392(12)	0.5884(13)
101000	$+XIXZIZ$	0.5832(11)	0.6311(12)
001011	$+ZZXIYY$	0.6084(11)	0.6718(12)
001100	$+IZYYZI$	0.7376(10)	0.8037(10)
101100	$+XIYYZZ$	0.6316(11)	0.6981(12)
001101	$+ZZYYIX$	0.6068(11)	0.6712(12)
001110	$-IZYXYZ$	0.5924(11)	0.6565(13)
101110	$-XIYXYI$	0.5308(12)	0.5784(13)
001111	$+ZZYXXY$	0.7056(10)	0.7970(11)
010101	$+IXIXIX$	0.5368(12)	0.5690(13)
111110	$-YXXXYI$	0.6228(11)	0.6925(12)

TABLE D.1. *(Continued).*

Input	Stabilizer	Expectation value	
		Raw value	SPAM-corrected
010110	$+ZXIYYZ$	0.4936(12)	0.5483(14)
011000	$+ZYYZII$	0.5768(12)	0.6275(13)
011010	$+ZYYIXZ$	0.4676(13)	0.5171(14)
011001	$+IYYZZX$	0.4500(13)	0.4976(14)
011011	$+IYYIYY$	0.5200(12)	0.5628(13)
101101	$+YIYYIY$	0.5584(12)	0.6037(13)
110110	$+YYIYYI$	0.5016(12)	0.5487(13)
011100	$-ZYXYZI$	0.6444(11)	0.7192(12)
011101	$-IYXYIX$	0.5524(12)	0.5982(13)
011110	$+ZYXXYZ$	0.5528(12)	0.6233(13)
011111	$-IYXXXY$	0.6544(11)	0.7232(12)
100001	$+YZIIZY$	0.5404(12)	0.5872(13)
101001	$+YIXZZY$	0.4708(12)	0.5214(14)
100011	$-YZIZYX$	0.6172(11)	0.6856(12)
101011	$-YIXIYX$	0.5836(11)	0.6308(12)
100101	$+YZZXIY$	0.4624(13)	0.5114(14)
100111	$+YZZYXX$	0.5476(12)	0.6190(13)
101010	$+XIXIXI$	0.5500(12)	0.5863(13)
111101	$-XXXYIY$	0.6764(10)	0.7486(12)
101111	$-YIYXXX$	0.6884(10)	0.7606(11)
110000	$+YYZIIZ$	0.7484(9)	0.8090(10)
110100	$+YYIXZZ$	0.5948(11)	0.6597(13)
110001	$-XYZIZY$	0.6144(11)	0.6785(12)

TABLE D.1. *(Continued).*

		Expectation value	
Input	Stabilizer	Raw value	SPAM-corrected
110101	$-XYIXIY$	0.5580(12)	0.6048(13)
110010	$+YYZZXI$	0.5880(11)	0.6549(13)
110011	$+XYZZYX$	0.6952(10)	0.7871(11)
110111	$-XYIYXX$	0.6428(11)	0.7138(12)
111000	$-YXYZIZ$	0.6248(11)	0.6893(12)
111010	$-YXYIXI$	0.5592(12)	0.6091(13)
111001	$+XXYZZY$	0.5164(12)	0.5832(14)
111011	$-XXYIYX$	0.6248(11)	0.6908(12)
111100	$+YXXYZZ$	0.7492(9)	0.8456(11)
111111	$+XXXXXX$	0.8304(8)	0.9378(9)

Bibliography

[1] Scott Aaronson. "Shadow tomography of quantum states". In: *SIAM Journal on Computing* 49.5 (2019), STOC18–368.

[2] Deanna M. Abrams et al. "Implementation of XY entangling gates with a single calibrated pulse". In: *Nat. Electronics* 3.12 (2020), pp. 744–750. DOI: 10.1038/s41928-020-00498-1. URL: https://doi.org/10.1038/s41928-020-00498-1.

[3] Tameem Albash and Daniel A. Lidar. "Adiabatic quantum computation". In: *Reviews of Modern Physics* 90.1 (Jan. 29, 2018), p. 015002. ISSN: 0034-6861, 1539-0756. DOI: 10.1103/RevModPhys.90.015002. URL: https://link.aps.org/doi/10.1103/RevModPhys.90.015002 (visited on 10/13/2024).

[4] C. Huerta Alderete et al. *Experimental realization of para-particle oscillators*. 2021. DOI: 10.48550/ARXIV.2108.05471. URL: https://arxiv.org/abs/2108.05471.

[5] Andrei Alexandru et al. "Gluon field digitization for quantum computers". In: *Physical Review D* 100.11 (Dec. 2019). ISSN: 2470-0029. DOI: 10.1103/physrevd.100.114501. URL: http://dx.doi.org/10.1103/PhysRevD.100.114501.

[6] Andris Ambainis. *Quantum search algorithms*. Apr. 3, 2005. arXiv: quant-ph/0504012. URL: http://arxiv.org/abs/quant-ph/0504012 (visited on 10/09/2024).

[7] Janet Anders and Dan E. Browne. "Computational Power of Correlations". In: *Phys. Rev. Lett.* 102 (5 Feb. 2009), p. 050502. DOI: 10.1103/PhysRevLett.102.050502. URL: https://link.aps.org/doi/10.1103/PhysRevLett.102.050502.

[8] Anurag Anshu, Zeph Landau, and Yunchao Liu. "Distributed quantum inner product estimation". In: *arXiv preprint arXiv:2111.03273* (2021).

[9] Frank Arute et al. "Quantum supremacy using a programmable superconducting processor". In: *Nature* 574.7779 (2019), pp. 505–510. DOI: 10.1038/s41586-019-1666-5.

[10] Alán Aspuru-Guzik et al. "Simulated Quantum Computation of Molecular Energies". In: *Science* 309.5741 (2005), pp. 1704–1707. DOI: 10.1126/science.1113479. URL: https://www.science.org/doi/abs/10.1126/science.1113479.

[11] D. P. L. Aude Craik et al. "High-fidelity spatial and polarization addressing of Ca + 43 qubits using near-field microwave control". In: *Physical Review A* 95.2 (Feb. 27, 2017), p. 022337. ISSN: 2469-9926, 2469-9934. DOI: 10.1103/PhysRevA.95.022337. URL: https://link.aps.org/doi/10.1103/PhysRevA.95.022337 (visited on 10/14/2024).

[12] Marlon Azinović et al. "Assessment of Quantum Annealing for the Construction of Satisfiability Filters". In: *SciPost Phys.* 2 (2 2017), p. 013. DOI: 10.21468/SciPostPhys.2.2.013. URL: https://scipost.org/10.21468/SciPostPhys.2.2.013.

[13] Manuel Bähr et al. "Herwig++ Physics and Manual". In: *European Physical Journal C* 58 (Dec. 2008), pp. 639–707. DOI: 10.1140/epjc/s10052-008-0798-9.

[14] C. H. Baldwin et al. "High-fidelity light-shift gate for clock-state qubits". In: *Phys. Rev. A* 103 (1 Jan. 2021), p. 012603. DOI: 10.1103/PhysRevA.103.012603. URL: https://link.aps.org/doi/10.1103/PhysRevA.103.012603.

[15] C. J. Ballance et al. "High-Fidelity Quantum Logic Gates Using Trapped-Ion Hyperfine Qubits". In: *Physical Review Letters* 117.6 (Aug. 4, 2016). Publisher: American Physical Society, p. 060504. DOI: 10.1103/PhysRevLett.117.060504. URL: https://link.aps.org/doi/10.1103/PhysRevLett.117.060504 (visited on 10/08/2024).

[16] C. J. Ballance et al. "High-Fidelity Quantum Logic Gates Using Trapped-Ion Hyperfine Qubits". In: *Phys. Rev. Lett.* 117 (6 Aug. 2016), p. 060504. DOI: 10.1103/PhysRevLett.117.060504.

[17] M. C. Bañuls et al. "Simulating Lattice Gauge Theories within Quantum Technologies". In: *Eur. Phys. J. D* 74.8 (2020), p. 165. DOI: 10.1140/epjd/e2020-100571-8. arXiv: 1911.00003 [quant-ph].

[18] Jonathan Barrett et al. "Modeling Pauli measurements on graph states with nearest-neighbor classical communication". In: *Phys. Rev. A* 75 (1 Jan. 2007), p. 012103. DOI: 10.1103/PhysRevA.75.012103. URL: https://link.aps.org/doi/10.1103/PhysRevA.75.012103.

[19] Andreas Bärtschi and Stephan Eidenbenz. "Grover Mixers for QAOA: Shifting Complexity from Mixer Design to State Preparation". In: *2020 IEEE International Conference on Quantum Computing and Engineering (QCE)*. 2020, pp. 72–82. DOI: 10.1109/QCE49297.2020.00020.

[20] T. Baumgratz et al. "Scalable Reconstruction of Density Matrices". In: *Physical Review Letters* 111.2 (July 11, 2013). Publisher: American Physical Society, p. 020401. DOI: 10.1103/PhysRevLett.111.020401. URL: https://link.aps.org/doi/10.1103/PhysRevLett.111.020401 (visited on 10/17/2024).

[21] O. Băzăvan et al. *Synthesizing a $\hat{\sigma}_z$ spin-dependent force for optical, metastable, and ground state trapped-ion qubits*. 2022. DOI: 10.48550/ARXIV.2207.11193.

[22] J. S. Bell. "On the Einstein Podolsky Rosen paradox". In: *Physics Physique Fizika* 1 (3 Nov. 1964), pp. 195–200. DOI: 10.1103/PhysicsPhysiqueFizika.1.195. URL: https://link.aps.org/doi/10.1103/PhysicsPhysiqueFizika.1.195.

[23] Andreas Bengtsson et al. "Improved Success Probability with Greater Circuit Depth for the Quantum Approximate Optimization Algorithm". In: *Phys. Rev. Applied* 14 (3 Sept. 2020), p. 034010. DOI: 10.1103/PhysRevApplied.14.034010. URL: https://link.aps.org/doi/10.1103/PhysRevApplied.14.034010.

[24] Jan Benhelm et al. "Towards fault-tolerant quantum computing with trapped ions". In: *Nature Physics* 4.6 (2008), pp. 463–466. DOI: 10.1038/nphys961. URL: https://doi.org/10.1038/nphys961.

[25] Ewout van den Berg et al. "Probabilistic error cancellation with sparse Pauli–Lindblad models on noisy quantum processors". en. In: *Nature Physics* 19.8 (Aug. 2023). Publisher: Nature Publishing Group, pp. 1116–1121. ISSN: 1745-2481. DOI: 10.1038/s41567-023-02042-2. URL: https://www.nature.com/articles/s41567-023-02042-2 (visited on 09/30/2024).

[26] Hannes Bernien et al. "Probing many-body dynamics on a 51-atom quantum simulator". In: *Nature* 551.7682 (Nov. 2017), pp. 579–584. DOI: 10.1038/nature24622. arXiv: 1707.04344 [quant-ph].

[27] K. Binder and A. P. Young. "Spin glasses: Experimental facts, theoretical concepts, and open questions". In: *Rev. Mod. Phys.* 58 (4 Oct. 1986), pp. 801–976. DOI: 10.1103/RevModPhys.58.801. URL: https://link.aps.org/doi/10.1103/RevModPhys.58.801.

[28] Robin Blume-Kohout. "Optimal, reliable estimation of quantum states". In: *New Journal of Physics* 12.4 (Apr. 2010), p. 043034. DOI: 10.1088/1367-2630/12/4/043034.

[29] H. Bombin et al. "Strong Resilience of Topological Codes to Depolarization". In: *Physical Review X* 2.2 (Apr. 2012). Publisher: American Physical Society, p. 021004. DOI: 10.1103/PhysRevX.2.021004. URL: https://link.aps.org/doi/10.1103/PhysRevX.2.021004 (visited on 10/17/2024).

[30] Zvika Brakerski et al. "A Cryptographic Test of Quantumness and Certifiable Randomness from a Single Quantum Device". In: *2018 IEEE 59th Annual Symposium on Foundations of Computer Science (FOCS)*. 2018, pp. 320–331. DOI: 10.1109/FOCS.2018.00038.

[31] Zvika Brakerski et al. "Simpler Proofs of Quantumness". In: *15th Conference on the Theory of Quantum Computation, Communication and Cryptography (TQC 2020)*. Ed. by Steven T. Flammia. Vol. 158. Leibniz International Proceedings in Informatics (LIPIcs). Dagstuhl, Germany: Schloss Dagstuhl–Leibniz-Zentrum für Informatik, 2020, 8:1–8:14. ISBN: 978-3-95977-146-7. DOI: 10.4230/LIPIcs.TQC.2020.8. URL: https://drops.dagstuhl.de/opus/volltexte/2020/12067.

[32] S. Bravyi et al. "Quantum advantage with noisy shallow circuits". In: *Nature Physics* (2020), pp. 1–6. DOI: 10.1038/s41567-020-0948-z.

[33] Sergey Bravyi, David Gosset, and Robert Koenig. "Quantum advantage with shallow circuits". In: *Science* 362.6412 (2018), pp. 308–311. DOI: 10.1126/science.aar3106.

[34] Raul A. Briceno, Jozef J. Dudek, and Ross D. Young. "Scattering processes and resonances from lattice QCD". In: *Rev. Mod. Phys.* 90.2 (2018), p. 025001. DOI: 10.1103/RevModPhys.90.025001. arXiv: 1706.06223 [hep-lat].

[35] Raul A. Briceno et al. "Isoscalar $\pi\pi$ scattering and the σ meson resonance from QCD". In: *Phys. Rev. Lett.* 118.2 (2017), p. 022002. DOI: 10.1103/PhysRevLett.118.022002. arXiv: 1607.05900 [hep-ph].

[36] Raul A. Briceño et al. "Two-nucleon systems in a finite volume. II. ${}^3S_1 - {}^3D_1$ coupled channels and the deuteron". In: *Phys. Rev. D* 88.11 (2013), p. 114507. DOI: 10.1103/PhysRevD.88.114507. arXiv: 1309.3556 [hep-lat].

[37] Raúl A. Briceño et al. "The role of boundary conditions in quantum computations of scattering observables". In: (July 2020). arXiv: 2007.01155 [hep-lat].

[38] Hans J. Briegel and Robert Raussendorf. "Persistent Entanglement in Arrays of Interacting Particles". In: *Phys. Rev. Lett.* 86 (5 Jan. 2001), p. 910. DOI: 10.1103/PhysRevLett.86.910. URL: https://journals.aps.org/prl/abstract/10.1103/PhysRevLett.86.910.

[39] Richard C. Brower, David Berenstein, and Hiroki Kawai. *Lattice Gauge Theory for a Quantum Computer*. 2020. arXiv: 2002.10028 [hep-lat].

[40] Lowell S. Brown and Gerald Gabrielse. "Geonium theory: Physics of a single electron or ion in a Penning trap". In: *Reviews of Modern Physics* 58.1 (Jan. 1, 1986), pp. 233–311. ISSN: 0034-6861. DOI: 10.1103/RevModPhys.58.233. URL: https://link.aps.org/doi/10.1103/RevModPhys.58.233 (visited on 10/14/2024).

[41] Nicolas Brunner et al. "Bell nonlocality". In: *Reviews of Modern Physics* 86.2 (Apr. 2014), pp. 419–478. ISSN: 1539-0756. DOI: 10.1103/revmodphys.86.419. URL: http://dx.doi.org/10.1103/RevModPhys.86.419.

[42] Colin D. Bruzewicz et al. "Trapped-ion quantum computing: Progress and challenges". In: *Applied Physics Reviews* 6.2 (May 2019). ISSN: 1931-9401. DOI: 10.1063/1.5088164. URL: http://dx.doi.org/10.1063/1.5088164.

[43] Harry Buhrman et al. "Quantum fingerprinting". In: *Physical Review Letters* 87.16 (2001), p. 167902.

[44] Vera von Burg et al. "Quantum computing enhanced computational catalysis". In: *Physical Review Research* 3.3 (July 16, 2021). Publisher: American Physical Society, p. 033055. DOI: 10.1103/PhysRevResearch.3.033055. URL: https://link.aps.org/doi/10.1103/PhysRevResearch.3.033055 (visited on 10/09/2024).

[45] Guido Burkard et al. "Semiconductor spin qubits". In: *Rev. Mod. Phys.* 95 (2 June 2023), p. 025003. DOI: 10.1103/RevModPhys.95.025003. URL: https://link.aps.org/doi/10.1103/RevModPhys.95.025003.

[46] Boye Buyens et al. "Real-time simulation of the Schwinger effect with Matrix Product States". In: *Phys. Rev. D* 96.11 (2017), p. 114501. DOI: 10.1103/PhysRevD.96.114501. arXiv: 1612.00739 [hep-lat].

[47] Adán Cabello, Otfried Gühne, and David Rodríguez. "Mermin inequalities for perfect correlations". In: *Phys. Rev. A* 77 (6 June 2008), p. 062106. DOI: 10.1103/PhysRevA.77.062106. URL: https://link.aps.org/doi/10.1103/PhysRevA.77.062106.

[48] Madelyn Cain et al. *Quantum speedup for combinatorial optimization with flat energy landscapes*. July 7, 2023. arXiv: 2306.13123[cond-mat,physics:quant-ph]. URL: http://arxiv.org/abs/2306.13123 (visited on 10/09/2024).

[49] Jose Carrasco et al. "Theoretical and Experimental Perspectives of Quantum Verification". In: *PRX Quantum* 2 (1 Mar. 2021), p. 010102. DOI: 10.1103/PRXQuantum.2.010102.

[50] Raino Ceccarelli et al. "Experimental Entanglement and Nonlocality of a Two-Photon Six-Qubit Cluster State". In: *Phys. Rev. Lett.* 103 (16 Oct. 2009), p. 160401. DOI: 10.1103/PhysRevLett.103.160401. URL: https://link.aps.org/doi/10.1103/PhysRevLett.103.160401.

[51] Alba Cervera-Lierta. "Exact Ising model simulation on a quantum computer". In: *Quantum* 2 (Dec. 2018), p. 114. ISSN: 2521-327X. DOI: 10.22331/q-2018-12-21-114. URL: https://doi.org/10.22331/q-2018-12-21-114.

[52] R. Chaves et al. "Unifying Framework for Relaxations of the Causal Assumptions in Bell's Theorem". In: *Phys. Rev. Lett.* 114 (14 Apr. 2015), p. 140403. DOI: 10.1103/PhysRevLett.114.140403. URL: https://link.aps.org/doi/10.1103/PhysRevLett.114.140403.

[53] Rafael Chaves, Daniel Cavalcanti, and Leandro Aolita. "Causal hierarchy of multipartite Bell nonlocality". In: *Quantum* 1 (Aug. 2017), p. 23. ISSN: 2521-327X. DOI: 10.22331/q-2017-08-04-23. URL: https://doi.org/10.22331/q-2017-08-04-23.

[54] Senrui Chen et al. "Quantum advantages for Pauli channel estimation". In: *Physical Review A* 105.3 (Mar. 2022). Publisher: American Physical Society, p. 032435. DOI: 10.1103/PhysRevA.105.032435. URL: https://link.aps.org/doi/10.1103/PhysRevA.105.032435 (visited on 09/28/2024).

[55] Senrui Chen et al. "The learnability of Pauli noise". en. In: *Nature Communications* 14.1 (Jan. 2023). Publisher: Nature Publishing Group, p. 52. ISSN: 2041-1723. DOI: 10.1038/s41467-022-35759-4. URL: https://www.nature.com/articles/s41467-022-35759-4 (visited on 09/30/2024).

[56] T. Choi et al. "Optimal Quantum Control of Multimode Couplings between Trapped-Ion Qubits for Scalable Entanglement". In: *Phys. Rev. Lett.* 112 (19 May 2014), p. 190502. DOI: 10.1103/PhysRevLett.112.190502. URL: https://link.aps.org/doi/10.1103/PhysRevLett.112.190502.

[57] J. I. Cirac and P. Zoller. "Quantum Computations with Cold Trapped Ions". In: *Phys. Rev. Lett.* 74 (20 May 1995), pp. 4091–4094. DOI: 10.1103/PhysRevLett.74.4091. URL: https://link.aps.org/doi/10.1103/PhysRevLett.74.4091.

[58] J. I. Cirac and P. Zoller. "Quantum Computations with Cold Trapped Ions". In: *Phys. Rev. Lett.* 74 (20 May 1995), pp. 4091–4094. DOI: 10.1103/PhysRevLett.74.4091. URL: https://link.aps.org/doi/10.1103/PhysRevLett.74.4091.

[59] Craig R. Clark et al. "High-Fidelity Bell-State Preparation with $\^{}\{40\}\{\mathrm\{Ca\}\}\^{}\{+\}$ Optical Qubits". In: *Physical Review Letters* 127.13 (Sept. 24, 2021). Publisher: American Physical Society, p. 130505. DOI: 10.1103/PhysRevLett.127.130505. URL: https://link.aps.org/doi/10.1103/PhysRevLett.127.130505 (visited on 10/08/2024).

[60] R. Cleve et al. "Consequences and limits of nonlocal strategies". In: *Proceedings. 19th IEEE Annual Conference on Computational Complexity, 2004.* 2004, pp. 236–249. DOI: 10.1109/CCC.2004.1313847.

[61] Matthew Coudron, Jalex Stark, and Thomas Vidick. "Trading locality for time: certifiable randomness from low-depth circuits". In: *arXiv preprint arXiv:1810.04233* (2018). URL: https://arxiv.org/abs/1810.04233.

[62] Marcus Cramer et al. "Efficient quantum state tomography". In: *Nature Communications* 1.1 (Dec. 21, 2010). Publisher: Nature Publishing Group, p. 149. ISSN: 2041-1723. DOI: 10.1038/ncomms1147. URL: https://www.nature.com/articles/ncomms1147 (visited on 10/17/2024).

[63] Andrew Cross. "The IBM Q experience and QISKit open-source quantum computing software". In: *APS March Meeting Abstracts*. Vol. 2018. 2018, pp. L58–003.

[64] Andrew W Cross et al. "Validating quantum computers using randomized model circuits". In: *Physical Review A* 100.3 (2019), p. 032328. DOI: 10.1103/PhysRevA.100.032328.

[65] Austin K. Daniel and Akimasa Miyake. "Quantum Computational Advantage with String Order Parameters of One-Dimensional Symmetry-Protected Topological Order". In: *Phys. Rev. Lett.* 126 (9 Mar. 2021), p. 090505. DOI: 10.1103/PhysRevLett.126.090505. URL: https://link.aps.org/doi/10.1103/PhysRevLett.126.090505.

[66] Austin K. Daniel et al. "Quantum computational advantage attested by nonlocal games with the cyclic cluster state". In: *Physical Review Research* 4.3 (July 22, 2022). Publisher: American Physical Society, p. 033068. DOI: 10.1103/PhysRevResearch.4.033068. URL: https://link.aps.org/doi/10.1103/PhysRevResearch.4.033068 (visited on 10/17/2024).

[67] Christoph Dankert et al. "Exact and approximate unitary 2-designs and their application to fidelity estimation". en. In: *Physical Review A* 80.1 (July 2009), p. 012304. ISSN: 1050-2947, 1094-1622. DOI: 10.1103/PhysRevA.80.012304. URL: https://link.aps.org/doi/10.1103/PhysRevA.80.012304 (visited on 09/29/2024).

[68] Zohreh Davoudi. "The path from finite to infinite volume: Hadronic observables from lattice QCD". In: *PoS* LATTICE2018 (2018), p. 014. DOI: 10.22323/1.334.0014. arXiv: 1812.11899 [hep-lat].

[69] S. Debnath et al. "Demonstration of a small programmable quantum computer with atomic qubits". In: *Nature* 536.7614 (2016), pp. 63–66. DOI: 10.1038/nature18648. URL: https://doi.org/10.1038/nature18648.

[70] Shantanu Debnath et al. "Demonstration of a small programmable quantum computer with atomic qubits". In: *Nature* 536.7614 (2016), pp. 63–66.

[71] Pablo Díez-Valle, Diego Porras, and Juan José García-Ripoll. *QAOA pseudo-Boltzmann states*. 2022. arXiv: 2201.03358 [quant-ph].

[72] Adam Douglass, Andrew D. King, and Jack Raymond. "Constructing SAT Filters with a Quantum Annealer". In: *Theory and Applications of Satisfiability Testing – SAT 2015*. Ed. by Marijn Heule and Sean Weaver. Cham: Springer International Publishing, 2015, pp. 104–120. ISBN: 978-3-319-24318-4.

[73] L.-M. Duan et al. "Scalable trapped-ion quantum computation with a probabilistic ion-photon mapping". In: *Quantum Info. Comput.* 4.3 (May 1, 2004), pp. 165–173. ISSN: 1533-7146.

[74] David K Duvenaud et al. "Convolutional Networks on Graphs for Learning Molecular Fingerprints". In: *Advances in Neural Information Processing Systems*. Ed. by C. Cortes et al. Vol. 28. Curran Associates, Inc., 2015. URL: https://proceedings.neurips.cc/paper/2015/file/f9be311e65d81a9ad8150a60844bb94c-Paper.pdf.

[75] Bradley Efron and Gail Gong. "A leisurely look at the bootstrap, the jackknife, and cross-validation". In: *The American Statistician* 37.1 (1983), pp. 36–48.

[76] Laird Egan et al. "Fault-tolerant operation of a quantum error-correction code". In: *arXiv preprint arXiv:2009.11482* (2020).

[77] Andreas Elben et al. "Cross-Platform Verification of Intermediate Scale Quantum Devices". In: *Phys. Rev. Lett.* 124 (1 Jan. 2020), p. 010504. DOI: 10.1103/PhysRevLett.124.010504.

[78] Alexander Erhard et al. "Characterizing large-scale quantum computers via cycle benchmarking". en. In: *Nature Communications* 10.1 (Nov. 2019). Publisher: Nature Publishing Group, p. 5347. ISSN: 2041-1723. DOI: 10.1038/s41467-019-13068-7. URL: https://www.nature.com/articles/s41467-019-13068-7 (visited on 08/29/2024).

[79] Majid Eskandarpour et al. "Sustainable supply chain network design: An optimization-oriented review". In: *Omega* 54 (2015), pp. 11–32. ISSN: 0305-0483. DOI: https://doi.org/10.1016/j.omega.2015.01.006. URL: https://www.sciencedirect.com/science/article/pii/S0305048315000080.

[80] S. M. Ali Eslami, Nicolas Heess, and John Winn. "The Shape Boltzmann Machine: A strong model of object shape". In: *2012 IEEE Conference on Computer Vision and Pattern Recognition*. 2012, pp. 406–413. DOI: 10.1109/CVPR.2012.6247702.

[81] Wenqi Fan et al. *Graph Neural Networks for Social Recommendation*. 2019. arXiv: 1902.07243 [cs.IR].

[82] Chao Fang et al. *Realization of Scalable Cirac-Zoller Multi-Qubit Gates*. 2023. DOI: 10.48550/ARXIV.2301.07564. URL: https://arxiv.org/abs/2301.07564.

[83] Edward Farhi, Jeffrey Goldstone, and Sam Gutmann. *A Quantum Approximate Optimization Algorithm*. 2014. arXiv: 1411.4028 [quant-ph].

[84] Edward Farhi and Aram W Harrow. *Quantum Supremacy through the Quantum Approximate Optimization Algorithm*. 2019. arXiv: 1602.07674 [quant-ph].

[85] Edward Farhi et al. "A Quantum Adiabatic Evolution Algorithm Applied to Random Instances of an NP-Complete Problem". In: *Science* 292.5516 (Apr. 20, 2001), pp. 472–475. ISSN: 0036-8075, 1095-9203. DOI: 10.1126/science.1057726. arXiv: quant-ph/0104129. URL: http://arxiv.org/abs/quant-ph/0104129 (visited on 10/09/2024).

[86] Andrew J. Ferris. "Fourier Transform for Fermionic Systems and the Spectral Tensor Network". In: *Phys. Rev. Lett.* 113 (1 July 2014), p. 010401. DOI: 10.1103/PhysRevLett.113.010401. URL: https://link.aps.org/doi/10.1103/PhysRevLett.113.010401.

[87] C. Figgatt et al. "Parallel entangling operations on a universal ion-trap quantum computer". In: *Nature* 572.7769 (2019), pp. 368–372. DOI: 10.1038/s41586-019-1427-5.

[88] Caroline Margaret Figgatt. "Building and Programming a Universal Ion Trap Quantum Computer". PhD thesis. University of Maryland, 2018.

[89] Steven T. Flammia and Yi-Kai Liu. "Direct Fidelity Estimation from Few Pauli Measurements". In: *Phys. Rev. Lett.* 106 (23 June 2011), p. 230501. DOI: 10.1103/PhysRevLett.106.230501. URL: https://link.aps.org/doi/10.1103/PhysRevLett.106.230501.

[90] Steven T. Flammia and Yi-Kai Liu. "Direct Fidelity Estimation from Few Pauli Measurements". en. In: *Physical Review Letters* 106.23 (June 2011). arXiv:1104.4695 [quant-ph], p. 230501. ISSN: 0031-9007, 1079-7114. DOI: 10.1103/PhysRevLett.106.230501. URL: http://arxiv.org/abs/1104.4695 (visited on 09/30/2024).

[91] Steven T. Flammia and Joel J. Wallman. "Efficient Estimation of Pauli Channels". In: *ACM Transactions on Quantum Computing* 1.1 (Dec. 2020), 3:1–3:32. DOI: 10.1145/3408039. URL: https://dl.acm.org/doi/10.1145/3408039 (visited on 09/29/2024).

[92] Tobias Fritz. "Beyond Bell's theorem: correlation scenarios". In: *New Journal of Physics* 14.10 (Oct. 2012), p. 103001. DOI: 10.1088/1367-2630/14/10/103001. URL: https://doi.org/10.1088%2F1367-2630%2F14%2F10%2F103001.

[93] J. P. Gaebler et al. "High-Fidelity Universal Gate Set for ${^{9}\mathrm{Be}}^{+}$ Ion Qubits". In: *Physical Review Letters* 117.6 (Aug. 4, 2016). Publisher: American Physical Society, p. 060505. DOI: 10.1103/PhysRevLett.117.060505. URL: https://link.aps.org/doi/10.1103/PhysRevLett.117.060505 (visited on 10/08/2024).

[94] François Le Gall. "Average-Case Quantum Advantage with Shallow Circuits". In: *34th Computational Complexity Conference (CCC 2019)*. Vol. 137. Leibniz International Proceedings in Informatics (LIPIcs). 2019, 21:1–21:20. ISBN: 978-3-95977-116-0. DOI: 10.4230/LIPIcs.CCC.2019.21. URL: http://drops.dagstuhl.de/opus/volltexte/2019/10843.

[95] Bryan T Gard et al. "Efficient symmetry-preserving state preparation circuits for the variational quantum eigensolver algorithm". In: *NPJ Quantum Inf.* 6.1 (2020), pp. 1–9.

[96] Marissa Giustina et al. "Significant-Loophole-Free Test of Bell's Theorem with Entangled Photons". In: *Phys. Rev. Lett.* 115 (25 Dec. 2015), p. 250401. DOI: 10.1103/PhysRevLett.115.250401. URL: https://link.aps.org/doi/10.1103/PhysRevLett.115.250401.

[97] John Golden et al. *QAOA-based Fair Sampling on NISQ Devices*. 2021. arXiv: 2101.03258 [quant-ph].

[98] Carla P. Gomes, Ashish Sabharwal, and Bart Selman. "Model Counting: A New Strategy for Obtaining Good Bounds". In: *Proceedings of the 21st National Conference on Artificial Intelligence - Volume 1*. AAAI'06. Boston, Massachusetts: AAAI Press, 2006, pp. 54–61. ISBN: 9781577352815.

[99] Carla P. Gomes, Ashish Sabharwal, and Bart Selman. *Handbook of Satisfiability*. Ed. by Armin Biere et al. IOS Press, 2008.

[100] Dylan J Gorman et al. "Engineering Vibrationally Assisted Energy Transfer in a Trapped-Ion Quantum Simulator". In: *Phys. Rev. X* 8 (1 Mar. 2018), p. 011038. DOI: 10.1103/PhysRevX.8.011038. URL: https://link.aps.org/doi/10.1103/PhysRevX.8.011038.

[101] Markus Grassl, Andreas Klappenecker, and Martin Rotteler. "Graphs, quadratic forms, and quantum codes". In: *Proceedings IEEE International Symposium on Information Theory*. IEEE. 2002, p. 45. DOI: 10.1109/ISIT.2002.1023317.

[102] Markus Grassl et al. "Quantum Error-Correcting Codes for Qudit Amplitude Damping". In: *IEEE Transactions on Information Theory* 64.6 (June 2018). Conference Name: IEEE Transactions on Information Theory, pp. 4674–4685. ISSN: 1557-9654. DOI: 10.1109/TIT.2018.2790423. URL: https://ieeexplore.ieee.org/document/8248788 (visited on 09/29/2024).

[103] Todd J. Green and Michael J. Biercuk. "Phase-Modulated Decoupling and Error Suppression in Qubit-Oscillator Systems". In: *Phys. Rev. Lett.* 114 (12 Mar. 2015), p. 120502. DOI: 10.1103/PhysRevLett.114.120502. URL: https://link.aps.org/doi/10.1103/PhysRevLett.114.120502.

[104] Daniel M Greenberger, Michael A Horne, and Anton Zeilinger. "Going beyond Bell's theorem". In: *Bell's theorem, quantum theory and conceptions of the universe*. Springer, 1989, pp. 69–72.

[105] C Greganti et al. "Cross-verification of independent quantum devices". In: *Physical Review X* 11.3 (2021), p. 031049.

[106] Daniel Grier, Nathan Ju, and Luke Schaeffer. "Interactive quantum advantage with noisy, shallow Clifford circuits". In: *arXiv preprint arXiv:2102.06833* (2021). URL: https://arxiv.org/abs/2102.06833.

[107] Daniel Grier and Luke Schaeffer. "Interactive shallow Clifford circuits: quantum advantage against NC^1 and beyond". In: *arXiv preprint arXiv:1911.02555* (2019). URL: https://arxiv.org/abs/1911.02555.

[108] David Gross et al. "Quantum State Tomography via Compressed Sensing". In: *Physical Review Letters* 105.15 (Oct. 4, 2010). Publisher: American Physical Society, p. 150401. DOI: 10.1103/PhysRevLett.105.150401. URL: https://link.aps.org/doi/10.1103/PhysRevLett.105.150401 (visited on 10/17/2024).

[109] Particle Data Group, P. A. Zyla, et al. "Review of Particle Physics". In: *Progress of Theoretical and Experimental Physics* 2020.8 (Aug. 2020). 083C01. ISSN: 2050-3911. DOI: 10.1093/ptep/ptaa104. eprint: https://academic.oup.com/ptep/article-pdf/2020/8/083C01/34673722/ptaa104.pdf. URL: https://doi.org/10.1093/ptep/ptaa104.

[110] Lov K. Grover. "Quantum Mechanics Helps in Searching for a Needle in a Haystack". In: *Physical Review Letters* 79.2 (July 14, 1997). Publisher: American Physical Society, pp. 325–328. DOI: 10.1103/PhysRevLett.79.325. URL: https://link.aps.org/doi/10.1103/PhysRevLett.79.325 (visited on 10/09/2024).

[111] Nikodem Grzesiak et al. "Efficient arbitrary simultaneously entangling gates on a trapped-ion quantum computer". In: *Nature Communications* 11.1 (2020), p. 2963. DOI: 10.1038/s41467-020-16790-9. URL: https://doi.org/10.1038/s41467-020-16790-9.

[112] Nikodem Grzesiak et al. "Efficient quantum programming using EASE gates on a trapped-ion quantum computer". In: *Quantum* 6 (Jan. 2022), p. 634. ISSN: 2521-327X. DOI: 10.22331/q-2022-01-27-634. URL: https://doi.org/10.22331/q-2022-01-27-634.

[113] Otfried Gühne et al. "Bell Inequalities for Graph States". In: *Phys. Rev. Lett.* 95 (12 Sept. 2005), p. 120405. DOI: 10.1103/PhysRevLett.95.120405. URL: https://link.aps.org/doi/10.1103/PhysRevLett.95.120405.

[114] Erik Gustafson, Y. Meurice, and Judah Unmuth-Yockey. "Quantum simulation of scattering in the quantum Ising model". In: *Physical Review D* 99 (May 2019). DOI: 10.1103/PhysRevD.99.094503.

[115] Erik Gustafson et al. *Real time evolution of a one-dimensional field theory on a 20 qubit machine*. 2019. arXiv: 1910.09478 [hep-lat].

[116] Erik Gustafson et al. "Real-time quantum calculations of phase shifts using wave packet time delays". In: *Phys. Rev. D* 104 (5 Sept. 2021), p. 054507. DOI: 10.1103/PhysRevD.104.054507. URL: https://link.aps.org/doi/10.1103/PhysRevD.104.054507.

[117] Matthew P. Harrigan et al. "Quantum approximate optimization of non-planar graph problems on a planar superconducting processor". In: *Nat. Phys.* 17.3 (2021), pp. 332–336. DOI: 10.1038/s41567-020-01105-y. URL: https://doi.org/10.1038/s41567-020-01105-y.

[118] Atsuya Hasegawa and François Le Gall. "Quantum Advantage with Shallow Circuits under Arbitrary Corruption". In: *arXiv preprint arXiv:2105.00603* (2021). URL: https://arxiv.org/abs/2105.00603.

[119] Akel Hashim et al. "Randomized Compiling for Scalable Quantum Computing on a Noisy Superconducting Quantum Processor". In: *Physical Review X* 11.4 (Nov. 2021). Publisher: American Physical Society, p. 041039. DOI: 10.1103/PhysRevX.11.041039. URL: https://link.aps.org/doi/10.1103/PhysRevX.11.041039 (visited on 09/29/2024).

[120] Marc Hein et al. "Entanglement in Graph States and its Applications". In: *Proceedings of the International School of Physics "Enrico Fermi": Volume 162: Quantum Computers, Algorithms and Chaos* (Oct. 2006), pp. 115–218. DOI: 10.3254/978-1-61499-018-5-115.

[121] Itay Hen and Marcelo S Sarandy. "Driver Hamiltonians for constrained optimization in quantum annealing". In: *Phys. Rev. A* 93.6 (2016), p. 062312.

[122] Loïc Henriet et al. "Quantum computing with neutral atoms". In: *Quantum* 4 (Sept. 2020), p. 327. ISSN: 2521-327X. DOI: 10.22331/q-2020-09-21-327. URL: https://doi.org/10.22331/q-2020-09-21-327.

[123] Bas Hensen et al. "Loophole-free Bell inequality violation using electron spins separated by 1.3 kilometres". In: *Nature* 526.7575 (2015), pp. 682–686. DOI: 10.1038/nature15759.

[124] Geoffrey E. Hinton. "Training Products of Experts by Minimizing Contrastive Divergence". In: *Neural Comput.* 14.8 (Aug. 2002), pp. 1771–1800. ISSN: 0899-7667. DOI: 10.1162/089976602760128018. URL: https://doi.org/10.1162/089976602760128018.

[125] Matty J Hoban et al. "Non-adaptive measurement-based quantum computation and multi-party Bell inequalities". In: *New Journal of Physics* 13.2 (Feb. 2011), p. 023014. DOI: 10.1088/1367-2630/13/2/023014. URL: https://doi.org/10.1088%5C%2F1367-2630%5C%2F13%5C%2F2%5C%2F023014.

[126] Alex Hobé et al. "Estimating fluid flow rates through fracture networks using combinatorial optimization". In: *Adv Water Resour* 122 (2018), pp. 85–97. ISSN: 0309-1708. DOI: https://doi.org/10.1016/j.advwatres.2018.10.002. URL: https://www.sciencedirect.com/science/article/pii/S0309170818300666.

[127] Eric T. Holland et al. "Optimal control for the quantum simulation of nuclear dynamics". In: *Physical Review A* 101.6 (June 2020). ISSN: 2469-9934. DOI: 10.1103/physreva.101.062307. URL: http://dx.doi.org/10.1103/PhysRevA.101.062307.

[128] Hsin-Yuan Huang, Richard Kueng, and John Preskill. "Predicting many properties of a quantum system from very few measurements". In: *Nature Physics* 16 (2020), pp. 1050–1057. DOI: 10.1038/s41567-020-0932-7.

[129] Hsin-Yuan Huang et al. "Provably efficient machine learning for quantum many-body problems". In: *arXiv preprint arXiv:2106.12627* (2021).

[130] He-Liang Huang et al. "Superconducting quantum computing: a review". In: *Science China Information Sciences* 63.8 (July 2020). ISSN: 1869-1919. DOI: 10.1007/s11432-020-2881-9. URL: http://dx.doi.org/10.1007/s11432-020-2881-9.

[131] "IBM Quantum. https://quantum-computing.ibm.com/, 2021". In: ().

[132] Kazuki Ikeda, Dmitri E. Kharzeev, and Yuta Kikuchi. "Real-time dynamics of Chern-Simons fluctuations near a critical point". In: (Dec. 2020). arXiv: 2012.02926 [hep-ph].

[133] Wolfram Research Inc. *Mathematica, Version 13.1*. Champaign, IL, 2022. URL: https://www.wolfram.com/mathematica.

[134] Mohsin Iqbal et al. "Non-Abelian topological order and anyons on a trapped-ion processor". In: *Nature* 626.7999 (Feb. 2024). Publisher: Nature Publishing Group, pp. 505–511. ISSN: 1476-4687. DOI: 10.1038/s41586-023-06934-4. URL: https://www.nature.com/articles/s41586-023-06934-4 (visited on 10/08/2024).

[135] D. F. V. James. "Quantum dynamics of cold trapped ions with application to quantum computation". In: *Applied Physics B* 66.2 (1998), pp. 181–190. DOI: 10.1007/s003400050373. URL: https://doi.org/10.1007/s003400050373.

[136] Ian T Jolliffe and Jorge Cadima. "Principal component analysis: a review and recent developments". In: *Philosophical Transactions of the Royal Society A: Mathematical, Physical and Engineering Sciences* 374.2065 (2016), p. 20150202.

[137] Petar Jurcevic et al. "Demonstration of quantum volume 64 on a superconducting quantum computing system". In: *Quantum Science and Technology* (2021).

[138] Tadashi Kadowaki and Hidetoshi Nishimori. "Quantum annealing in the transverse Ising model". In: *Phys. Rev. E* 58 (5 Nov. 1998), pp. 5355–5363. DOI: 10.1103/PhysRevE.58.5355. URL: https://link.aps.org/doi/10.1103/PhysRevE.58.5355.

[139] Gregory D Kahanamoku-Meyer et al. "Classically-Verifiable Quantum Advantage from a Computational Bell Test". In: *arXiv preprint arXiv:2104.00687* (2021). URL: https://arxiv.org/abs/2104.00687.

[140] Sabre Kais. "Introduction to Quantum Information and Computation for Chemistry". In: *Advances in Chemical Physics*. Ed. by Sabre Kais. 1st ed. Wiley, Feb. 14, 2014, pp. 1–38. ISBN: 978-1-118-49566-7 978-1-118-74263-1. DOI: 10.1002/9781118742631.ch01. URL: https://onlinelibrary.wiley.com/doi/10.1002/9781118742631.ch01 (visited on 10/09/2024).

[141] Abhinav Kandala et al. "Hardware-efficient variational quantum eigensolver for small molecules and quantum magnets". In: *Nature* 549 (Sept. 2017), 242 EP -. URL: https://doi.org/10.1038/nature23879.

[142] Abhinav Kandala et al. "Error mitigation extends the computational reach of a noisy quantum processor". In: *Nature* 567.7749 (Mar. 2019), pp. 491–495. ISSN: 1476-4687. DOI: 10.1038/s41586-019-1040-7. URL: http://dx.doi.org/10.1038/s41586-019-1040-7.

[143] P. I. Karpov et al. "Spatiotemporal dynamics of particle collisions in quantum spin chains". In: (2020). arXiv: 2011.11624 [cond-mat.quant-gas].

[144] Or Katz, Marko Cetina, and Christopher Monroe. "N-Body Interactions between Trapped-Ion Qubits via Spin-Dependent Squeezing". In: *Phys. Rev. Lett.* 129 (6 Aug. 2022), p. 063603. DOI: 10.1103/PhysRevLett.129.063603. URL: https://link.aps.org/doi/10.1103/PhysRevLett.129.063603.

[145] Dmitri E. Kharzeev and Yuta Kikuchi. "Real-time chiral dynamics from a digital quantum simulation". In: *Phys. Rev. Res.* 2.2 (2020), p. 023342. DOI: 10.1103/PhysRevResearch.2.023342. arXiv: 2001.00698 [hep-ph].

[146] K Kim et al. "Quantum simulation of the transverse Ising model with trapped ions". In: *New Journal of Physics* 13.10 (Oct. 2011), p. 105003. DOI: 10.1088/1367-2630/13/10/105003. URL: https://dx.doi.org/10.1088/1367-2630/13/10/105003.

[147] Minhyuk Kim et al. "Quantum Ising Hamiltonian Programming in Trio, Quartet, and Sextet Qubit Systems". In: *PRX Quantum* 1.2 (Dec. 2020). ISSN: 2691-3399. DOI: 10.1103/prxquantum.1.020323. URL: http://dx.doi.org/10.1103/PRXQuantum.1.020323.

[148] H. J. Kimble. "The quantum internet". In: *Nature* 453.7198 (June 2008), pp. 1023–1030. ISSN: 1476-4687. DOI: 10.1038/nature07127.

[149] Ian D. Kivlichan et al. "Improved Fault-Tolerant Quantum Simulation of Condensed-Phase Correlated Electrons via Trotterization". In: *Quantum* 4 (July 2020), p. 296. ISSN: 2521-327X. DOI: 10.22331/q-2020-07-16-296. URL: http://dx.doi.org/10.22331/q-2020-07-16-296.

[150] N. Klco et al. "Quantum-classical computation of Schwinger model dynamics using quantum computers". In: *Phys. Rev.* A98.3 (2018), p. 032331. DOI: 10.1103/PhysRevA.98.032331. arXiv: 1803.03326 [quant-ph].

[151] E. Knill et al. "Randomized benchmarking of quantum gates". In: *Phys. Rev. A* 77 (1 Jan. 2008), p. 012307. DOI: 10.1103/PhysRevA.77.012307. URL: https://link.aps.org/doi/10.1103/PhysRevA.77.012307.

[152] E. Knill et al. "Randomized benchmarking of quantum gates". In: *Physical Review A* 77.1 (Jan. 2008). Publisher: American Physical Society, p. 012307. DOI: 10.1103/PhysRevA.77.012307. URL: https://link.aps.org/doi/10.1103/PhysRevA.77.012307 (visited on 10/17/2024).

[153] John B. Kogut. "An introduction to lattice gauge theory and spin systems". In: *Rev. Mod. Phys.* 51 (4 Oct. 1979), pp. 659–713. DOI: 10.1103/RevModPhys.51.659. URL: https://link.aps.org/doi/10.1103/RevModPhys.51.659.

[154] John B. Kogut. "The lattice gauge theory approach to quantum chromodynamics". In: *Rev. Mod. Phys.* 55 (3 July 1983), pp. 775–836. DOI: 10.1103/RevModPhys.55.775. URL: https://link.aps.org/doi/10.1103/RevModPhys.55.775.

[155] Henning Labuhn et al. "Tunable two-dimensional arrays of single Rydberg atoms for realizing quantum Ising models". In: *Nature* 534.7609 (June 2016), pp. 667–670. ISSN: 1476-4687. DOI: 10.1038/nature18274. URL: http://dx.doi.org/10.1038/nature18274.

[156] Nathan Lacroix et al. "Improving the Performance of Deep Quantum Optimization Algorithms with Continuous Gate Sets". In: *PRX Quantum* 1 (2 Oct. 2020), p. 110304. DOI: 10.1103/PRXQuantum.1.020304. URL: https://link.aps.org/doi/10.1103/PRXQuantum.1.020304.

[157] Henry Lamm and Scott Lawrence. "Simulation of Nonequilibrium Dynamics on a Quantum Computer". In: *Phys. Rev. Lett.* 121.17 (2018), p. 170501. DOI: 10.1103/PhysRevLett.121.170501. arXiv: 1806.06649 [quant-ph].

[158] Henry Lamm, Scott Lawrence, and Yukari Yamauchi. "Parton physics on a quantum computer". In: *Physical Review Research* 2.1 (Mar. 2020). ISSN: 2643-1564. DOI: 10.1103/physrevresearch.2.013272. URL: http://dx.doi.org/10.1103/PhysRevResearch.2.013272.

[159] Kevin Antony Landsman. "Construction, Optimization, and Applications of a Small Trapped-Ion Quantum Computer". PhD thesis. Univeristy of Maryland, 2019.

[160] B. P. Lanyon et al. "Experimental Violation of Multipartite Bell Inequalities with Trapped Ions". In: *Phys. Rev. Lett.* 112 (10 Mar. 2014), p. 100403. DOI: 10.1103/PhysRevLett.112.100403. URL: https://link.aps.org/doi/10.1103/PhysRevLett.112.100403.

[161] Lingling Lao and Dan Browne. *2QAN: A quantum compiler for 2-local qubit Hamiltonian simulation algorithms*. 2021. arXiv: 2108.02099 [quant-ph].

[162] David Layden, Louisa Ruixue Huang, and P. Cappellaro. *Robustness-optimized quantum error correction*. 2019. DOI: 10.1088/2058-9565/ab79b2.

[163] D. Leibfried et al. "Experimental demonstration of a robust, high-fidelity geometric two ion-qubit phase gate". In: *Nature* 422.6930 (Mar. 2003). Publisher: Nature Publishing Group, pp. 412–415. ISSN: 1476-4687. DOI: 10.1038/nature01492. URL: https://www.nature.com/articles/nature01492 (visited on 10/16/2024).

[164] D. Leibfried et al. "Experimental demonstration of a robust, high-fidelity geometric two ion-qubit phase gate". In: *Nature* 422.6930 (2003), pp. 412–415. DOI: 10.1038/nature01492. URL: https://doi.org/10.1038/nature01492.

[165] A. D. Leu et al. "Fast, High-Fidelity Addressed Single-Qubit Gates Using Efficient Composite Pulse Sequences". In: *Physical Review Letters* 131.12 (Sept. 19, 2023), p. 120601. ISSN: 0031-9007, 1079-7114. DOI: 10.1103/PhysRevLett.131.120601. URL: https://link.aps.org/doi/10.1103/PhysRevLett.131.120601 (visited on 10/14/2024).

[166] Pak Hong Leung et al. "Robust 2-Qubit Gates in a Linear Ion Crystal Using a Frequency-Modulated Driving Force". In: *Phys. Rev. Lett.* 120 (2 Jan. 2018), p. 020501. DOI: 10.1103/PhysRevLett.120.020501. URL: https://link.aps.org/doi/10.1103/PhysRevLett.120.020501.

[167] Ming Li et al. "Generalized Hamiltonian to describe imperfections in ion-light interaction". In: *Phys. Rev. A* 102 (6 Dec. 2020), p. 062616. DOI: 10.1103/PhysRevA.102.062616.

[168] Norbert M Linke et al. "Experimental comparison of two quantum computing architectures". In: *Proceedings of the National Academy of Sciences* 114.13 (2017), pp. 3305–3310.

[169] Seth Lloyd. "Universal Quantum Simulators". In: *Science* 273.5278 (1996), pp. 1073–1078. ISSN: 0036-8075. DOI: 10.1126/science.273.5278.1073. URL: http://science.sciencemag.org/content/273/5278/1073.

[170] Seth Lloyd. "Universal Quantum Simulators". In: *Science* 273.5278 (1996), pp. 1073–1078. DOI: 10.1126/science.273.5278.1073. URL: https://www.science.org/doi/abs/10.1126/science.273.5278.1073.

[171] Chao-Yang Lu et al. "Experimental entanglement of six photons in graph states". In: *Nature Physics* 3.2 (2007), pp. 91–95. DOI: https://doi.org/10.1038/nphys507.

[172] Yao Lu et al. "Global entangling gates on arbitrary ion qubits". In: *Nature* 572.7769 (2019), pp. 363–367. DOI: 10.1038/s41586-019-1428-4. URL: https://doi.org/10.1038/s41586-019-1428-4.

[173] M. Lüscher. "Volume dependence of the energy spectrum in massive quantum field theories". In: *Communications in Mathematical Physics* 105.2 (June 1986), pp. 153–188. ISSN: 1432-0916. DOI: 10.1007/BF01211097. URL: https://doi.org/10.1007/BF01211097.

[174] C. Marquet, F. Schmidt-Kaler, and D. F. V. James. "Phonon–phonon interactions due to non-linear effects in a linear ion trap". In: *Applied Physics B* 76.3 (2003), pp. 199–208. DOI: 10.1007/s00340-003-1097-7. URL: https://doi.org/10.1007/s00340-003-1097-7.

[175] Esteban A. Martinez et al. "Real-time dynamics of lattice gauge theories with a few-qubit quantum computer". In: *Nature* 534.7608 (June 2016), pp. 516–519. ISSN: 1476-4687. DOI: 10.1038/nature18318. URL: http://dx.doi.org/10.1038/nature18318.

[176] Nishad Maskara, Aleksander Kubica, and Tomas Jochym-O'Connor. "Advantages of versatile neural-network decoding for topological codes". In: *Physical Review A* 99.5 (May 2019). Publisher: American Physical Society, p. 052351. DOI: 10.1103/PhysRevA.99.052351. URL: https://link.aps.org/doi/10.1103/PhysRevA.99.052351 (visited on 10/17/2024).

[177] Peter Lukas Wilhelm Maunz. "High Optical Access Trap 2.0." In: (2016).

[178] N. David Mermin. "Extreme quantum entanglement in a superposition of macroscopically distinct states". In: *Phys. Rev. Lett.* 65 (15 Oct. 1990), pp. 1838–1840. DOI: 10.1103/PhysRevLett.65.1838. URL: https://link.aps.org/doi/10.1103/PhysRevLett.65.1838.

[179] Yannick Meurice. *Quantum field theory: a quantum computation approach*. Bristol: Institute of Physics Publishing, 2021.

[180] Yannick Meurice, Ryo Sakai, and Judah Unmuth-Yockey. "Tensor field theory with applications to quantum computing". In: (Oct. 2020). arXiv: 2010.06539 [hep-lat].

[181] M. Michael et al. *New class of quantum error-correcting codes for a bosonic mode*. 2016. DOI: 10.1103/PhysRevX.6.031006.

[182] J. Mizrahi et al. "Quantum control of qubits and atomic motion using ultrafast laser pulses". In: *Applied Physics B* 114.1 (Jan. 1, 2014), pp. 45–61. ISSN: 1432-0649. DOI: 10.1007/s00340-013-5717-6. URL: https://doi.org/10.1007/s00340-013-5717-6 (visited on 10/18/2024).

[183] C. Monroe and J. Kim. "Scaling the Ion Trap Quantum Processor". In: *Science* 339.6124 (Mar. 8, 2013). Publisher: American Association for the Advancement of Science, pp. 1164–1169. DOI: 10.1126/science.1231298. URL: https://www.science.org/doi/10.1126/science.1231298 (visited on 10/08/2024).

[184] C. Monroe et al. "Programmable quantum simulations of spin systems with trapped ions". In: *Rev. Mod. Phys.* 93 (2 Apr. 2021), p. 025001. DOI: 10.1103/RevModPhys.93.025001. URL: https://link.aps.org/doi/10.1103/RevModPhys.93.025001.

[185] S. A. Moses et al. "A Race-Track Trapped-Ion Quantum Processor". In: *Physical Review X* 13.4 (Dec. 18, 2023). Publisher: American Physical Society, p. 041052. DOI: 10.1103/PhysRevX.13.041052. URL: https://link.aps.org/doi/10.1103/PhysRevX.13.041052 (visited on 10/08/2024).

[186] Niklas Mueller, Andrey Tarasov, and Raju Venugopalan. "Deeply inelastic scattering structure functions on a hybrid quantum computer". In: *Phys. Rev. D* 102 (1 July 2020), p. 016007. DOI: 10.1103/PhysRevD.102.016007. URL: https://link.aps.org/doi/10.1103/PhysRevD.102.016007.

[187] Yunseong Nam et al. "Automated optimization of large quantum circuits with continuous parameters". In: *npj Quantum Information* 4.1 (2018), pp. 1–12.

[188] Nhung Hong Nguyen. "Trapped Ions: From Error Correction to Simulation of Quantum Field Theories". PhD thesis. University of Maryland, 2024.

[189] Naomi H. Nickerson and Benjamin J. Brown. "Analysing correlated noise on the surface code using adaptive decoding algorithms". en-GB. In: *Quantum* 3 (Apr. 2019). Publisher: Verein zur Förderung des Open Access Publizierens in den Quantenwissenschaften, p. 131. DOI: 10.22331/q-2019-04-08-131. URL: https://quantum-journal.org/papers/q-2019-04-08-131/ (visited on 10/17/2024).

[190] Erik Nielsen et al. "Gate Set Tomography". en-GB. In: *Quantum* 5 (Oct. 2021). Publisher: Verein zur Förderung des Open Access Publizierens in den Quantenwissenschaften, p. 557. DOI: 10.22331/q-2021-10-05-557. URL: https://quantum-journal.org/papers/q-2021-10-05-557/ (visited on 10/04/2024).

[191] M.A. Nielsen and I.L. Chuang. *Quantum Computation and Quantum Information*. Cambridge Series on Information and the Natural Sciences. Cambridge University Press, 2000. ISBN: 9780521635035. URL: https://books.google.com/books?id=65FqEKQOfP8C.

[192] Murphy Yuezhen Niu, Sirui Lu, and Isaac L. Chuang. *Optimizing QAOA: Success Probability and Runtime Dependence on Circuit Depth*. 2019. arXiv: 1905.12134 [quant-ph].

[193] J. S. Otterbach et al. *Unsupervised Machine Learning on a Hybrid Quantum Computer*. 2017. arXiv: 1712.05771 [quant-ph].

[194] Guido Pagano et al. "Quantum approximate optimization of the long-range Ising model with a trapped-ion quantum simulator". In: *Proc. Natl. Acad. Sci.* 117.41 (2020), pp. 25396–25401. ISSN: 0027-8424. DOI: 10.1073/pnas.2006373117. URL: https://www.pnas.org/content/117/41/25396.

[195] Dávid Pataki et al. "Coherent errors in stabilizer codes caused by quasistatic phase damping". In: *Physical Review A* 110.1 (July 2024). Publisher: American Physical Society, p. 012417. DOI: 10.1103/PhysRevA.110.012417. URL: https://link.aps.org/doi/10.1103/PhysRevA.110.012417 (visited on 09/29/2024).

[196] Wolfgang Paul. "Electromagnetic traps for charged and neutral particles". In: *Reviews of Modern Physics* 62.3 (July 1, 1990), pp. 531–540. ISSN: 0034-6861, 1539-0756. DOI: 10.1103/RevModPhys.62.531. URL: https://link.aps.org/doi/10.1103/RevModPhys.62.531 (visited on 10/14/2024).

[197] Elijah Pelofske et al. *Sampling on NISQ Devices:"Who's the Fairest One of All?"* 2021. arXiv: 2107.06468 [quant-ph].

[198] Juan M Pino et al. "Demonstration of the QCCD trapped-ion quantum computer architecture". In: *arXiv preprint arXiv:2003.01293* (2020).

[199] Juan M Pino et al. "Demonstration of the trapped-ion quantum CCD computer architecture". In: *Nature* 592.7853 (2021), pp. 209–213. DOI: 10.1038/s41586-021-03318-4.

[200] J. Preskill. *Quantum Information and Space-Time*. 2017. URL: https://www.microsoft.com/en-us/research/wp-content/uploads/2017/09/2017-01-15-Afternoon-Tutorial-John-Preskill.pdf.

[201] J. Preskill. "Simulating quantum field theory with a quantum computer". In: *Proceedings of Science, Lattice Conference 2018*. 2018. URL: https://pos.sissa.it/334/024/pdf.

[202] John Preskill. "Quantum Computing in the NISQ era and beyond". In: *Quantum* 2 (2018), p. 79. DOI: 10.22331/q-2018-08-06-79.

[203] Xiaogang Qiang et al. "Large-scale silicon quantum photonics implementing arbitrary two-qubit processing". In: *Nat. Photonics* 12.9 (2018), pp. 534–539. DOI: 10.1038/s41566-018-0236-y. URL: https://doi.org/10.1038/s41566-018-0236-y.

[204] Robert Raussendorf, Daniel E. Browne, and Hans J. Briegel. "Measurement-based quantum computation on cluster states". In: *Phys. Rev. A* 68 (2 Aug. 2003), p. 022312. DOI: 10.1103/PhysRevA.68.022312. URL: https://journals.aps.org/pra/abstract/10.1103/PhysRevA.68.022312.

[205] M.G.C. Resende. *Combinatorial Optimization in Telecommunications*. Springer, Boston, MA, 2003. ISBN: 9781461302339. URL: https://doi.org/10.1007/978-1-4613-0233-9_4.

[206] Lewis Fry Richardson and J. Arthur Gaunt. "VIII. The deferred approach to the limit". In: *Philosophical Transactions of the Royal Society A: Mathematical, Physical and Engineering Sciences* 226.299 (1927).

[207] Alessandro Roggero et al. "Preparation of excited states for nuclear dynamics on a quantum computer". In: *Physical Review C* 102.6 (Dec. 2020). ISSN: 2469-9993. DOI: 10.1103/physrevc.102.064624. URL: http://dx.doi.org/10.1103/PhysRevC.102.064624.

[208] Christian F Roos. "Ion trap quantum gates with amplitude-modulated laser beams". In: *New Journal of Physics* 10.1 (Jan. 2008), p. 013002. DOI: 10.1088/1367-2630/10/1/013002. URL: https://dx.doi.org/10.1088/1367-2630/10/1/013002.

[209] Wenjamin Rosenfeld et al. "Event-Ready Bell Test Using Entangled Atoms Simultaneously Closing Detection and Locality Loopholes". In: *Phys. Rev. Lett.* 119 (1 July 2017), p. 010402. DOI: 10.1103/PhysRevLett.119.010402. URL: https://link.aps.org/doi/10.1103/PhysRevLett.119.010402.

[210] Dan Roth. "On the hardness of approximate reasoning". In: *Artif. Intell* 82.1 (1996), pp. 273–302. ISSN: 0004-3702. DOI: https://doi.org/10.1016/0004-3702(94)00092-1. URL: https://www.sciencedirect.com/science/article/pii/0004370294000921.

[211] Subir Sachdev. "Quantum magnetism and criticality". In: *Nature Physics* 4.3 (2008), pp. 173–185. DOI: 10.1038/nphys894. URL: https://doi.org/10.1038/nphys894.

[212] C. A. Sackett et al. "Experimental entanglement of four particles". In: *Nature* 404.6775 (2000), pp. 256–259. DOI: 10.1038/35005011. URL: https://doi.org/10.1038/35005011.

[213] Y. Salathé et al. "Digital Quantum Simulation of Spin Models with Circuit Quantum Electrodynamics". In: *Physical Review X* 5.2 (June 2015). ISSN: 2160-3308. DOI: 10.1103/physrevx.5.021027. URL: http://dx.doi.org/10.1103/PhysRevX.5.021027.

[214] Martin J. Savage. "Nuclear Physics". In: *PoS* LATTICE2016 (2016), p. 021. DOI: 10.22323/1.256.0021. arXiv: 1611.02078 [hep-lat].

[215] Abdelkader Sbihi and Richard W. Eglese. "Combinatorial optimization and Green Logistics". In: *4OR* 5.2 (2007), pp. 99–116. DOI: 10.1007/s10288-007-0047-3. URL: https://doi.org/10.1007/s10288-007-0047-3.

[216] Valerio Scarani et al. "Nonlocality of cluster states of qubits". In: *Phys. Rev. A* 71 (4 Apr. 2005), p. 042325. DOI: 10.1103/PhysRevA.71.042325. URL: https://link.aps.org/doi/10.1103/PhysRevA.71.042325.

[217] Peter Schauss. "Quantum simulation of transverse Ising models with Rydberg atoms". In: *Quantum Science and Technology* 3.2 (Jan. 2018), p. 023001. DOI: 10.1088/2058-9565/aa9c59. URL: https://dx.doi.org/10.1088/2058-9565/aa9c59.

[218] Dirk Schingelman. "Stabilizer codes can be realized as graph codes". In: *arXiv preprint quant-ph/0111080* (2001). URL: https://arxiv.org/abs/quant-ph/0111080.

[219] Ferdinand Schmidt-Kaler et al. "Realization of the Cirac–Zoller controlled-NOT quantum gate". In: *Nature* 422.6930 (2003), pp. 408–411. DOI: 10.1038/nature01494. URL: https://doi.org/10.1038/nature01494.

[220] Alireza Seif et al. "Entanglement-enhanced learning of quantum processes at scale". en. In: ().

[221] Raja Selvarajan, Manas Sajjan, and Sabre Kais. *Variational quantum circuits to prepare low energy symmetry states*. 2021. arXiv: 2112.12857.

[222] Lynden K. Shalm et al. "Strong Loophole-Free Test of Local Realism". In: *Phys. Rev. Lett.* 115 (25 Dec. 2015), p. 250402. DOI: 10.1103/PhysRevLett.115.250402. URL: https://link.aps.org/doi/10.1103/PhysRevLett.115.250402.

[223] Yotam Shapira et al. "Robust Entanglement Gates for Trapped-Ion Qubits". In: *Phys. Rev. Lett.* 121 (18 Nov. 2018), p. 180502. DOI: 10.1103/PhysRevLett.121.180502. URL: https://link.aps.org/doi/10.1103/PhysRevLett.121.180502.

[224] Yotam Shapira et al. "Robust Two-Qubit Gates for Trapped Ions Using Spin-Dependent Squeezing". In: *Phys. Rev. Lett.* 130 (3 Jan. 2023), p. 030602. DOI: 10.1103/PhysRevLett.130.030602. URL: https://link.aps.org/doi/10.1103/PhysRevLett.130.030602.

[225] Meron Sheffer, Daniel Azses, and Emanuele Dalla Torre. "Playing quantum nonlocal games with six noisy qubits on the cloud". In: *arXiv preprint arXiv:2105.05266* (2021). URL: https://arxiv.org/abs/2105.05266.

[226] Peter W. Shor. "Polynomial-Time Algorithms for Prime Factorization and Discrete Logarithms on a Quantum Computer". In: *SIAM Journal on Computing* 26.5 (1997), pp. 1484–1509. DOI: 10.1137/S0097539795293172. eprint: https://doi.org/10.1137/S0097539795293172. URL: https://doi.org/10.1137/S0097539795293172.

[227] Marcus P. da Silva, Olivier Landon-Cardinal, and David Poulin. "Practical Characterization of Quantum Devices without Tomography". In: *Phys. Rev. Lett.* 107 (21 Nov. 2011), p. 210404. DOI: 10.1103/PhysRevLett.107.210404. URL: https://link.aps.org/doi/10.1103/PhysRevLett.107.210404.

[228] Törbjörn Sjöstrand, Stephen Mrenna, and Peter Skands. "PYTHIA 6.4 physics and manual". In: *Journal of High Energy Physics* 2006 (Mar. 2006). DOI: 10.1088/1126-6708/2006/05/026.

[229] Adam Smith et al. "Simulating quantum many-body dynamics on a current digital quantum computer". In: *npj Quantum Information* 5.1 (Nov. 2019). ISSN: 2056-6387. DOI: 10.1038/s41534-019-0217-0. URL: http://dx.doi.org/10.1038/s41534-019-0217-0.

[230] Anders Sørensen and Klaus Mølmer. "Quantum Computation with Ions in Thermal Motion". In: *Phys. Rev. Lett.* 82 (9 Mar. 1999), pp. 1971–1974. DOI: 10.1103/PhysRevLett.82.1971.

[231] Bhuvanesh Sundar et al. *A quantum algorithm to count weighted ground states of classical spin Hamiltonians*. 2019. arXiv: 1908.01745 [quant-ph].

[232] Federica Maria Surace and Alessio Lerose. "Scattering of mesons in quantum simulators". In: (2021). arXiv: 2011.10583 [cond-mat.quant-gas].

[233] Masuo Suzuki. "General theory of fractal path integrals with applications to many-body theories and statistical physics". In: *Journal of Mathematical Physics* 32.2 (1991), pp. 400–407. DOI: 10.1063/1.529425. eprint: https://doi.org/10.1063/1.529425. URL: https://doi.org/10.1063/1.529425.

[234] W. L. Tan et al. "Domain-wall confinement and dynamics in a quantum simulator". In: *Nature Physics* (Mar. 2021). ISSN: 1745-2481. DOI: 10.1038/s41567-021-01194-3. URL: http://dx.doi.org/10.1038/s41567-021-01194-3.

[235] Colin J Trout et al. "Simulating the performance of a distance-3 surface code in a linear ion trap". In: *New Journal of Physics* 20.4 (Apr. 2018), p. 043038. DOI: 10.1088/1367-2630/aab341. URL: https://dx.doi.org/10.1088/1367-2630/aab341.

[236] David K. Tuckett, Stephen D. Bartlett, and Steven T. Flammia. "Ultrahigh Error Threshold for Surface Codes with Biased Noise". In: *Physical Review Letters* 120.5 (Jan. 2018). Publisher: American Physical Society, p. 050505. DOI: 10.1103/PhysRevLett.120.050505. URL: https://link.aps.org/doi/10.1103/PhysRevLett.120.050505 (visited on 10/17/2024).

[237] David K. Tuckett et al. "Tailoring Surface Codes for Highly Biased Noise". In: *Phys. Rev. X* 9 (4 Nov. 2019), p. 041031. DOI: 10.1103/PhysRevX.9.041031. URL: https://link.aps.org/doi/10.1103/PhysRevX.9.041031.

[238] David K. Tuckett et al. "Tailoring Surface Codes for Highly Biased Noise". In: *Physical Review X* 9.4 (Nov. 2019). Publisher: American Physical Society, p. 041031. DOI: 10.1103/PhysRevX.9.041031. URL: https://link.aps.org/doi/10.1103/PhysRevX.9.041031 (visited on 09/27/2024).

[239] David K. Tuckett et al. "Fault-Tolerant Thresholds for the Surface Code in Excess of $5%$ under Biased Noise". In: *Physical Review Letters* 124.13 (Mar. 2020). Publisher: American Physical Society, p. 130501. DOI: 10.1103/PhysRevLett.124.130501. URL: https://link.aps.org/doi/10.1103/PhysRevLett.124.130501 (visited on 09/29/2024).

[240] Götz S. Uhrig. "Keeping a Quantum Bit Alive by Optimized π-Pulse Sequences". In: *Phys. Rev. Lett.* 98 (10 Mar. 2007), p. 100504. DOI: 10.1103/PhysRevLett.98.100504. URL: https://link.aps.org/doi/10.1103/PhysRevLett.98.100504.

[241] Maarten Van Damme et al. "Real-time scattering of interacting quasiparticles in quantum spin chains". In: *Phys. Rev. Research* 3 (1 Jan. 2021), p. 013078. DOI: 10.1103/PhysRevResearch.3.013078. URL: https://link.aps.org/doi/10.1103/PhysRevResearch.3.013078.

[242] Maarten Van den Nest, Jeroen Dehaene, and Bart De Moor. "Graphical description of the action of local clifford Transformations on Graph States". In: *Physical Review A* 69 (2004), p. 022316. DOI: https://doi.org/10.1103/PhysRevA.69.022316.

[243] Lorenza Viola and Emanuel Knill. "Robust Dynamical Decoupling of Quantum Systems with Bounded Controls". In: *Physical Review Letters* 90.3 (Jan. 2003). Publisher: American Physical Society, p. 037901. DOI: 10.1103/PhysRevLett.90.037901. URL: https://link.aps.org/doi/10.1103/PhysRevLett.90.037901 (visited on 10/01/2024).

[244] Lorenza Viola, Emanuel Knill, and Seth Lloyd. "Dynamical Decoupling of Open Quantum Systems". In: *Physical Review Letters* 82.12 (Mar. 1999). Publisher: American Physical Society, pp. 2417–2421. DOI: 10.1103/PhysRevLett.82.2417. URL: https://link.aps.org/doi/10.1103/PhysRevLett.82.2417 (visited on 10/01/2024).

[245] Lorenza Viola and Seth Lloyd. "Dynamical suppression of decoherence in two-state quantum systems". In: *Physical Review A* 58.4 (Oct. 1998). Publisher: American Physical Society, pp. 2733–2744. DOI: 10.1103/PhysRevA.58.2733. URL: https://link.aps.org/doi/10.1103/PhysRevA.58.2733 (visited on 10/01/2024).

[246] Joseph Vovrosh and Johannes Knolle. "Confinement and Entanglement Dynamics on a Digital Quantum Computer". In: (2020). arXiv: 2001.03044 [cond-mat.str-el].

[247] Mordecai Waegell and Justin Dressel. "Benchmarks of nonclassicality for qubit arrays". In: *npj Quantum Information* 5.1 (2019), pp. 1–8. DOI: 10.1038/s41534-019-0181-8.

[248] Joel J. Wallman and Joseph Emerson. "Noise tailoring for scalable quantum computation via randomized compiling". In: *Physical Review A* 94.5 (Nov. 2016). Publisher: American Physical Society, p. 052325. DOI: 10.1103/PhysRevA.94.052325. URL: https://link.aps.org/doi/10.1103/PhysRevA.94.052325 (visited on 09/29/2024).

[249] Philip Walther et al. "Experimental Violation of a Cluster State Bell Inequality". In: *Phys. Rev. Lett.* 95 (2 July 2005), p. 020403. DOI: 10.1103/PhysRevLett.95.020403. URL: https://link.aps.org/doi/10.1103/PhysRevLett.95.020403.

[250] Pengfei Wang et al. "Single ion qubit with estimated coherence time exceeding one hour". In: *Nature Communications* 12.1 (Jan. 11, 2021). Publisher: Nature Publishing Group, p. 233. ISSN: 2041-1723. DOI: 10.1038/s41467-020-20330-w. URL: https://www.nature.com/articles/s41467-020-20330-w (visited on 10/08/2024).

[251] Ye Wang et al. "High-Fidelity Two-Qubit Gates Using a Microelectromechanical-System-Based Beam Steering System for Individual Qubit Addressing". In: *Physical Review Letters* 125.15 (Oct. 6, 2020), p. 150505. ISSN: 0031-9007, 1079-7114. DOI: 10.1103/PhysRevLett.125.150505. URL: https://link.aps.org/doi/10.1103/PhysRevLett.125.150505 (visited on 10/10/2024).

[252] Matthew Ware et al. "Experimental Pauli-frame randomization on a superconducting qubit". In: *Physical Review A* 103.4 (Apr. 2021). Publisher: American Physical Society, p. 042604. DOI: 10.1103/PhysRevA.103.042604. URL: https://link.aps.org/doi/10.1103/PhysRevA.103.042604 (visited on 10/06/2024).

[253] U. Warring et al. "Individual-Ion Addressing with Microwave Field Gradients". In: *Physical Review Letters* 110.17 (Apr. 22, 2013). Publisher: American Physical Society, p. 173002. DOI: 10.1103/PhysRevLett.110.173002. URL: https://link.aps.org/doi/10.1103/PhysRevLett.110.173002 (visited on 10/14/2024).

[254] Adam Bene Watts et al. "Exponential separation between shallow quantum circuits and unbounded fan-in shallow classical circuits". In: *Proceedings of the 51st Annual ACM SIGACT Symposium on Theory of Computing*. 2019, pp. 515–526. DOI: 10.1145/3313276.3316404.

[255] S Weaver et al. "Satisfiability-based Set Membership Filters". In: *J. Satisf. Boolean Model. Comput.* 8 (2014), pp. 129–148.

[256] Eugene P. Wigner. "Lower Limit for the Energy Derivative of the Scattering Phase Shift". In: *Phys. Rev.* 98 (1 Apr. 1955), pp. 145–147. DOI: 10.1103/PhysRev.98.145. URL: https://link.aps.org/doi/10.1103/PhysRev.98.145.

[257] Madita Willsch et al. "Benchmarking the quantum approximate optimization algorithm". In: *Quantum Inf. Process* 19.7 (2020), p. 197. DOI: 10.1007/s11128-020-02692-8. URL: https://doi.org/10.1007/s11128-020-02692-8.

[258] K. Wright et al. "Benchmarking an 11-qubit quantum computer". In: *Nature Communications* 10.1 (Nov. 2019), p. 5464. ISSN: 2041-1723. DOI: 10.1038/s41467-019-13534-2.

[259] Yulin Wu et al. "Strong quantum computational advantage using a superconducting quantum processor". In: *arXiv:2106.14734* (2021). URL: https://arxiv.org/abs/2106.14734.

[260] Kübra Yeter-Aydeniz, George Siopsis, and Raphael C. Pooser. *Scattering in the Ising Model Using Quantum Lanczos Algorithm*. 2021. arXiv: 2008.08763 [quant-ph].

[261] Xiang Yue et al. "Graph embedding on biomedical networks: methods, applications and evaluations". In: *Bioinformatics* 36.4 (Feb. 2020), pp. 1241–1251. ISSN: 1367-4803. DOI: 10.1093/bioinformatics/btz718. URL: https://europepmc.org/articles/PMC7703771.

[262] Fuzheng Zhang et al. "Collaborative Knowledge Base Embedding for Recommender Systems". In: *Proc. ACM SIGKDD Int. Conf. Knowl.* (2016).

[263] J. Zhang et al. "Observation of a many-body dynamical phase transition with a 53-qubit quantum simulator". In: *Nature* 551.7682 (Nov. 2017), pp. 601–604. DOI: 10.1038/nature24654. arXiv: 1708.01044 [quant-ph].

[264] Yuxuan Zhang, Ruizhe Zhang, and Andrew C Potter. "QED driven QAOA for network-flow optimization". In: *Quantum* 5 (2021), p. 510.

[265] Han-Sen Zhong et al. "Quantum computational advantage using photons". In: *Science* 370.6523 (2020), pp. 1460–1463. ISSN: 0036-8075. DOI: 10.1126/science.abe8770. URL: https://science.sciencemag.org/content/370/6523/1460.

[266] D Zhu et al. "Generation of thermofield double states and critical ground states with a quantum computer". In: *Proceedings of the National Academy of Sciences* 117.41 (2020), pp. 25402–25406.

[267] D. Zhu et al. "Cross-platform comparison of arbitrary quantum states". In: *Nature Communications* 13.1 (2022), p. 6620. DOI: 10.1038/s41467-022-34279-5. URL: https://doi.org/10.1038/s41467-022-34279-5.

[268] Daiwei Zhu et al. "Interactive cryptographic proofs of quantumness using mid-circuit measurements". In: *Nature Physics* 19.11 (Nov. 2023). Publisher: Nature Publishing Group, pp. 1725–1731. ISSN: 1745-2481. DOI: 10.1038/s41567-023-02162-9. URL: https://www.nature.com/articles/s41567-023-02162-9 (visited on 10/08/2024).

[269] Shi-Liang Zhu, C. Monroe, and L.-M. Duan. "Arbitrary-speed quantum gates within large ion crystals through minimum control of laser beams". In: *Europhysics Letters* 73.4 (Jan. 2006), p. 485. DOI: 10.1209/epl/i2005-10424-4. URL: https://dx.doi.org/10.1209/epl/i2005-10424-4.

[270] Yingyue Zhu et al. "Pairwise-Parallel Entangling Gates on Orthogonal Modes in a Trapped-Ion Chain". In: *Advanced Quantum Technologies* 6.11 (2023). _eprint: https://onlinelibrary.wiley.com/doi/pdf/10.1002/qute.202300056, p. 2300056. ISSN: 2511-9044. DOI: 10.1002/qute.202300056. URL: https://onlinelibrary.wiley.com/doi/abs/10.1002/qute.202300056 (visited on 08/01/2024).

[271] Erez Zohar, J. Ignacio Cirac, and Benni Reznik. "Quantum simulations of gauge theories with ultracold atoms: Local gauge invariance from angular-momentum conservation". In: *Physical Review A* 88.2 (Aug. 2013). ISSN: 1094-1622. DOI: 10.1103/physreva.88.023617. URL: http://dx.doi.org/10.1103/PhysRevA.88.023617.